

# Experimental and Theoretical Developments in the Application of Lagrangian Coherent Structures to Geophysical Transport

Peter J. Nolan

Dissertation submitted to the Faculty of the  
Virginia Polytechnic Institute and State University  
in partial fulfillment of the requirements for the degree of

Doctor of Philosophy  
in  
Engineering Mechanics

Shane D. Ross, Chair

Traian Iliescu

Craig A. Woolsey

David G. Schmale

Hosein Foroutan

March 5, 2019

Blacksburg, Virginia

Keywords: Lagrangian coherent structures, geophysical fluid mechanics, dynamical systems

Copyright 2019, Peter J. Nolan

# Experimental and Theoretical Developments in the Application of Lagrangian Coherent Structures to Geophysical Transport

Peter J. Nolan

## ABSTRACT

The transport of material in geophysical fluid flows is a problem with important implications for fields as diverse as: agriculture, aviation, human health, disaster response, and weather forecasting. Due to the unsteady nature of geophysical flows, predicting how material will be transported in these systems can often be challenging. Tools from dynamical systems theory can help to improve the prediction of material transport by revealing important transport structures. These transport structures reveal areas of the flow where fluid parcels, and thus material transported by those parcels, are likely to converge or diverge. Typically, these transport structures have been uncovered by the use of Lagrangian diagnostics. Unfortunately, calculating Lagrangian diagnostics can often be time consuming and computationally expensive.

Recently new Eulerian diagnostics have been developed. These diagnostics are faster and less expensive to compute, while still revealing important transport structures in fluid flows. Because Eulerian diagnostics are so new, there is still much about them and their connection to Lagrangian diagnostics that is unknown. This dissertation will fill in some of this gap and provide a mathematical bridge between Lagrangian and Eulerian diagnostics.

This dissertation is composed of three projects. These projects represent theoretical, numerical, and experimental advances in the understanding of Eulerian diagnostics and their relationship to Lagrangian diagnostics. The first project rigorously explores the deep mathematical relationship that exists between Eulerian and Lagrangian diagnostics. It proves that some of the new Eulerian diagnostics are the limit of Lagrangian diagnostics as integra-

tion time of the velocity field goes to zero. Using this discovery, a new Eulerian diagnostic, infinitesimal-time Lagrangian coherent structures is developed. The second project develops a methodology for estimating local Eulerian diagnostics from wind velocity data measured by a fixed-wing unmanned aircraft system (UAS) flying in circular arcs. Using a simulation environment, it is shown that the Eulerian diagnostic estimates from UAS measurements approximate the true local Eulerian diagnostics and can predict the passage of Lagrangian diagnostics. The third project applies Eulerian diagnostics to experimental data of atmospheric wind measurements. These are then compared to Eulerian diagnostics as calculated from a numerical weather simulation to look for indications of Lagrangian diagnostics.

# Experimental and Theoretical Developments in the Application of Lagrangian Coherent Structures to Geophysical Transport

Peter J. Nolan

## GENERAL AUDIENCE ABSTRACT

How particles are moved by fluid flows, such as the oceanic currents and the atmospheric winds, is a problem with important implications for fields as diverse as: agriculture, aviation, human health, disaster response, and weather forecasting. Because these fluid flows tend to change over time, predicting how particles will be moved by these flows can often be challenging. Fortunately, mathematical tools exist which can reveal important geometric features in these flows. These geometric features can help us to visualize regions where particles are likely to come together or spread apart, as they are moved by the flow. In the past, these geometric features have been uncovered by using methods which look at the trajectories of particles in the flow. These methods are referred to as Lagrangian, in honor of the Italian mathematician Joseph-Louis Lagrange. Unfortunately, calculating the trajectories of particles can be a time consuming and computationally expensive process.

Recently, new methods have been developed which look at how the speed of the flow changes in space. These new methods are referred to as Eulerian, in honor of the Swiss mathematician Leonhard Euler. These new Eulerian methods are faster and less expensive to calculate, while still revealing important geometric features within the flow. Because these Eulerian methods are so new, there is still much that we do not know about them and their connection to the older Lagrangian methods. This dissertation will fill in some of this gap and provide a mathematical bridge between these two methodologies.

This dissertation is composed of three projects. These projects represent theoretical, numerical, and experimental advances in the understanding of these new Eulerian methods

and their relationship to the older Lagrangian methods. The first project explores the deep mathematical relationship that exists between Eulerian and Lagrangian diagnostic tools. It mathematically proves that some of the new Eulerian diagnostics are the limit of Lagrangian diagnostics as the trajectory's integration times is decreased to zero. Taking advantage of this discovery, a new Eulerian diagnostic is developed, called infinitesimal-time Lagrangian coherent structures. The second project develops a technique for estimating local Eulerian diagnostics using wind speed measures from a single fixed-wing unmanned aircraft system (UAS) flying in a circular path. Using computer simulations, we show that the Eulerian diagnostics as calculated from UAS measurements provide a reasonable estimate of the true local Eulerian diagnostics. Furthermore, we show that these Eulerian diagnostics can be used to estimate the local Lagrangian diagnostics. The third project applies these Eulerian diagnostics to real-world wind speed measurements. These results are then compared to Eulerian diagnostics that were calculated from a computer simulation to look for indications of Lagrangian diagnostics.

*This dissertation is dedicated to my parents, Peter and Madeline Nolan. They have given me their love and support throughout this tumultuous journey.*

# Acknowledgments

I would like to say thank you to my:

committee members for guiding me through this process and offering me the opportunities to work on many diverse projects,

labmates for their help, companionship and assistance,

and friends for helping to keep me grounded.

# Contents

<b>List of Figures</b>	<b>xiii</b>
<b>List of Tables</b>	<b>xxiii</b>
<b>1 Introduction</b>	<b>1</b>
1.1 Background . . . . .	1
1.2 Governing equations . . . . .	4
1.3 Research overview . . . . .	6
1.4 Research not covered in this dissertation . . . . .	8
1.4.1 3D atmospheric Lagrangian coherent structures . . . . .	8
1.4.2 Detection of atmospheric Lagrangian coherent structures via sonic de- tection and ranging . . . . .	9
1.4.3 Lagrangian coherent structures and pollution transport . . . . .	12
1.4.4 Hybrid Lagrangian coherent structures . . . . .	16
1.4.5 Trajectory divergence rate . . . . .	19

1.4.6	Reduced order modeling . . . . .	20
<b>Bibliography</b>		<b>22</b>
<b>2</b>	<b>Finite-time Lyapunov exponent field in the infinitesimal time limit</b>	<b>26</b>
2.1	Introduction . . . . .	27
2.2	Setup and Notation . . . . .	29
2.3	Expansion of the Cauchy-Green tensor in the infinitesimal integration time limit . . . . .	31
2.3.1	Eigenvalues of S as FTLE limit as integration time goes to zero . . . . .	31
2.3.2	Approximating FTLE to second-order in integration time . . . . .	34
2.3.3	Equality of the eigenvectors of S and C as integration time goes to zero . . . . .	36
2.4	Infinitesimal-time LCS . . . . .	37
2.5	Examples . . . . .	39
2.5.1	2D Nonlinear Saddle Flow . . . . .	39
2.5.2	2D Time-Varying Double-Gyre Flow . . . . .	42
2.5.3	2D Geophysical Flow Example . . . . .	46
2.5.4	3D Time-varying Double Gyre Flow . . . . .	50
2.5.5	3D ABC Flow . . . . .	53
2.6	Conclusion . . . . .	57
	Appendix A . . . . .	60

A.1	Expansion of the right Cauchy-Green tensor $C$ . . . . .	60
A.2	Proof of Eq. (2.16) . . . . .	61
A.3	Eigenvalues of the Taylor expanded Cauchy-Green tensor . . . . .	62
A.4	Details for Time-Varying Double-Gyre Example . . . . .	67
	<b>Bibliography</b> . . . . .	<b>71</b>
<b>3</b>	<b>A Method for Detecting Atmospheric Lagrangian Coherent Structures using a Single Fixed-Wing Unmanned Aircraft System</b> . . . . .	<b>75</b>
1	Introduction . . . . .	76
2	Methods . . . . .	81
2.1	Lagrangian-Eulerian Analysis . . . . .	81
2.2	Gradient Approximation from UAS Flight . . . . .	83
2.3	Model Data . . . . .	86
3	Results . . . . .	88
3.1	Approximating local Eulerian Metrics from UAS flights . . . . .	88
3.2	Using Eulerian Metrics to infer Lagrangian Dynamics . . . . .	90
3.3	Inferring Lagrangian Dynamics from UAS measurements . . . . .	94
4	Discussion . . . . .	95
5	Conclusions . . . . .	102
	Appendix B . . . . .	104

<b>Bibliography</b>	<b>108</b>
<b>4 Coordinated Unmanned Aircraft System and Ground-based Weather Measurements to Predict Lagrangian Coherent Structures</b>	<b>114</b>
1 Introduction . . . . .	116
2 Materials and Methods . . . . .	120
2.1 Sensor Package onboard UAS . . . . .	120
2.2 Permissions for Flight Operations . . . . .	122
2.3 Coordinated aerial and ground-based measurements . . . . .	123
2.4 WRF-LES model . . . . .	124
2.5 Lagrangian-Eulerian analysis . . . . .	125
2.6 Computation of Wind Gradient and Attraction Rate . . . . .	127
2.7 Uncertainty Analysis . . . . .	129
3 Results . . . . .	131
3.1 Comparison of Measurements . . . . .	132
3.2 Attraction rate measurements . . . . .	136
4 Discussion . . . . .	138
5 Conclusions . . . . .	143
<b>Bibliography</b>	<b>146</b>
<b>5 Conclusion</b>	<b>152</b>

1	Summary . . . . .	152
2	Future research direction . . . . .	154
	<b>Bibliography</b>	<b>157</b>

# List of Figures

1.1	Top: Wind velocity field along 925 mb pressure surface from a simulation of the global atmosphere, approximately 760 m above sea level. Bottom: Backward-time FTLE field, with an integration time of 24 hr. Regions in yellow are where fluid parcels are most likely to converge over the next 24 hr.	2
1.2	3D backward-time FTLE field from a CBL simulation. Colorbar has units of $s^{-1}$ . An animation of this flow can be found at <a href="https://www.youtube.com/watch?v=mTmdv-Kvz7Y">https://www.youtube.com/watch?v=mTmdv-Kvz7Y</a> .	10
1.3	Isosurfaces of a 3D backward-time FTLE field from a CBL simulation. Colorbar has units of $s^{-1}$ . An animation of this flow can be found at <a href="https://www.youtube.com/watch?v=9FEBGTPSmio">https://www.youtube.com/watch?v=9FEBGTPSmio</a> .	11
1.4	Mean and standard deviation of a 3D backward-time FTLE field from a CBL simulation. The variance of the velocity component fields are shown as well. An animation of this figure can be found at <a href="https://www.youtube.com/watch?v=FgV-1tVDd0w">https://www.youtube.com/watch?v=FgV-1tVDd0w</a> .	12
1.5	Intersection of an attracting (blue) LCS and a repelling (red) LCS from a CBL simulation. A blob of passive tracers is shown in green. An animation of these structures can be found at <a href="https://www.youtube.com/watch?v=NflrLXB6Gbc">https://www.youtube.com/watch?v=NflrLXB6Gbc</a> .	13

1.6	3D atmospheric attracting LCSs above Blacksblack VA. This image shows that 3D atmospheric LCSs come in both horizontal and vertical structures. Note that the y axis corresponds to North, and the x axis to East. . . . .	14
1.7	Results from numerical SoDAR experiments. Left: The FTLE profile calculated from 1D SoDAR model taken from a 3D WRF-LES. Right: The FTLE isosurfaces calculated from full 3D velocity field. Blue line simulated SoDAR sampling profile. Both colorbars have units $s^{-1}$ . . . . .	15
1.8	An intersection of attracting (blue) and repelling (red) LCSs over the San Francisco Bay Area, California. Passive tracers are shown in green. An animation of this figure, showing the saddle-point-like behavior of this intersection can be seen at <a href="https://www.youtube.com/watch?v=fci3r0chMxw">https://www.youtube.com/watch?v=fci3r0chMxw</a> . . . . .	16
1.9	Comparison of -1 hr backward-time FTLE fields for different atmospheric species: A) horizontal wind, B) water vapor, C) nitrogen dioxide, D) ozone. The horizontal wind velocity field is taken from a horizontal level $\sim 100$ m above ground level. The other three species are calculated based on column-averaged and species-weighted horizontal wind vector components. All four species have their own unique structures (yellow) where fluid parcels will converge. . . . .	17
1.10	Comparison of an ocean LCS (red and yellow) and a hybrid LCS (blue and green) with a windage coefficient of 0.019 (the same windage coefficient as a person-in-water), south of Martha's Vineyard, Massachusetts. It can be seen that tracers that are advected under the ocean current (orange) converge to the ocean LCS; while the tracers advected under the hybrid velocity field (cyan) converge to the hybrid LCS. . . . .	18

1.11	Left: depiction of the trajectory divergence rate along with streamlines from an MSEAS model [24] simulation of the oceanic flow around Martha’s Vineyard, Massachusetts. Areas in blue show where streamlines converge, while areas in orange show where streamlines diverge. Right: attracting LCSs (blue) and repelling LCSs (red) for an integration time of 2 hr are shown atop the trajectory divergence rate field. The inset plot shows the trajectory divergence rate along 41.3°N latitude from 70.6°W to 70.3°W, marked by the points A and B. Places where LCSs cross this latitude between A and B are shown as lines colored red for repelling and blue for attracting. Notice how the repelling LCSs tend to correspond to peaks in the trajectory divergence rate; while attracting LCSs correspond to troughs. This image was published in [13].	20
2.1	RMSE for successive approximations of the backward-time FTLE field for the nonlinear saddle (2.48) expanded in $T$ : zeroth-order (blue), first-order (magenta), second-order (black). Notice that the error grows linear in $ T $ , quadratic in $ T $ , and cubic in $ T $ , respectively, as shown more clearly in the log-log plot on the right.	43
2.2	Left: RMSE vs. $ T $ for successive approximations of the backward-time FTLE field for the double-gyre expanded in $T$ : zeroth-order (blue), first-order (magenta), second-order (black), showing the error grow linear, quadratic, and cubic in $ T $ , respectively. Right: Shows this RMSE vs. $ T $ in a log-log plot.	45
2.3	Left: FTLE field for the double-gyre flow for an integration period of $T = -0.3$ . Right: approximation to the FTLE field to first-order in $T$ . Parameters: $A = 0.1$ , $\omega = 0.2\pi$ , $\epsilon = 0.25$ , and $t_0 = 0$ .	46

2.4	RMSE for successive approximations of the backward-time FTLE field for an atmospheric flow expanded in $T$ : zeroth-order (blue), first-order (magenta), and second-order (black). Time is in seconds. . . . .	47
2.5	Comparison of the attraction rate (A), with FTLE fields of integration times $T =$ (B) $-1$ hr (C) $-2$ hr, (D) $-4$ hr. The spatial correlation between these fields can be seen in figure 2.6 . . . . .	48
2.6	Pearson correlation coefficient between the attraction rate and the backward-time FTLE for different integration times, $ T $ . . . . .	49
2.7	iLCSs and passive tracers at different integration times, $T$ . A) $T = 0$ hr, B) $T = 2$ hr, C) $T = 4$ hr, D) $T = 8$ hr. Repelling iLCSs are shown in red, attraction iLCSs in blue, and passive tracers in cyan. . . . .	50
2.8	Comparison of the attraction rate field, $s_1$ , left, and the repulsion rate field, $s_2$ , right, at $T = 0$ . Structures in the attraction rate field are noticeably stronger than in the repulsion rate field. The attraction rate field has been multiplied by $-1$ to aid in visualization. Colorbar has units of $\text{hr}^{-1}$ . . . . .	51
2.9	RMSE for successive approximations of the backward-time FTLE field for the 3D double-gyre flow (2.70) expanded in $T$ : zeroth-order (blue), first-order (magenta). Time is in non-dimensional units. . . . .	52
2.10	An attracting 3D iLCS, blue, with a blob passive tracers, green, shown at different angles. Top row shows the iLCS and tracers at the initial time, $t=0$ . Bottom row shows the iLCS and tracers after being advected forward in time 1.25. . . . .	53

2.11	A repelling 3D iLCS, red, with a blob a passive tracers, green, shown at different angles. Top row shows the iLCS and tracers at the initial time, $t=0$ . Bottom row shows the iLCS and tracers after being advected forward in time 1.25. . . . .	54
2.12	RMSE for successive approximations of the backward-time FTLE field for the ABC flow (2.71) expanded in $T$ : zeroth-order (blue), first-order (magenta). Time is in non-dimensional units. . . . .	56
2.13	An attracting 3D iLCS, blue, with a blob a passive tracers, green, shown at different angles. Top row shows the iLCS and tracers at the initial time, $t_0 = 0$ . Bottom row shows the iLCS and tracers after being advected forward in time to $T = t - t_0 = 1.309$ . . . . .	58
2.14	A repelling 3D iLCS, red, with a blob a passive tracers, green, shown at different angles. Top row shows the iLCS and tracers at the initial time, $t_0 = 0$ . Bottom row shows the iLCS and tracers after being advected forward in time to $T = t - t_0 = 1.309$ . . . . .	59
3.1	Map of the Mid-Atlantic United States, Kentland Farm in Virginia is shown in red. . . . .	80
3.2	Schematic of the effect of a trough of the attraction rate, $s_1$ , field on a fluid parcel. . . . .	83
3.3	Schematic of the trajectory divergence rate. Where $\dot{\rho} < 0$ , trajectories are converging; where $\dot{\rho} > 0$ trajectories are diverging. . . . .	83
3.4	Schematic showing positions where velocity measurements were made and the position of the circle gradient frame to the reference frame. . . . .	84

3.5	Simulated 3D UAS flight path (solid blue line) along with a 2D perfect circle (dotted black line). The 2D circle is at a constant altitude, while the 3D UAS flight tracks the 850mb isosurface. The vertical dimension is shown highly exaggerated. . . . .	87
3.6	Comparison of measurements of the trajectory divergence rate $\dot{\rho}$ at the center point of the circular sampling orbit (red), along the path of a simulated UAS flight (black), and along a circular arc (blue). The radius of the circle and flight path is shown in the lower right hand corner of each time series. The circular arc and the simulated UAS flight are nearly on top of each other. . .	89
3.7	Comparison of measurements of the attraction rate $s_1$ at the center point of the circular sampling orbit (red), along the path of a simulated UAS flight (black), and along a circular arc (blue). The radius of the circle and flight path is shown in the lower right hand corner of each time series. The circular arc and the simulated UAS flight are nearly on top of each other. . . . .	90
3.8	Comparison of the trajectory divergence rate with the 0.5, 1, and 2 hr backward-time FTLE from $t=4$ to $t=215$ hrs. FTLE fields have been multiplied by -1 to offer better comparison of attraction. . . . .	91
3.9	Comparison of the attraction rate with the 0.5, 1, and 2 hr backward-time FTLE from $t=4$ to $t=215$ hrs. FTLE fields have been multiplied by -1 to offer better comparison of attraction. . . . .	92
3.10	Schematic of LCS detection showing two examples of threshold radii as dashed lines. An attracting LCS falls within the larger threshold radius but does not fall within the smaller radius. The instantaneous wind field is depicted as the background vector field. . . . .	93

3.11	<p>Depiction of a true positive (left) and a false positive (right), from approximately 43.5 hrs and 20.67 hrs respectively. The true attraction rate field over Kentland Farm Va. is displayed, darker greens are lower values of the attraction rate. Grid points where the value of the attraction rate is above the threshold value are masked (white). Attracting LCS with an integration time of -1 hr are shown as blue lines. The threshold radius is shown by the black dashed circle and has a radius of 5 km. In both examples the attraction rate at the center of the sampling domain is below the threshold value, thus meeting the criterion for a positive identification of an LCS passing within the threshold radius. In the true positive example there is an LCS passing within the threshold radius. Meanwhile, in the false positive there is no LCS within the threshold radius. The ROC plot point for the particular case shown in this figure (i.e. threshold value and radius) is depicted by a red “+” marker in figure 3.14. . . . .</p>	94
3.12	<p>Schematic of an idealized ROC curve and with threshold percentiles. . . . .</p>	95
3.13	<p>ROC curves for the trajectory divergence rate, <math>\dot{\rho}</math>, as measured at the center point ability to detect 90<sup>th</sup> percentile LCSs with integration times of 0.5 (green), 1 (red), and 2 (blue) hrs. Threshold radii are displayed in the upper left hand corner. The AUC for each integration time is given in the legend. . . . .</p>	96
3.14	<p>ROC curves for the attraction rate, <math>s_1</math>, as measured at the center point ability to detect 90<sup>th</sup> percentile LCSs with integration times of 0.5 (green), 1 (red), and 2 (blue) hrs. Threshold radii are displayed in the upper left hand corner. The AUC for each integration time is given in the legend. The red “+” marker corresponds to the plot point for the case (i.e. threshold value and radius) that was shown in figure 3.11. . . . .</p>	97

3.15	ROC curves for the trajectory divergence rate, $\dot{\rho}$ , as measured from a 2 km radius UAS simulation ability to detect 90 <sup>th</sup> percentile LCSs with integration times of 0.5 (green), 1 (red), and 2 (blue) hrs. Threshold radii are displayed in the upper left hand corner. The AUC for each integration time is given in the legend. . . . .	98
3.16	ROC curves for the attraction rate, $s_1$ , as measured from a 2 km radius UAS simulation ability to detect 90 <sup>th</sup> percentile LCSs with integration times of 0.5 (green), 1 (red), and 2 (blue) hrs. Threshold radii are displayed in the upper left hand corner. The AUC for each integration time is given in the legend. . . . .	99
4.1	Schematic illustration of an attracting LCS, and its effect on a fluid parcel over a short advection time. . . . .	118
4.2	Schematic of Inspire 2 sampler assembly. An interactive 3D version can be found at <a href="https://a360.co/2OnKTl4">https://a360.co/2OnKTl4</a> . . . . .	120
4.3	Calibration flight with vertical array of sensors at 10 m (UAS with Atmos 22 sonic anemometer), 4 m (Atmos22 sonic anemometer), and 2 m (CSAT3 sonic anemometer) (left). White arrows indicate the sensors at each of the respective heights. Calibration flight (B2) with one ground-based sensor on the MURC tower and one UAS, both at 15 m (right). White arrows indicate the sensors for each of the platforms. . . . .	121
4.4	Simultaneous flights with sensors in a triangle formation (white arrows). Both UASs were operating off of marks on the taxiway, and the MURC tower was stationed north of the UAS operations. . . . .	122

4.5	Schematic of how the velocity gradient, $\nabla\mathbf{v}(\mathbf{x}, t)$ , was computed from sensor measurements. Using wind measurements from three independent sensors, a linear function was generated for a triangular element. This function was then used to interpolate the wind to an interpolated point. A finite-difference scheme, eq. 4.4, was then used to calculate the gradient of the two components, $u$ and $v$ , of the horizontal wind. . . . .	128
4.6	Satellite image of the sampling region with sensor locations marked with blue pins. A potential interpolated point is marked in yellow. . . . .	132
4.7	Comparison of wind speed measurements on the flux tower for a height of 2 m (CSAT3 sonic anemometer, yellow), 4 m (Atmos22 sonic anemometer), and 10 m (UAS with Atmos 22 sonic anemometer. . . . .	133
4.8	RMSE comparison for wind speed and direction measurements collected from UAS B and MURC Tower at 15 meters above ground level. . . . .	134
4.9	Comparison of wind speed measurements from UAS A and ground based sensors.	136
4.10	Comparison of wind speed measurements from UAS B and ground based sensors.	137
4.11	Wind speed from WRF-LES grid point nearest to where the attraction rate was calculated (blue) and wind speed as measured by sensors, interpolated to the attraction rate position (orange) overlaid with flight average of the wind speed (black). Wind speed from the WRF-LES comes from the 10m height level, while wind speed measurements were performed by sensors at 15m. . .	138

4.12	The velocity gradient from WRF-LES predictions (blue) and the velocity gradient as calculated from sensor measurements (orange). The velocity gradient from the WRF-LES comes from the 10 m height level wind speed, while wind speed measurements used to calculate the velocity gradient were performed by sensors at 15 m. The uncertainty ranges for the velocity gradient as calculated from sensor measurements are shown in gray. . . . .	139
4.13	The attraction rate from WRF-LES predictions (blue) and the attraction rate as calculated from sensor measurements (orange) overlaid with flight average of the attraction rate (black). The uncertainty ranges for the attraction rate measurements are shown in gray. The attraction rate from the WRF-LES comes from the 10 m height level wind speed, while wind speed measurements used to calculate the attraction rate were performed by sensors at 15 m. Times of interest are highlighted with a yellow vertical line, corresponding to the predicted attraction rate fields shown in figures 4.14 and 4.15, respectively.	140
4.14	The attraction rate field at 1400 MDT, convective cells can be seen, bordered by troughs of the attracting field, throughout the domain. A front appears to be blowing an attracting feature out of the east of the domain. Sampling region is marked with a red dot. . . . .	141
4.15	The attraction rate field at 1550 MDT, an attracting LCS can be seen along the center of the domain having ridden the front out of the east. The sampling region is marked with a red dot. Part of the attracting feature is shown as a white line. The direction the feature is moving is shown by black arrows. . .	142

# List of Tables

3.1	Pearson correlation coefficients for trajectory divergence rate, $\dot{\rho}$ , measurements. Coefficients range from 0.730 to 0.965. . . . .	88
3.2	Pearson correlation coefficients for attraction rate, $s_1$ , measurements. Coefficients range from 0.577 to 0.939. . . . .	91
4.1	UAS mission and ground station details. UAS sensor packages were functionally identical. Time start and time end are in local time, Mountain Daylight Time. Height is in meters above ground level. . . . .	131
4.2	Pearson correlation coefficients for wind speed measurements between different UAS packages and ground based sensors. . . . .	136



# Chapter 1

## Introduction

### 1.1 Background

The transport of material in geophysical fluid flows is a problem with important implications for fields as diverse as: agriculture [1, 2, 3, 4], aviation [5, 6], human health [7, 8], disaster response [9, 10], and weather forecasting [11]. Due to the unsteady nature of geophysical flows, predicting how material will be transported in these systems can often be challenging. Tools from dynamical systems theory can help to improve the prediction of material transport by revealing important transport structures. These transport structures reveal areas of the flow where fluid parcels, and thus material transported by those parcels, are likely to converge or diverge. A demonstration of this can be seen in figure 1.1. The top image shows the wind velocity field along the 925 mb pressure surface from a simulation of the global atmosphere. Looking at this image, it is difficult to predict how material advected by this flow will spread. The bottom image shows this flow's backward-time finite-time Lyapunov exponent (FTLE) field, for an integration period of 24 hr. The transport structures of this flow show up in yellow, it is these yellow regions where material will likely converge over the subsequent 24

hr period.

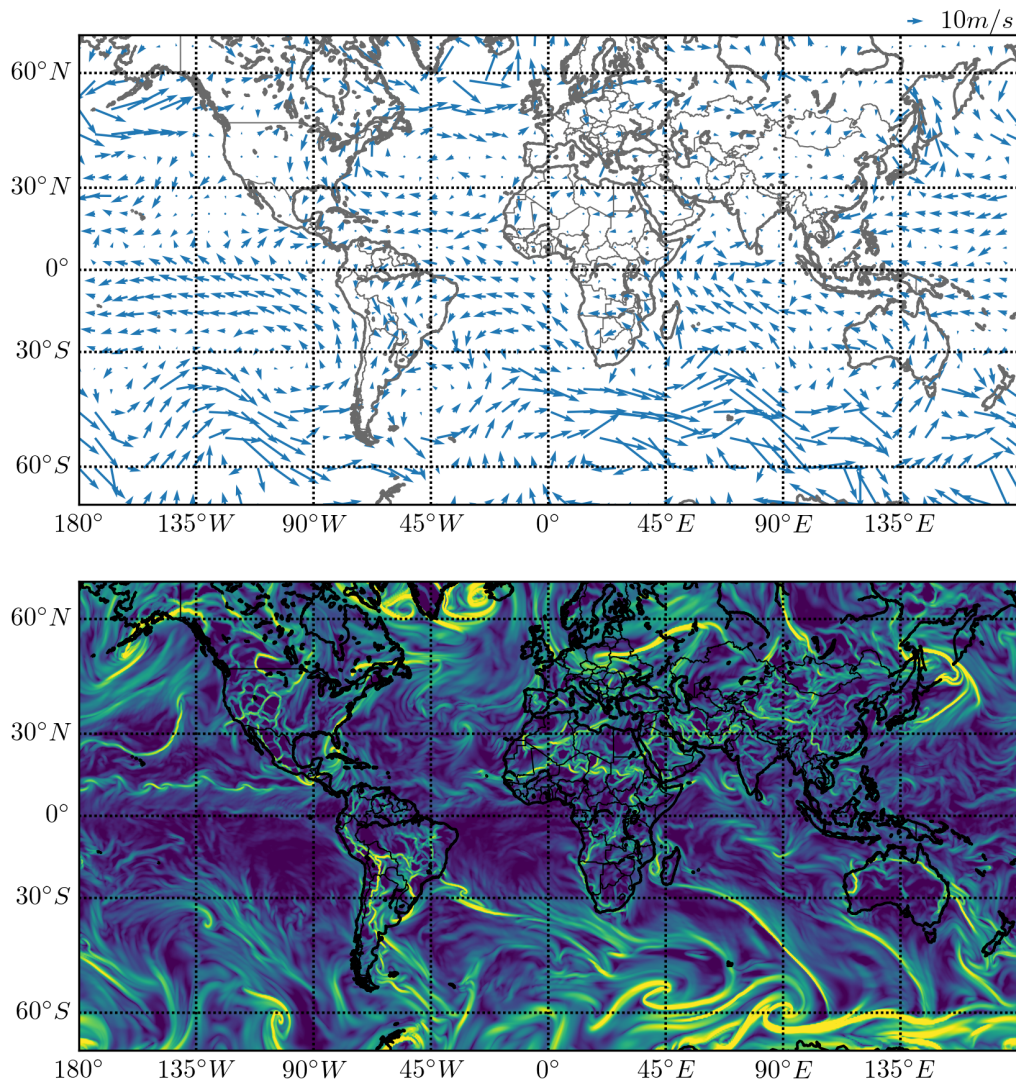


Figure 1.1: Top: Wind velocity field along 925 mb pressure surface from a simulation of the global atmosphere, approximately 760 m above sea level. Bottom: Backward-time FTLE field, with an integration time of 24 hr. Regions in yellow are where fluid parcels are most likely to converge over the next 24 hr.

The diagnostics used to locate these transport structures have historically been Lagrangian in nature, such as FTLE and Lagrangian coherent structures (LCSs). The FTLE provides a measure of how much fluid parcels stretch over an integration period. LCSs, on the other hand, are co-dimension 1 material surfaces which represent the material lines where fluid

parcel stretching is maximized; as such they are often identified as ridge-lines of the FTLE field. Being Lagrangian, these tools require the integration of fluid parcel trajectories. This reliance on trajectory integration makes Lagrangian diagnostics time consuming to calculate and computationally expensive. Additionally, the accurate integration of fluid parcel trajectories requires a velocity field which is sufficiently resolved in both time and space. While this requirement is not a major obstacle for the analysis of ocean surface flows, due to velocity measurements from devices such as high frequency radar and satellites, it is problematic for atmospheric and subsurface oceanic flows. This means that the analysis of these flows rely on the use of velocity fields from numerical models. Numerical models themselves take time to compute, which limits their usefulness in real-time applications. Additionally, numerical models can be computationally expensive, may not accurately capture sub-grid scale phenomena, and at best are still an approximation of the true situation.

Over the past few years new Eulerian diagnostics, such as objective Eulerian coherent structures (OECS) [12] and the trajectory divergence rate [13], have been developed. These Eulerian diagnostics are based on gradients of the velocity field, rather than fluid parcel trajectories. As such, Eulerian diagnostics are faster to compute and less computationally expensive. Furthermore, as will be shown in chapter 4, these diagnostics can be calculated from velocity data at as few as  $n + 1$  points in an  $n$ -dimensional space and 1 point in time. This makes them easy to calculate from experimental measurements of geophysical flows, such as those in the atmosphere.

Due to their relative novelty, there is still much that is unknown about the relationship between Eulerian and Lagrangian diagnostics. It is at this interface of Eulerian and Lagrangian analysis that this dissertation makes an impact. In particular this dissertation will:

- prove rigorous mathematical connections between Lagrangian and Eulerian diagnostics for  $n$ -dimensional systems,

- formulate a new Eulerian diagnostic, the infinitesimal-time LCS (iLCS),
- explore the ability of Eulerian diagnostics to detect Lagrangian dynamics,
- develop a new method to measure local Eulerian diagnostics using a single fixed-wing unmanned aircraft system (UAS),
- apply new Eulerian diagnostics to real-world experimental data, combining UAS and ground-based measurements, to look for indications of LCSs.

These developments are presented over the course of three chapters. These chapters can be thought of as representing theoretical, numerical, and experimental advances in the field of dynamical systems theory, focusing on the relationship between Eulerian and Lagrangian diagnostics. Each of these three chapters has either been published, submitted for publication, or is currently in preparation for journal submission.

## 1.2 Governing equations

This dissertation examines the dynamical system,

$$\frac{d}{dt}\mathbf{x}(t) = \mathbf{v}(\mathbf{x}(t), t), \quad (1.1)$$

$$\mathbf{x}_0 = \mathbf{x}(t_0), \quad (1.2)$$

$$\mathbf{x}(t) \in \mathbb{R}^n, t \in \mathbb{R}, \quad (1.3)$$

where  $\mathbf{x}(t)$  is the position of a fluid parcel at time  $t$ ,  $\mathbf{v}(\mathbf{x}(t), t)$  is the velocity of the fluid flow at position  $\mathbf{x}(t)$  at time  $t$ , and  $\mathbb{R}$  is the set of real numbers.

Analysis of this system by Lagrangian methods begins with calculating the flow map,

$$\mathbf{F}_{t_0}^t(\mathbf{x}_0) = \mathbf{x}_0 + \int_{t_0}^t \mathbf{v}(\mathbf{x}(t), t) dt. \quad (1.4)$$

Taking the gradient of the flow map, the right Cauchy-Green strain tensor is then calculated,

$$\mathbf{C}_{t_0}^t(\mathbf{x}_0) = \nabla \mathbf{F}_{t_0}^t(\mathbf{x}_0)^T \cdot \nabla \mathbf{F}_{t_0}^t(\mathbf{x}_0), \quad (1.5)$$

with ordered eigenvalues,  $\lambda_1 < \dots < \lambda_n$ , each of which is associated with a normalized eigenvector,  $\boldsymbol{\xi}_{\lambda_i}$ ,  $i \in [1, n]$ . From the largest eigenvalue of the right Cauchy-Green strain tensor,  $\lambda_n$ , the FTLE field is derived,

$$\sigma_{t_0}^t(\mathbf{x}_0) = \frac{1}{2|t - t_0|} \log(\lambda_n(\mathbf{x}_0)). \quad (1.6)$$

Ridges of this field can then be identified as LCSs. While there are different mathematical definitions for what constitutes a ridge, a ridge-line can be thought of as the generalization of the concept of a local maxima. Following [14], this dissertation identifies LCSs as C-ridges of the FTLE field. C-ridges are ridge-lines of the FTLE which are orthogonal to the direction of maximal stretching. Mathematically, they are defined as,

$$\sigma > 0, \quad (1.7)$$

$$\nabla \sigma \cdot \boldsymbol{\xi}_{\lambda_n} = 0, \quad (1.8)$$

$$(\mathbf{H}_\sigma \cdot \boldsymbol{\xi}_{\lambda_n}) \cdot \boldsymbol{\xi}_{\lambda_n} < 0, \quad (1.9)$$

where  $\mathbf{H}_\sigma$  is the Hessian matrix of the FTLE field. C-ridges are advantageous over other forms of FTLE ridges, as they only rely on invariants of the Cauchy-Green strain tensor and were shown in [14] to be equivalent to the variational definition hyperbolic LCSs described

in [15].

The main contributions of this dissertation are based the use of Eulerian methods and the connection between Eulerian and Lagrangian diagnostics. These Eulerian methods derive primarily from the Eulerian rate-of-strain tensor,

$$\mathbf{S}(\mathbf{x}_0, t_0) = \frac{1}{2} (\nabla \mathbf{v}(\mathbf{x}_0, t_0) + \nabla \mathbf{v}(\mathbf{x}_0, t_0)^T), \quad (1.10)$$

with ordered eigenvalues  $s_1 < \dots < s_n$ . The minimum eigenvalue,  $s_1$ , is the attraction rate; while the maximum,  $s_n$ , is the repulsion rate.

### 1.3 Research overview

This dissertation presents the results of three research projects over the course of three chapters. These chapters each advance the understanding of material transport in a distinct way.

Chapter 2 is largely a theoretical work, with some numerics. This chapter builds a mathematical bridge between traditional Lagrangian diagnostics and newer Eulerian diagnostics. It lays out rigorous mathematical proofs which show that the attraction rate is the limit of the backward-time FTLE and the repulsion rate is the limit of the forward-time FTLE as the integration time goes to zero. Building upon this discovery, a new Eulerian diagnostic, iLCS, is formulated. In addition to this, equations for higher order approximations to the FTLE are derived using Taylor series expansions and Rivlin-Ericksen tensors. These advances are then applied to a series of examples, including standard analytical models used in the LCS literature, a realistic geophysical flow, and two 3-dimensional analytic flows. This chapter is currently being prepared for journal submission to either *Chaos*, *PhysicaD*, or *Nonlinear*

*Dynamics.*

Chapter 3 is mostly a numerical work. This chapter lays the groundwork for being able to detect LCSs from a single fixed-wing UAS. Towards this end, a new algorithm is developed which calculates the gradient of a scalar field from measurements taken along a circular arc. An observing system simulation experiment (OSSE) is then conducted to determine if it is possible to use wind velocity measurements from a circling UAS to approximate local Eulerian diagnostics at the center-point of the UAS orbit. After this, a parametric study is performed to determine if it is possible to utilize Eulerian diagnostics to infer Lagrangian dynamics. Finally, these two ideas are combined to see if it is possible to infer local Lagrangian dynamics from UAS measurements. This chapter has been submitted to the journal *Sensors* for publication.

Chapter 4 is an analysis of experimental measurements and numerical models. Over the summer of 2018, an experimental campaign was conducted in the San Luis Valley, Co, in association with the with the International Society for Atmospheric Research using Remotely-Piloted Aircraft conference [16], where UASs and ground-based sensors were used to measure local atmospheric conditions. During this campaign several missions were conducted which simultaneously measured the atmospheric velocity at three points. From these measurements, the gradient of the local atmospheric velocity is able to be approximated. This then allows for the calculation of the Eulerian rate-of-strain tensor and hence Eulerian diagnostics. These calculations are then compared to Eulerian diagnostics computed from a numerical atmospheric fluid model of the San Luis Valley in order to look for signs of LCSs. This chapter has been published in the journal *Sensors* [17].

## 1.4 Research not covered in this dissertation

This section presents an overview of the projects that have been pursued over the past four years, but did not become a core component of this dissertation. Some these projects morphed into projects that did become central to this dissertation, others were passed over in favor of more productive lines of research, and still others, while fruitful, were simply beyond the scope of this dissertation. However, all these projects are worth mentioning and have contributed to the institutional knowledge of Ross Dynamics Lab.

### 1.4.1 3D atmospheric Lagrangian coherent structures

The study of 3D atmospheric LCSs was originally intended to be a rather significant portion of this dissertation. Many months were spent learning how to setup and run the realistic Weather Research and Forecasting (WRF) model [18]. Unfortunately, the challenges of accurately fine tuning a model with scores of parameters were beyond the scope of current lab research. In its place, the output from other models were used, such as the North American Mesoscale (NAM) WRF model, which had been used in previous lab research. Additionally, model results provided by more experienced atmospheric modelers, such as Dr. Hosein Foroutan at Virginia Tech and Nevio Babic and Ross Palomaki at the De Wekker lab at the University of Virginia, have also been used. Still, this line of research produced many interesting results. Analysis of the 3D backward-time FTLE field from a convective boundary layer (CBL) simulation showed that LCSs can likely be used to track the entrainment of material from ground level into the atmosphere. This can be seen in animations [FTLE field video](#) and [FTLE isosurface video](#), stills of these animations can be found in figures 1.2 and 1.3. These animations show that regions of elevated FTLE values tend to be advected upward. These elevated FTLE values are likely associated with convective plums. Looking

at the statistics of the 3D backward-time FTLE field, figure 1.4, showed that there were clear elevations of FTLE values at the top and bottom of the CBL. This suggests that fluid parcels can be expected to converge towards either the ground or the top of the CBL. An animation of these FTLE statistics along with the variance of the velocity field can be found at [FTLE statistics video](#). Additionally, figure 1.5 shows the intersection of attracting and repelling 3D LCSs, highlighting saddle-point-like behavior in the CBL. An animation of this intersection can be found at [LCS saddle video](#). Note how the LCSs and tracers converge to the top of the CBL over time. This line of research culminated in the fall of 2018, with the extraction of 2-dimensional attracting LCSs using wind velocity data from a portion of the NAM model over Blacksburg VA. This result can be found in figure 1.6, which shows both horizontal and vertical LCSs. Previous work had typically assumed atmospheric LCSs would be vertical structures due to the horizontal wind components being two orders of magnitude greater than the vertical wind component, on average.

In addition to these results, studying the mathematics of 3D LCSs directly lead to the formulation of iLCS during the summer of 2018. This was done by applying methodology of  $n$ -dimensional LCSs to Eulerian diagnostics first began in [12]. iLCS form a prominent part of this dissertation and are discussed in chapter 2.

This 3D LCS research resulted in a talk at the 2017 *SIAM Conference on Applications of Dynamical Systems* [19].

### **1.4.2 Detection of atmospheric Lagrangian coherent structures via sonic detection and ranging**

The detection of LCSs from experimental data has been a focus of research since starting in the Ross Dynamics Lab. Earlier on, access to sonic detection and ranging (SoDAR) data

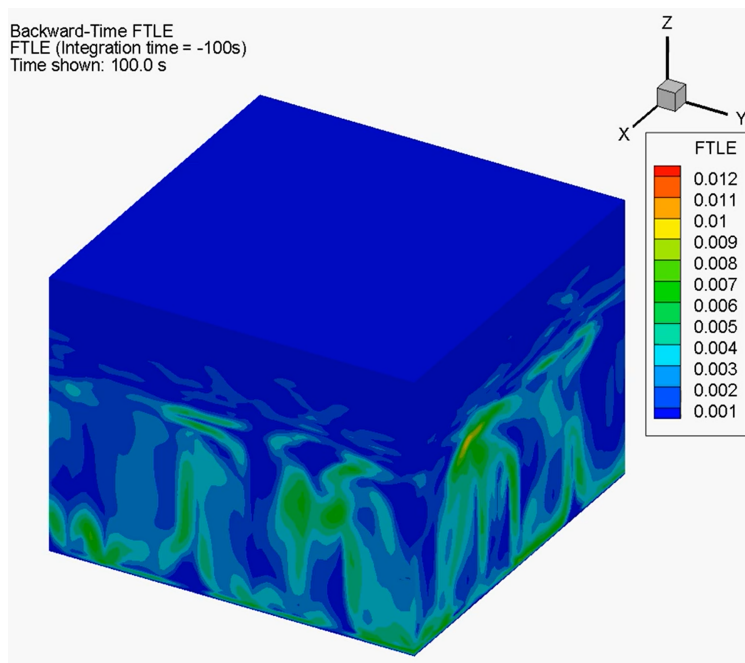


Figure 1.2: 3D backward-time FTLE field from a CBL simulation. Colorbar has units of  $\text{s}^{-1}$ . An animation of this flow can be found at <https://www.youtube.com/watch?v=mTmdv-Kvz7Y>.

led to the idea of using multiple SoDAR units to measure a volumetric 3D velocity field. These velocity measurements would then be analyzed to attempt to detect the passage of LCSs through the sampling area. Due to a limited number of available SoDAR devices, the decision was made to explore whether a single SoDAR could be used to detect LCSs passing through the sampling area. This idea was tested using a WRF large eddy simulation (LES). A simulated SoDAR model was formulated which took a 1-dimensional velocity profile from the WRF-LES and assumed horizontal homogeneity (i.e., the wind velocity was not changing in the horizontal plane). This was then used to calculate an FTLE field.

Results from these efforts seemed to suggest that a single SoDAR might indeed be used to detect LCSs. This can be seen in figure 1.7, which shows the results of a simulated SoDAR numerical experiment. The left hand side shows a time series of the FTLE field as calculated from velocity measurements performed by a simulated SoDAR. The right hand side shows

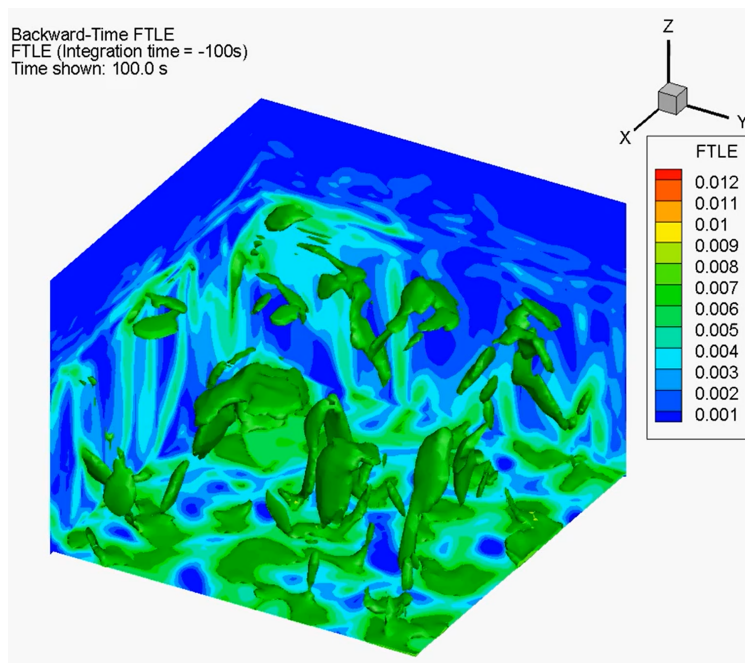


Figure 1.3: Isosurfaces of a 3D backward-time FTLE field from a CBL simulation. Colorbar has units of  $\text{s}^{-1}$ . An animation of this flow can be found at <https://www.youtube.com/watch?v=9FEBGTPSmio>.

FTLE isosurfaces as calculated from the fully 3-dimensional velocity field. The magenta dot highlights an elevated FTLE value that appears in both the SoDAR model and the fully 3D FTLE field. This correspondence seems to suggest that velocity measurements from a 1-dimensional profile, such as those of a SoDAR or light detection and ranging (LiDAR) device, can be used to detect LCSs.

This line of research was eclipsed by research utilizing UASs to detect LCSs. While platforms such as SoDAR and LiDAR are a useful for platform for making continuous measurements of the wind at a given location, UASs are a less expensive, more portable, and more readily available platform. Work on detecting LCSs from wind measurements performed by UASs can be found in chapters 3 and 4.

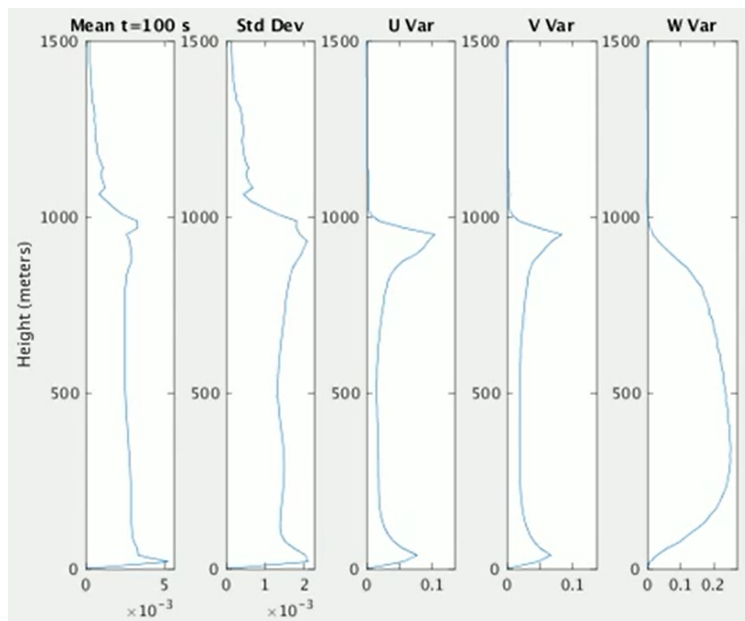


Figure 1.4: Mean and standard deviation of a 3D backward-time FTLE field from a CBL simulation. The variance of the velocity component fields are shown as well. An animation of this figure can be found at <https://www.youtube.com/watch?v=FgV-1tVDd0w>.

### 1.4.3 Lagrangian coherent structures and pollution transport

Work on the study of LCSs and their ability to predict the transportation of pollution in the atmosphere began in the summer of 2017. Dr. William Vance at the California Air Resources Board (CARB) contacted the Ross Dynamics Lab to analyze a pollution event that had happened the previous year. In June 2016, an elevated level of ozone was detected near the city of Visalia in the San Joaquin Valley, California. It was speculated that the ozone had been transported to California from forest fires in Asia. CARB was interested to see if LCSs had played any roll in the ozone’s transport. The velocity field of the 800 mb pressure surface from a NAM simulation of that time period was analyzed. While there were LCSs present over the San Joaquin Valley during that time span, it did not appear that they were associated with the elevated ozone measurements. However, during this analysis an interesting intersection of attracting and repelling LCSs was noticed over the San Francisco

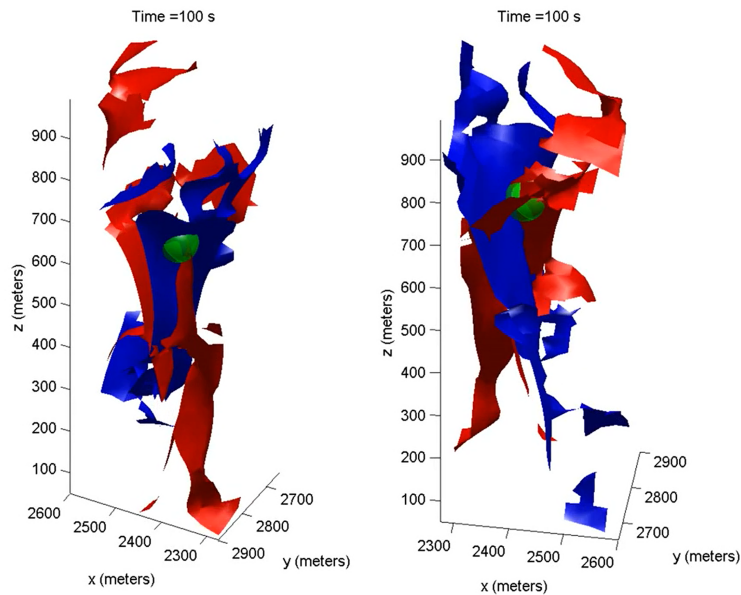


Figure 1.5: Intersection of an attracting (blue) LCS and a repelling (red) LCS from a CBL simulation. A blob of passive tracers is shown in green. An animation of these structures can be found at <https://www.youtube.com/watch?v=NflrLXB6Gbc>.

Bay Area, figure 1.8. Investigating this feature more deeply revealed that it had originated over the Pacific Ocean and eventually wound up entangled in the Sierra Nevada mountains. An interesting observation from this study is that LCSs start off as ordinary material surfaces advecting with the flow. While they advect with the flow, there comes a point where these material surfaces appear to activate; the attracting LCSs begin to attract particles and the repelling LCSs begin to repel particles. After some time has passed, these material surfaces then deactivate (i.e. they cease to attract or repel) and revert to passively advecting with the flow. An animation of this activation and deactivation can be seen at [California saddle video](#). While this particular line of research did not lead to much, it did set the stage for the research the role of LCSs in the transport of atmospheric species using more sophisticated techniques.

A key strength of LCSs are their ability to predict how material advected by a geophysical fluid flow will be transported [5, 9]. However, visualizing these structures can be challenging

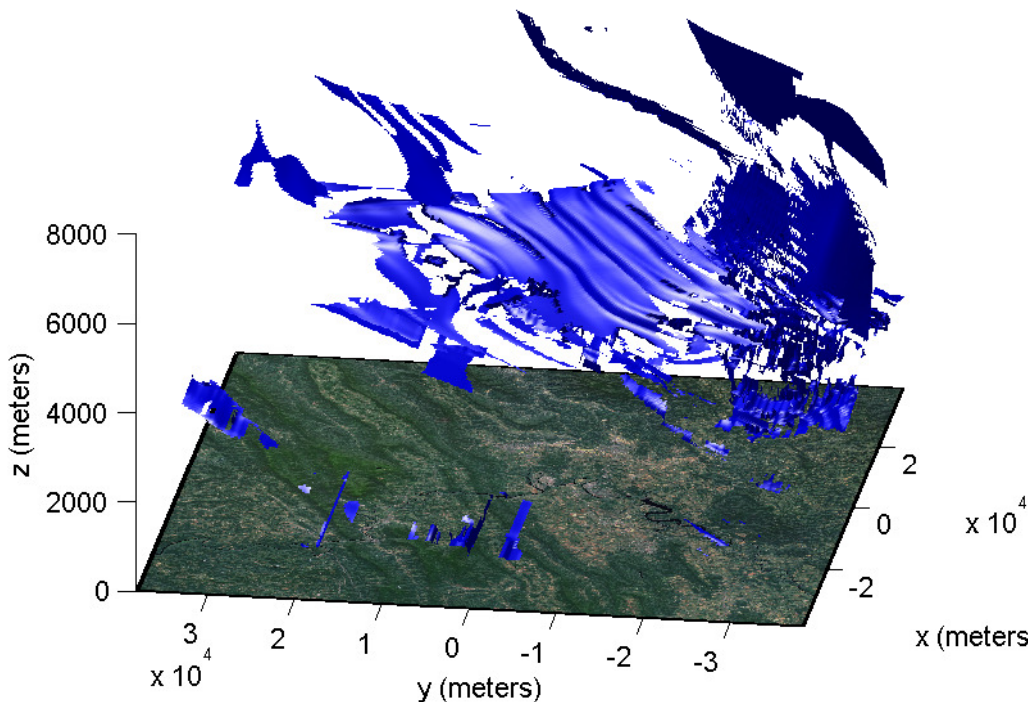


Figure 1.6: 3D atmospheric attracting LCSs above Blacksblack VA. This image shows that 3D atmospheric LCSs come in both horizontal and vertical structures. Note that the  $y$  axis corresponds to North, and the  $x$  axis to East.

in systems with  $n > 2$  dimensions, such as the atmosphere. This can make predicting how material in a flow, such as species in the atmosphere, will advect more difficult. One solution to this problem was presented in [11], which used a material-weighted vertically averaged velocity field to analyze atmospheric rivers; this turned a 3-dimensional problem into a 2-dimensional problem. This velocity field can be written as,

$$\mathbf{v} = \frac{1}{\int_0^1 q \frac{\partial p}{\partial \eta} d\eta} \begin{bmatrix} \int_0^1 u q \frac{\partial p}{\partial \eta} d\eta \\ \int_0^1 v q \frac{\partial p}{\partial \eta} d\eta \end{bmatrix} \quad (1.11)$$

where  $\eta$  is a hybrid vertical coordinate,  $p$  is the pressure level,  $u$  is the eastward wind velocity,

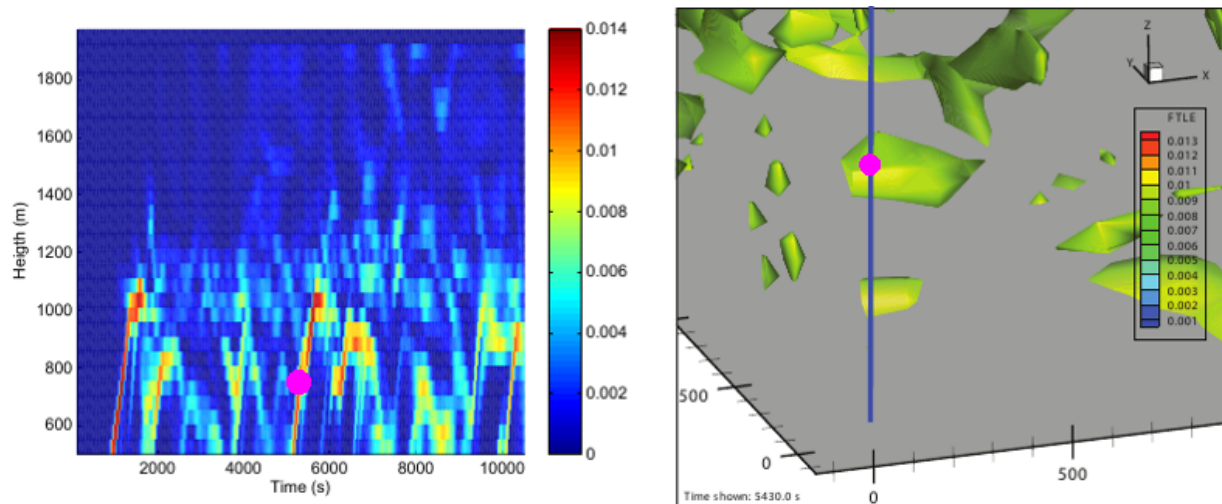


Figure 1.7: Results from numerical SoDAR experiments. Left: The FTLE profile calculated from 1D SoDAR model taken from a 3D WRF-LES. Right: The FTLE isosurfaces calculated from full 3D velocity field. Blue line simulated SoDAR sampling profile. Both colorbars have units  $s^{-1}$ .

$v$  is the northward wind velocity, and  $q$  is the material concentration at the pressure level  $p$ .

This has inspired new research looking at different atmospheric species in the place of water vapor. Thus far, the research on this topic has been promising. There have already been seven types of atmospheric species examined, including the three in figure 1.9. Transport structures of these seven species have been calculated for integration periods of 0, -1, and -6 hours. These structures were then compared to those of the 100 m wind field. While some species, such as water vapor, appear to have transport structures similar to that of the 100 m wind field, many have very different and unique structures. One such example is ozone, shown in figure 1.9(D), whose unique structures are due to having sources both near ground (e.g., urban air pollution) and high in the atmosphere (e.g. the ozone layer).

While still more work needs to be done, this research has already led to a poster at the 17<sup>th</sup> *Annual Community Modeling and Analysis System Conference* [20]. Additionally, results from this research will be presented at the upcoming 2019 *SIAM Conference on Applications*

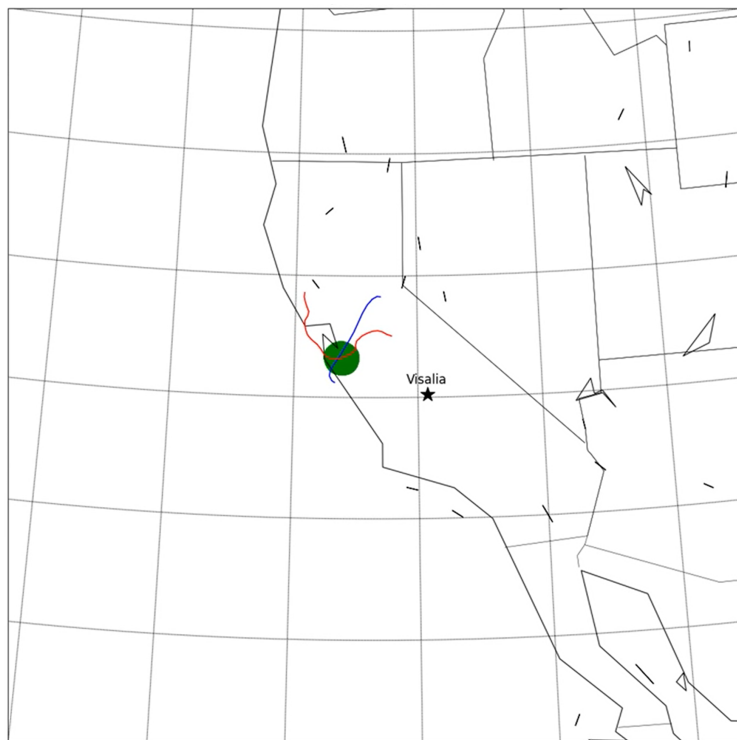


Figure 1.8: An intersection of attracting (blue) and repelling (red) LCSs over the San Francisco Bay Area, California. Passive tracers are shown in green. An animation of this figure, showing the saddle-point-like behavior of this intersection can be seen at <https://www.youtube.com/watch?v=fci3r0chMxw>.

*of Dynamical Systems* and will be submitted for journal publication.

#### 1.4.4 Hybrid Lagrangian coherent structures

Typically, when calculating Lagrangian diagnostics for a geophysical system,  $\mathbf{v}$  is the velocity of either the atmospheric winds or the oceanic currents. However, objects that exist at the interface of these fluids, such as ships, oil spills, persons in water, airplane debris, etc., are not exclusively transported by either of these two vector fields. In these situations a hybrid velocity field can be used to improve predictions of material transport [21]. This hybrid

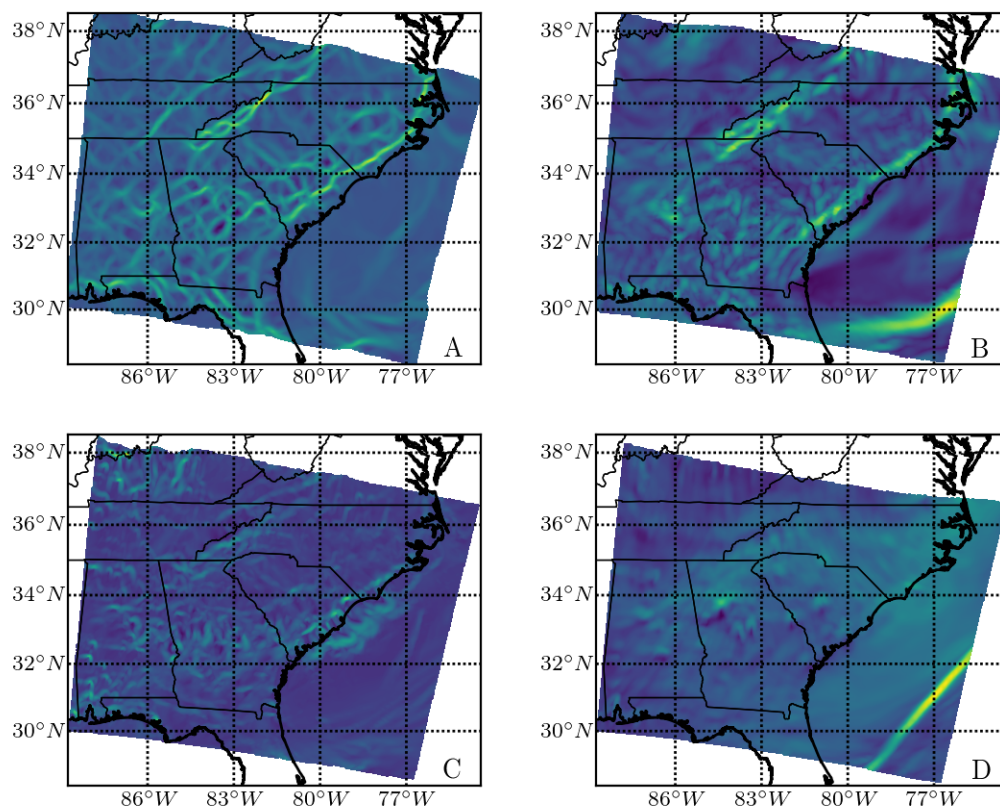


Figure 1.9: Comparison of -1 hr backward-time FTLE fields for different atmospheric species: A) horizontal wind, B) water vapor, C) nitrogen dioxide, D) ozone. The horizontal wind velocity field is taken from a horizontal level  $\sim 100$  m above ground level. The other three species are calculated based on column-averaged and species-weighted horizontal wind vector components. All four species have their own unique structures (yellow) where fluid parcels will converge.

velocity field can be written as,

$$\mathbf{v}(\mathbf{x}(t), t) = \mathbf{v}(\mathbf{x}(t), t)_{ocean} + C_w \mathbf{v}(\mathbf{x}(t), t)_{wind}, \quad (1.12)$$

where  $\mathbf{v}(\mathbf{x}(t), t)_{wind}$  is the wind speed at 10 m and  $C_w$  is the windage coefficient. The windage coefficient is a result of how large an object is, how much of it is acted on by the 10 m wind field and other physical characteristics [21].

Numerical and experiment work on this topic was done over the summer of 2018 in support

of the NSF ALPHA project [22]. This project used oceanic and atmospheric model data to calculate LCSs for ocean surface and hybrid velocity fields. Following [23], the windage coefficient for the hybrid field was set to 0.019 in order to model a person-in-water. The LCSs and tracers were then advected under equation 1.12. This was done to see if there was a noticeable difference between behavior of the oceanic and the hybrid flows. In addition to this, experimental work using partially submerged manakins and pure ocean drifters was performed off the coast of Martha’s Vineyard Massachusetts. While more analysis is needed, earlier results suggest that windage does make a noticeable difference; this is in agreement with the findings of [21]. Results from a simulation south of Martha’s Vineyard can be seen in figure 1.11.

The results of this project are currently in preparation for journal submission.

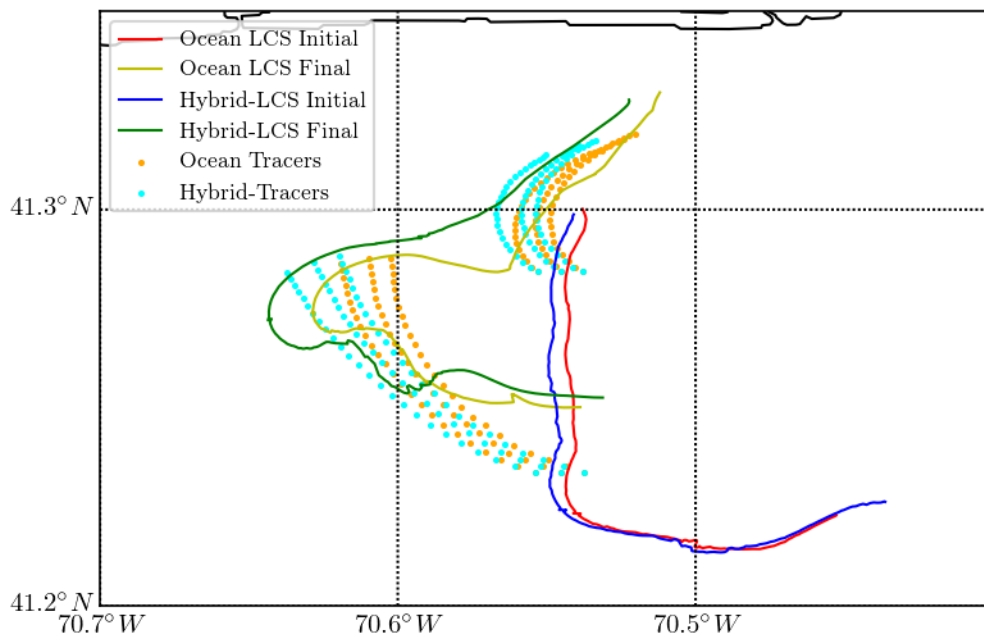


Figure 1.10: Comparison of an ocean LCS (red and yellow) and a hybrid LCS (blue and green) with a windage coefficient of 0.019 (the same windage coefficient as a person-in-water), south of Martha’s Vineyard, Massachusetts. It can be seen that tracers that are advected under the ocean current (orange) converge to the ocean LCS; while the tracers advected under the hybrid velocity field (cyan) converge to the hybrid LCS.

### 1.4.5 Trajectory divergence rate

The trajectory divergence rate grew out of the study of variational LCSs. It was developed as an instantaneous rate-of-change of the so called “repulsion rate” discussed in [15]. As an instantaneous rate-of-change, it provides a simultaneous measure of both attraction and repulsion in a fluid flow, or general  $n$ -dimensional vector field. The trajectory divergence rate is defined as,

$$\begin{aligned}\dot{\rho}(\mathbf{x}_0, t_0) &= \hat{\mathbf{n}}(\mathbf{x}_0, t_0)^T \cdot \mathbf{S}(\mathbf{x}_0, t_0) \cdot \hat{\mathbf{n}}(\mathbf{x}_0, t_0) \\ &= \frac{(\mathbf{v}(\mathbf{x}_0, t_0)^T \cdot \mathbf{J}^T \cdot \mathbf{S}(\mathbf{x}_0, t_0) \cdot \mathbf{J} \cdot \mathbf{v}(\mathbf{x}_0, t_0))}{\|\mathbf{v}(\mathbf{x}_0, t_0)\|^2},\end{aligned}\tag{1.13}$$

where  $\mathbf{S}(\mathbf{x}_0, t_0)$  is the Eulerian rate-of-strain tensor,  $\hat{\mathbf{n}}(\mathbf{x}_0, t_0)$  is the unit vector normal to the trajectory and  $\mathbf{J}$  is the symplectic matrix,  $\mathbf{J} = \begin{bmatrix} 0 & 1 \\ -1 & 0 \end{bmatrix}$ [13]. Areas where the trajectory divergence rate is  $> 0$  are where streamlines diverge; areas where the trajectory divergence rate is  $< 0$  are where streamlines converge.

Providing a metric of both attraction and repulsion in one scalar field makes the trajectory divergence rate a powerful tool for the analysis of dynamical systems. It has shown itself to be useful in the detection of slow manifolds and limit cycles. However, as shall be shown in chapter 3, it may not be the best diagnostic tool for the detection of LCSs in fluid flows.

While sensing the trajectory divergence rate from a UAS and using it to detect LCSs are explored in chapter 3, the theory behind it and the general applications of the trajectory divergence rate are not discussed. However, they can be found in [13].

This work contributed to one paper [13], published in *Nonlinear Dynamics*, and was influential on chapter 3 of this dissertation.

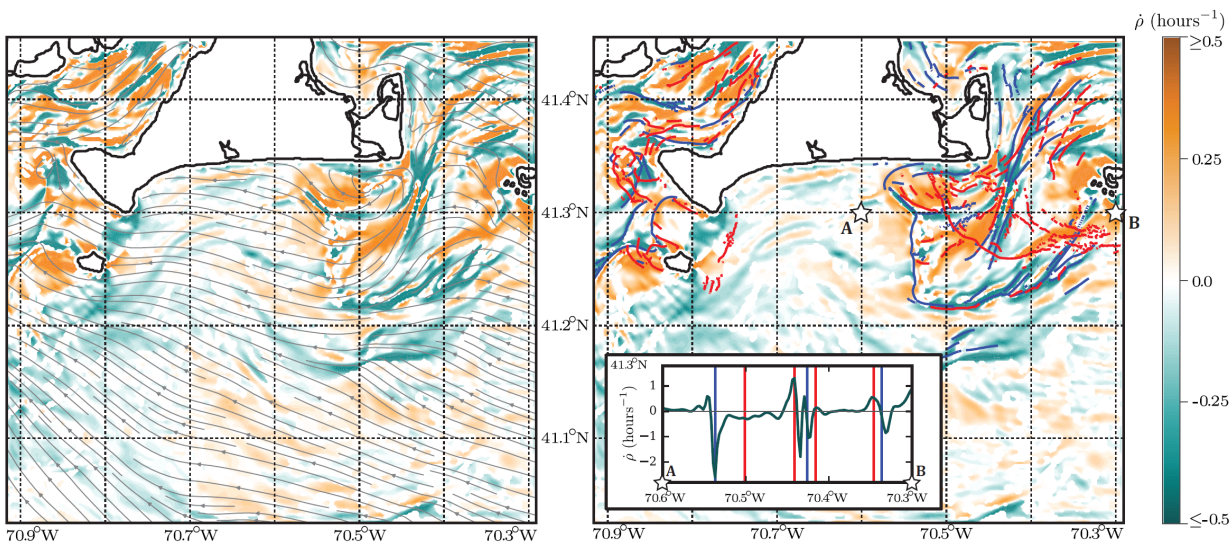


Figure 1.11: Left: depiction of the trajectory divergence rate along with streamlines from an MSEAS model [24] simulation of the oceanic flow around Martha’s Vineyard, Massachusetts. Areas in blue show where streamlines converge, while areas in orange show where streamlines diverge. Right: attracting LCSs (blue) and repelling LCSs (red) for an integration time of 2 hr are shown atop the trajectory divergence rate field. The inset plot shows the trajectory divergence rate along  $41.3^\circ\text{N}$  latitude from  $70.6^\circ\text{W}$  to  $70.3^\circ\text{W}$ , marked by the points A and B. Places where LCSs cross this latitude between A and B are shown as lines colored red for repelling and blue for attracting. Notice how the repelling LCSs tend to correspond to peaks in the trajectory divergence rate; while attracting LCSs correspond to troughs. This image was published in [13].

### 1.4.6 Reduced order modeling

One of the earlier topics considered for this dissertation was the application of Lagrangian diagnostics to the improvement of reduced order models (ROMs). Traditional direct numerical simulation (DNS) models can produce highly accurate results, however these results can be time consuming to calculate and computationally expensive. This has led to the development of ROMs. ROMs approximate the solution to a system by sampling DNS solutions and decomposing those solutions, with respect to some metric, to generate new basis functions. These new basis functions vary in space and have unknown coefficients which vary in time. This creates a new autonomous ordinary differential equation which is less

computationally expensive and time consuming to solve.

In the past, ROMs have been Eulerian based, typically applying a metric, such as the  $L^2$  norm, to an Eulerian quantity, such as the vorticity field. The idea to include Lagrangian information when generating a ROM was spurred by the development of a new inner product, which incorporates Lagrangian information. This inner product is

$$((\omega_1, \sigma_1), (\omega_2, \sigma_2))_{\text{FTLE}} = \int_{\Omega} (\omega_1(\mathbf{x})\omega_2(\mathbf{x}) + \alpha\sigma_1(\mathbf{x})\sigma_2(\mathbf{x})) \, d\mathbf{x}, \quad (1.14)$$

where the  $\omega_i$ 's are vorticity fields, the  $\sigma_i$ 's are FTLE fields, and  $\alpha$  is a weighting parameter. To study the effectiveness of the Lagrangian ROM at reproducing Lagrangian information, a parametric study was performed using the quasi-geostrophic flow. This study looked at how well the ROM was able to reproduce the FTLE field generated by the DNS for different values of  $\alpha$ . The value of  $\alpha$  was varied from 0 to  $10^4$ . This study found that not only does the Lagrangian ROM outperform the Eulerian ROM, but that there may be an optimal value of  $\alpha$ .

This research resulted in one paper [25], currently under review at the *International Journal for Numerical Methods in Fluids*, and an NSF grant [26].

# Bibliography

- [1] Phanindra Tallapragada, Shane D Ross, and David G Schmale III. Lagrangian coherent structures are associated with fluctuations in airborne microbial populations. *Chaos*, 21:033122, 2011.
- [2] David G Schmale III and Shane D Ross. Highways in the sky: Scales of atmospheric transport of plant pathogens. *Annual Review of Phytopathology*, 53:591–611, 2015.
- [3] David G Schmale III and Shane D Ross. High-flying microbes: Aerial drones and chaos theory help researchers explore the many ways that microorganisms spread havoc around the world. *Scientific American*, February:32–37, 2017.
- [4] Amir E BozorgMagham, Shane D Ross, and David G Schmale III. Local finite-time Lyapunov exponent, local sampling and probabilistic source and destination regions. *Nonlinear Processes in Geophysics*, 22(6):663–677, 2015.
- [5] Jifeng Peng and Rorik Peterson. Attracting structures in volcanic ash transport. *Atmospheric environment*, 48:230–239, 2012.
- [6] Wenbo Tang, Pak Wai Chan, and George Haller. Lagrangian coherent structure analysis of terminal winds detected by LiDAR. Part I: Turbulence structures. *Journal of Applied Meteorology and Climatology*, 50(2):325–338, 2011.

- [7] Marilena Kampa and Elias Castanas. Human health effects of air pollution. *Environmental pollution*, 151(2):362–367, 2008.
- [8] C Arden Pope III, Richard T Burnett, Michael J Thun, Eugenia E Calle, Daniel Krewski, Kazuhiko Ito, and George D Thurston. Lung cancer, cardiopulmonary mortality, and long-term exposure to fine particulate air pollution. *JAMA*, 287(9):1132–1141, 2002.
- [9] María J Olascoaga and George Haller. Forecasting sudden changes in environmental pollution patterns. *Proceedings of the National Academy of Sciences*, 109(13):4738–4743, 2012.
- [10] Thomas Peacock and George Haller. Lagrangian coherent structures: The hidden skeleton of fluid flows. *Physics today*, 66(2):41, 2013.
- [11] Daniel Garaboa-Paz, Jorge Eiras-Barca, Florian Huhn, and Vicente Pérez-Muñuzuri. Lagrangian coherent structures along atmospheric rivers. *Chaos: An Interdisciplinary Journal of Nonlinear Science*, 25(6):063105, 2015.
- [12] Mattia Serra and George Haller. Objective Eulerian coherent structures. *Chaos: An Interdisciplinary Journal of Nonlinear Science*, 26(5):053110, 2016.
- [13] Gary K Nave Jr, Peter J Nolan, and Shane D Ross. Trajectory-free approximation of phase space structures using the trajectory divergence rate. *Nonlinear Dynamics*, 2019.
- [14] Ronald Peikert, Benjamin Schindler, and Robert Carneky. Ridge surface methods for the visualization of Lagrangian coherent structures. In *Proceedings of the Ninth International Conference on Flow Dynamics, Sendai, Japan*, pages 206–207, 2012.
- [15] George Haller. A variational theory of hyperbolic Lagrangian coherent structures. *Physica D: Nonlinear Phenomena*, 240(7):574–598, 2011.

- [16] International society for atmospheric research using remotely -piloted aircraft. <http://www.isarra.org>. Accessed: 2019-03-07.
- [17] Peter J Nolan, James Pinto, Javier González-Rocha, Anders Jensen, Christina Vezzi, Sean Bailey, Gijs de Boer, Constantin Diehl, Roger Laurence, Craig Powers, Hosein Foroutan, Shane D Ross, and David G Schmale III. Coordinated unmanned aircraft system (UAS) and ground-based weather measurements to predict Lagrangian coherent structures (LCSs). *Sensors*, 18(12):4448, 2018.
- [18] Weather research and forecasting model. <https://www.mmm.ucar.edu/weather-research-and-forecasting-model>. Accessed: 2019-02-02.
- [19] 2017 siam conference on applications of dynamical systems. <https://archive.siam.org/meetings/ds17>. Accessed: 2019-03-07.
- [20] Peter J Nolan, Hosein Foroutan, and Shane D Ross. The understanding of pollutant transport in the atmosphere: Lagrangian coherent structures. Poster presented at the *17th Annual CMAS Conference*, October 2018. [https://cmascenter.org/conference//2018/slides/foroutan\\_understanding\\_pollutant\\_2018.pdf](https://cmascenter.org/conference//2018/slides/foroutan_understanding_pollutant_2018.pdf).
- [21] Michael R Allshouse, Gregory N Ivey, Ryan J Lowe, Nicole L Jones, CJ Beegle-Krause, Jiangtao Xu, and Thomas Peacock. Impact of windage on ocean surface Lagrangian coherent structures. *Environmental Fluid Mechanics*, 17(3):473–483, 2017.
- [22] Thomas Peacock, Pierre Lermusiaux, Shane D Ross, Irina Rypina, and Shawn Shadden. Hazards SEES: Advanced Lagrangian methods for prediction, mitigation and response to environmental flow hazards. NSF grant #1520825, 2015. [https://www.nsf.gov/awardsearch/showAward?AWD\\_ID=1520825](https://www.nsf.gov/awardsearch/showAward?AWD_ID=1520825).
- [23] Arthur A Allen. Leeway divergence. Technical Report CG-D-05-05, U.S. Coast Guard

- Research and Development Center, Groton, Connecticut, January 2005. <https://apps.dtic.mil/dtic/tr/fulltext/u2/a435435.pdf>.
- [24] Michela De Dominicis, Silvia Falchetti, Francesco Trotta, Nadia Pinardi, Luca Giacomelli, Ernesto Napolitano, Leopoldo Fazioli, Roberto Sorgente, Patrick J Haley Jr, Pierre FJ Lermusiaux, Flavio Martins, and Michele Cocco. A relocatable ocean model in support of environmental emergencies. *Ocean Dynamics*, 64(5):667–688, 2014.
- [25] Xuping Xie, Peter J Nolan, Shane D Ross, and Traian Iliescu. Lagrangian data-driven reduced order modeling of finite time Lyapunov exponents, 2019. <https://arxiv.org/abs/1808.05635>.
- [26] Traian Iliescu and Shane D Ross. Data-driven computation of Lagrangian transport structure in realistic flows. NSF grant #1821145, June 2018. [https://www.nsf.gov/awardsearch/showAward?AWD\\_ID=1821145](https://www.nsf.gov/awardsearch/showAward?AWD_ID=1821145).

## Chapter 2

# Finite-time Lyapunov exponent field in the infinitesimal time limit

### Attribution

This manuscript represents a collaborative work with Shane D. Ross which is currently in preparation for submission to either *Chaos*, *PhysicaD*, or *Nonlinear Dynamics*.

### Abstract

Lagrangian diagnostics, such as the finite-time Lyapunov exponent and Lagrangian coherent structures, have become popular tools for analyzing unsteady fluid flows. These diagnostics can help illuminate regions where fluid parcels transported by a flow will converge to and diverge from. Unfortunately, calculating Lagrangian diagnostics can be time consuming and computationally expensive. Recently new Eulerian diagnostics, such as objective Eulerian

coherent structures and the trajectory divergence rate, have been developed which are faster and less expensive to compute. Because Eulerian diagnostics are so new, there is still much about their connection to Lagrangian diagnostics that is unknown. This manuscript will provide a mathematical bridge between Lagrangian and Eulerian diagnostics. It will rigorously explore the deep mathematical relationship that exists between invariants of the Cauchy-Green strain tensor and the Eulerian rate-of-strain tensor in the infinitesimal time limit. Additionally, this manuscript will develop a new Eulerian diagnostic, infinitesimal-time Lagrangian coherent structures, and show its efficacy in predicting the Lagrangian transport of fluid parcels.

## 2.1 Introduction

Lagrangian diagnostics, such as the finite-time Lyapunov exponent (FTLE) and Lagrangian coherent structures, have become a popular means of analyzing unsteady fluid flows [1, 2, 3, 4, 5, 6, 7, 8, 9, 10, 11, 12, 13, 14, 15]. These diagnostics can help to predict how particles will spread in a fluid flow over a time interval of interest, as well as which areas of the flow will undergo the greatest and least amounts of stretching. However, Lagrangian methods rely on the integration of particle trajectories; this can make them computationally expensive and time consuming to calculate. Furthermore, the integration of particle trajectories requires a velocity field which is sufficiently resolved in both time and space in order to accurately calculate the particle's motion. This limits the ability of researchers to compute Lagrangian diagnostics from geophysical data, such as wind measurements, requiring the use of computer generated models instead. Unfortunately, model data itself takes time to generate, limiting its usefulness for real-time applications, such as a hazardous incident (e.g. a radioactive gas leak or an oil spill). Furthermore, even when model data is readily available it may not be

completely reliable. Thus new methods of analyzing unsteady fluid flows are required.

Recent Eulerian diagnostics, such as objective Eulerian coherent structures (OECS) [16], the trajectory divergence rate [17], and the attraction and repulsion rates [18], have been developed to analyze unsteady fluid flows. These diagnostics are derived from the Eulerian rate-of-strain tensor, which is calculated from gradients of the velocity field. This allows for dynamical systems to be analyzed without the need for particle integration, which reduces the amount of time and computational power, necessary to calculate. Furthermore, being based on gradients, these diagnostics can be calculated from measurements at as few as  $n + 1$  points in an  $n$  dimensional space, and 1 point in time. For example [18] calculated the attracting rate field in 2D using only 3 points in space.

This manuscript will build upon earlier work and lay a rigorous foundation which proves deep mathematical connections between the traditional Lagrangian diagnostics and the new Eulerian diagnostics. In addition to this, higher order Eulerian approximations to the FTLE field than those currently available will be derived, for short integration times. Building upon these proofs a new Eulerian diagnostic tool will be defined, infinitesimal-time LCS (iLCS). iLCSs will be shown to be the limit of LCSs as integration time goes to 0. Note that these proofs and iLCSs are generalized for  $n$  dimensional systems.

This manuscript is organized as follows. Section 2.2 gives information on the dynamical system that will be examined, along with the various notion. Section 2.3 provides a rigorous mathematical connection between invariants of the Eulerian rate-of-strain tensor and traditional Lagrangian diagnostics including the FTLE field and the eigenvectors of the right Cauchy-Green strain tensor. Section 2.4 derives a new Eulerian diagnostic, iLCSs, as the limit of LCSs as the integration time goes to 0. Then section 2.5 provides numerous examples, comparing the error of Eulerian approximation, demonstrating the effectiveness of iLCSs, and comparing the attraction rate field to the FTLE field. Finally, section 2.6 concludes the

manuscript.

## 2.2 Setup and Notation

Consider the dynamical system

$$\frac{d}{dt}\mathbf{x}(t) = \mathbf{v}(\mathbf{x}(t), t), \quad (2.1)$$

$$\mathbf{x}_0 = \mathbf{x}(t_0), \quad (2.2)$$

$$\mathbf{x} \in \mathbb{R}^n, t \in \mathbb{R}. \quad (2.3)$$

This system can be analyzed using Lagrangian methods, by first calculating the flow map for some time period of interest,  $[t_0, t]$ . The flow map is given by,

$$\mathbf{F}_{t_0}^t(\mathbf{x}_0) = \mathbf{x}_0 + \int_{t_0}^t \mathbf{v}(\mathbf{x}(t), t) dt. \quad (2.4)$$

Taking the gradient of the flow map, the right Cauchy-Green strain tensor for the time period of interest can be calculated,

$$\mathbf{C}_{t_0}^t(\mathbf{x}_0) = \nabla \mathbf{F}_{t_0}^t(\mathbf{x}_0)^T \cdot \nabla \mathbf{F}_{t_0}^t(\mathbf{x}_0), \quad (2.5)$$

the eigenvalues of which are

$$\lambda_1 < \lambda_2 < \dots < \lambda_n, \quad (2.6)$$

and are associated with the normalized eigenvectors

$$\boldsymbol{\xi}_{\lambda_i} \quad i \in \{1, \dots, n\}. \quad (2.7)$$

From the maximum eigenvalue of the Cauchy-Green tensor the FTLE can be calculated,

$$\sigma_{t_0}^t(\mathbf{x}_0) = \frac{1}{2|T|} \log(\lambda_n) \quad (2.8)$$

where  $T = t - t_0$  is the (signed) elapsed time, often called the integration time. Recent advances in dynamical systems theory have developed new Eulerian methods to analyze this system based on the Eulerian rate-of-strain tensors. The Eulerian rate-of-strain tensor is defined as

$$\mathbf{S}(\mathbf{x}, t) = \frac{1}{2} \left( \nabla \mathbf{v}(\mathbf{x}, t) + \nabla \mathbf{v}(\mathbf{x}, t)^T \right), \quad (2.9)$$

the eigenvalues of which are

$$s_1 < s_2 < \dots < s_n, \quad (2.10)$$

and are associated with the normalized eigenvectors

$$\boldsymbol{\xi}_{s_i} \quad i \in \{1, \dots, n\}. \quad (2.11)$$

From the eigenvalues of the Eulerian rate-of-strain tensor one can identify regions of the flow which are more attracting and repelling.

For two dimensional systems, [16] showed that the minimum eigenvalue,  $s_1$ , provides a measure of instantaneous hyperbolic attraction; with isolated minimas forming the cores of attracting OECS. Meanwhile, the maximum eigenvalue,  $s_2$ , was shown to provide a measure of instantaneous hyperbolic repulsion; with isolated maximas of forming the cores of repelling OECS. Furthermore, in [18]  $s_1$  was identified as the attraction rate and was used to look for indications of attracting LCSs. While  $s_2$  was identified as the repulsion rate. This nomenclature will be used in this manuscript as well, with  $s_n$  replacing  $s_2$ .

## 2.3 Expansion of the Cauchy-Green tensor in the infinitesimal integration time limit

### 2.3.1 Eigenvalues of $\mathbf{S}$ as FTLE limit as integration time goes to zero

For small  $|T|$ , we can perform a Taylor series expansion of  $\mathbf{C}_{t_0}^t(\mathbf{x})$  as

$$\mathbf{C}_{t_0}^t(\mathbf{x}) = \mathbb{1} + 2T\mathbf{S}(\mathbf{x}, t_0) + T^2\mathbf{B}(\mathbf{x}, t_0) + \frac{1}{2}T^3\mathbf{Q}(\mathbf{x}, t_0) + \mathcal{O}(T^4), \quad (2.12)$$

where  $\mathbb{1}$  is the  $n \times n$  identity and where

$$\mathbf{B}(\mathbf{x}, t_0) \equiv \frac{1}{2} \left[ \nabla \mathbf{a}(\mathbf{x}, t_0) + \left( \nabla \mathbf{a}(\mathbf{x}, t_0) \right)^T \right] + \nabla \mathbf{v}(\mathbf{x}, t_0)^T \cdot \nabla \mathbf{v}(\mathbf{x}, t_0), \quad (2.13)$$

where the acceleration field,  $\mathbf{a}(\mathbf{x}, t_0)$ , is

$$\mathbf{a}(\mathbf{x}, t_0) = \frac{d}{dt} \mathbf{v}(\mathbf{x}, t_0) = \frac{\partial}{\partial t} \mathbf{v}(\mathbf{x}, t_0) + \mathbf{v}(\mathbf{x}, t_0) \cdot \nabla \mathbf{v}(\mathbf{x}, t_0) \quad (2.14)$$

is the total time derivative of  $\mathbf{v}(\mathbf{x}, t_0)$ , that is, the acceleration measured along a trajectory (i.e., in a Lagrangian frame). The matrix  $\mathbf{Q}$  is given in the appendix.

We note the following general result for the eigenvalues,

$$\lambda^-(\mathbf{A}) = \lambda_1(\mathbf{A}) \leq \dots \leq \lambda_n(\mathbf{A}) = \lambda^+(\mathbf{A}), \quad (2.15)$$

of  $n \times n$  real symmetric matrices  $\mathbf{A}$  and scalar  $\varepsilon \neq 0$ . The formula is,

$$\lambda^\pm(\mathbb{1} + \varepsilon\mathbf{A}) = 1 + \lambda^\pm(\varepsilon\mathbf{A}) \quad (2.16)$$

where

$$\lambda^\pm(\varepsilon\mathbf{A}) = \begin{cases} \varepsilon\lambda^\pm(\mathbf{A}), & \text{for } \varepsilon > 0 \\ \varepsilon\lambda^\mp(\mathbf{A}), & \text{for } \varepsilon < 0 \end{cases} \quad (2.17)$$

See the appendix for the proof.

In (2.8),  $\lambda_n = \lambda^+(\mathbf{C}_{t_0}^t(\mathbf{x}))$ . For small  $T > 0$ , where we can neglect the  $\mathcal{O}(T^2)$  and higher terms, we have

$$\lambda^+(\mathbf{C}_{t_0}^t(\mathbf{x})) = 1 + 2T\lambda^+(\mathbf{S}(\mathbf{x}, t_0)) + \mathcal{O}(T^2) \quad (2.18)$$

Thus,

$$\log(\lambda_n) = \log(1 + 2T\lambda^+(\mathbf{S}(\mathbf{x}, t_0))) = 2T\lambda^+(\mathbf{S}(\mathbf{x}, t_0)) = 2Ts_n(\mathbf{x}, t_0) \quad (2.19)$$

in the limit of small  $T$  using the Taylor expansion  $\log(1 + \varepsilon) = \varepsilon + \mathcal{O}(\varepsilon^2)$ .

From (2.8), and noting that  $|T| = T$  for  $T > 0$ , we have,

$$\sigma_{t_0}^t(\mathbf{x}) = \frac{1}{2|T|} \log(\lambda_n) = \frac{1}{2T} 2Ts_n(\mathbf{x}, t_0) = s_n(\mathbf{x}, t_0) \quad (2.20)$$

Therefore, the maximum eigenvalue of  $\mathbf{S}(\mathbf{x}, t_0)$  is the limit of the FTLE value for forward time as  $T \rightarrow 0^+$ .

For  $T < 0$  with small  $T$ , we have

$$\lambda^+(\mathbf{C}_{t_0}^t(\mathbf{x})) = 1 + 2T\lambda^-(\mathbf{S}(\mathbf{x}, t_0)) + \mathcal{O}(T^2) \quad (2.21)$$

Thus,

$$\log(\lambda_n) = 2T\lambda^-(\mathbf{S}(\mathbf{x}, t_0)) = 2Ts_1(\mathbf{x}, t_0) \quad (2.22)$$

From (2.8), and noting that  $|T| = -T$  for  $T < 0$ , we have,

$$\sigma_{t_0}^t(\mathbf{x}) = \frac{1}{2|T|} \log(\lambda_n) = -\frac{1}{2T} 2Ts_1(\mathbf{x}, t_0) = -s_1(\mathbf{x}, t_0) \quad (2.23)$$

Therefore, the negative of the minimum eigenvalue of  $\mathbf{S}(\mathbf{x}, t_0)$  is the limit of the FTLE value for backward time as  $T \rightarrow 0^-$ .

If we denote  $s_1$  and  $s_n$  as  $s^-$  and  $s^+$ , respectively, we can summarize the above result as

$$\sigma_{t_0}^t(\mathbf{x}) = \pm s^\pm(\mathbf{x}, t_0) \quad \text{as } t - t_0 \rightarrow 0^\pm \quad (2.24)$$

For the  $n = 2$  dimensional case with  $\mathbf{x} = (x, y)$  with the vector field denoted  $\mathbf{v} = (u, v)$ , the velocity gradient tensor is given explicitly as,

$$\nabla \mathbf{v} = \begin{bmatrix} \frac{\partial u}{\partial x} & \frac{\partial u}{\partial y} \\ \frac{\partial v}{\partial x} & \frac{\partial v}{\partial y} \end{bmatrix}, \quad (2.25)$$

with the Eulerian rate-of-strain tensor,

$$\mathbf{S} = \begin{bmatrix} \frac{\partial u}{\partial x} & \frac{1}{2} \left( \frac{\partial u}{\partial y} + \frac{\partial v}{\partial x} \right) \\ \frac{1}{2} \left( \frac{\partial u}{\partial y} + \frac{\partial v}{\partial x} \right) & \frac{\partial v}{\partial y} \end{bmatrix}. \quad (2.26)$$

The instantaneous attraction and repulsion rate,  $s^-$  and  $s^+$ , respectively, are then given

analytically by

$$s^\pm(\mathbf{x}) = \frac{1}{2} \left( \frac{\partial u}{\partial x} + \frac{\partial v}{\partial y} \right) \pm \frac{1}{2} \sqrt{\left( \frac{\partial u}{\partial x} - \frac{\partial v}{\partial y} \right)^2 + \left( \frac{\partial u}{\partial y} + \frac{\partial v}{\partial x} \right)^2}. \quad (2.27)$$

If  $\mathbf{v}(\mathbf{x})$  represents a 2D fluid velocity, then the attraction and repulsion rates can be written as

$$s^\pm(\mathbf{x}) = \frac{1}{2} \operatorname{div}(\mathbf{v}(\mathbf{x})) \pm \frac{1}{2} s(\mathbf{x}). \quad (2.28)$$

in terms of fluid quantities, where  $\operatorname{div}(\mathbf{v}(\mathbf{x})) = \nabla \cdot \mathbf{v}(\mathbf{x}) = \frac{\partial u}{\partial x} + \frac{\partial v}{\partial y}$  is the divergence of the flow field,  $s_N(\mathbf{x}) = \frac{\partial u}{\partial x} - \frac{\partial v}{\partial y}$  is the normal component of strain,  $s_S(\mathbf{x}) = \frac{\partial u}{\partial y} + \frac{\partial v}{\partial x}$  is the shear component of strain, and  $s(\mathbf{x}) = \sqrt{s_N^2(\mathbf{x}) + s_S^2(\mathbf{x})}$  is the total strain. For an incompressible 2D flow, notice  $s^\pm(\mathbf{x}) = \pm \frac{1}{2} s(\mathbf{x})$  and thus,  $\sigma_{t_0}^t(\mathbf{x}) = \frac{1}{2} s(\mathbf{x})$  as  $t - t_0 \rightarrow 0$ , that is, attracting and repelling fields have the same structure in the infinitesimal integration time limit.

### 2.3.2 Approximating FTLE to second-order in integration time

If we consider now the third term, the order  $T^2$  term, of (2.12), then (2.18) becomes

$$\lambda^+(\mathbf{C}_{t_0}^t(\mathbf{x})) = 1 + 2T\lambda^+ \left( \mathbf{S}(\mathbf{x}, t_0) + \frac{1}{2} T \mathbf{B}(\mathbf{x}, t_0) \right) + \mathcal{O}(T^3) \quad (2.29)$$

Note that  $\mathbf{B}(\mathbf{x}, t_0)$ , like  $\mathbf{S}(\mathbf{x}, t_0)$ , is symmetric, i.e.,  $\mathbf{B}(\mathbf{x}, t_0)^T = \mathbf{B}(\mathbf{x}, t_0)$ . It can be shown via matrix perturbation techniques (see the appendix) that,

$$\lambda^+ \left( \mathbf{S}(\mathbf{x}, t_0) + \frac{1}{2} T \mathbf{B}(\mathbf{x}, t_0) \right) = s_n + \frac{1}{2} T \boldsymbol{\xi}_{s_n}^T \mathbf{B} \boldsymbol{\xi}_{s_n} + \mathcal{O}(T^2) \quad (2.30)$$

Using the Taylor expansion  $\log(1 + \varepsilon) = \varepsilon - \frac{1}{2}\varepsilon^2 + \frac{1}{3}\varepsilon^3 + \mathcal{O}(\varepsilon^4)$ , by a similar argument as before, for small  $T$ , we have,

$$\begin{aligned} \log(\lambda^+(\mathbf{C}_{t_0}^t(\mathbf{x}))) &= \log\left(1 + 2T\left[s_n + \frac{1}{2}T\boldsymbol{\xi}_{s_n}^T \mathbf{B}\boldsymbol{\xi}_{s_n} + \mathcal{O}(T^2)\right]\right) \\ &= 2T\left[s_n + \frac{1}{2}T\boldsymbol{\xi}_{s_n}^T \mathbf{B}\boldsymbol{\xi}_{s_n} + \mathcal{O}(T^2)\right] - \frac{1}{2}4T^2s_n^2 + \mathcal{O}(T^3) \\ &= 2T\left[s_n + T\left(-s_n^2 + \frac{1}{2}\boldsymbol{\xi}_{s_n}^T \mathbf{B}\boldsymbol{\xi}_{s_n}\right) + \mathcal{O}(T^2)\right] \end{aligned} \quad (2.31)$$

Therefore, for  $T > 0$  with small  $|T|$ , we have,

$$\sigma_{t_0}^t(\mathbf{x}) = s_n(\mathbf{x}, t_0) + T\left(-s_n(\mathbf{x}, t_0)^2 + \frac{1}{2}\boldsymbol{\xi}_{s_n}(\mathbf{x}, t_0)^T \mathbf{B}(\mathbf{x}, t_0)\boldsymbol{\xi}_{s_n}(\mathbf{x}, t_0)\right) + \mathcal{O}(T^2) \quad (2.32)$$

And similarly, for  $T < 0$  with small  $|T|$ , we have,

$$\sigma_{t_0}^t(\mathbf{x}) = -s_1(\mathbf{x}, t_0) - T\left(-s_1(\mathbf{x}, t_0)^2 + \frac{1}{2}\boldsymbol{\xi}_{s_1}(\mathbf{x}, t_0)^T \mathbf{B}(\mathbf{x}, t_0)\boldsymbol{\xi}_{s_1}(\mathbf{x}, t_0)\right) + \mathcal{O}(T^2) \quad (2.33)$$

If we include terms through second order in  $T$ , we get the following,

$$\begin{aligned} \sigma_{t_0}^t(\mathbf{x}) &= s_n + T\left(-s_n^2 + \frac{1}{2}\lambda_1\right) + T^2\left(\frac{4}{3}s_n^3 - s_n\lambda_1 + \frac{1}{4}\lambda_2\right) + \mathcal{O}(T^3) \text{ for } T > 0 \\ \sigma_{t_0}^t(\mathbf{x}) &= -s_1 - T\left(-s_1^2 + \frac{1}{2}\lambda_1\right) - T^2\left(\frac{4}{3}s_1^3 - s_1\lambda_1 + \frac{1}{4}\lambda_2\right) + \mathcal{O}(T^3) \text{ for } T < 0 \end{aligned} \quad (2.34)$$

where  $\lambda_1$  and  $\lambda_2$  are from (2.93) and (2.102), respectively, in the appendix, and the dependence on  $\mathbf{x}$  and  $t_0$  is understood.

### 2.3.3 Equality of the eigenvectors of $\mathbf{S}$ and $\mathbf{C}$ as integration time goes to zero

Let  $\mathbf{C}$  be the  $n \times n$  right Cauchy-Green strain tensor,  $\mathbf{S}$  the  $n \times n$  Eulerian rate-of-strain tensor,  $\lambda_i$  an ordered eigenvalue of  $\mathbf{C}$ ,  $s_i$  an ordered eigenvalue of  $\mathbf{S}$ , and  $\mathbb{1}$  the  $n \times n$  identity matrix. Let  $T > 0$  be small enough that the relationships in (2.12) and (2.18) hold and  $\mathcal{O}(T^2)$  terms are negligible. Assume that  $\boldsymbol{\xi}_i$  is the eigenvector of  $\mathbf{S}$  associated with  $s_i$ , then

$$\mathbf{S} \boldsymbol{\xi}_i = s_i \boldsymbol{\xi}_i, \quad (2.35)$$

$$2T\mathbf{S} \boldsymbol{\xi}_i + \boldsymbol{\xi}_i = 2T s_i \boldsymbol{\xi}_i + \boldsymbol{\xi}_i, \quad (2.36)$$

$$(2T\mathbf{S} + \mathbb{1}) \boldsymbol{\xi}_i = (2T s_i + 1) \boldsymbol{\xi}_i, \quad (2.37)$$

$$\mathbf{C} \boldsymbol{\xi}_i = \lambda_i \boldsymbol{\xi}_i, \quad (2.38)$$

where the dependence on  $\mathbf{x}$  and  $t_0$  is understood and we used the order- $T$  approximation for  $\mathbf{C}$ . Thus, if  $\boldsymbol{\xi}_i$  is an eigenvector of  $\mathbf{S}$ , then  $\boldsymbol{\xi}_i$  is an eigenvector of  $\mathbf{C}$ . Now, assuming that  $\boldsymbol{\xi}_i$  is the eigenvector of  $\mathbf{C}$  associated with  $\lambda_i$ , and working through (2.35-2.38) in reverse proves that if  $\boldsymbol{\xi}_i$  is an eigenvector of  $\mathbf{C}$ , then  $\boldsymbol{\xi}_i$  is an eigenvector of  $\mathbf{S}$  in the limit as  $T$  goes to 0. For  $T < 0$  an analogous argument holds using (2.21) in place of (2.18) and with the ordering of the eigenvalues opposed, i.e.  $\lambda_i \sim s_{n-i+1}$ ,  $i \in [1, n]$ .

Therefore, in the limit as  $|T|$  goes to 0, the eigenvectors of  $\mathbf{S}$  and  $\mathbf{C}$  are equal. For small  $|T|$ , we can also use the perturbation expansion of  $\mathbf{C}$ , to get the estimated eigenvectors of  $\mathbf{C}$  from (2.84) in Appendix A.3, which provides the eigenvectors through order  $T^2$  using only the velocity field  $\mathbf{v}$  evaluated at  $\mathbf{x}$  and time  $t_0$  as well as appropriate derivatives.

## 2.4 Infinitesimal-time LCS

Previous work [1, 2, 3, 4, 5, 6, 7, 10] has demonstrated that LCSs can be identified as Ridges of the FTLE field. While there are different mathematical definitions for what constitutes a ridge, a ridge-line can be thought of as the generalization of the concept of a local maxima. For this manuscript LCSs will be identified as C-ridges of the FTLE field. C-ridges were first described in [19], they are ridge-lines of the FTLE which are orthogonal to the direction of maximal stretching. Mathematically, they are defined as,

$$\sigma > 0, \tag{2.39}$$

$$\nabla\sigma \cdot \boldsymbol{\xi}_{\lambda_n} = 0, \tag{2.40}$$

$$(\mathbf{H}_\sigma \cdot \boldsymbol{\xi}_{\lambda_n}) \cdot \boldsymbol{\xi}_{\lambda_n} < 0. \tag{2.41}$$

C-ridges are advantageous over other definitions of ridges for the FTLE field, as they only rely on invariants of the Cauchy-Green strain tensor. C-ridges of the FTLE field have also been proven in [19] to be mathematically equivalent to the variational definition hyperbolic LCSs given in [13].

We propose an instantaneous approximation to the familiar LCS, called infinitesimal-time LCS (iLCS). Following [19] we seek material lines in the fluid flow which maximize local stretching and are orthogonal to the direction of maximal stretching. For a fluid flow the FTLE field provides a measure of stretching over a given time period. As  $-s_1$  and  $s_n$  are the limits of the backward-time and forward-time FTLE fields as integration time goes to 0, we seek ridge-lines of these field which are orthogonal to the direction of maximal stretching. The direction of maximal stretching in a fluid flow over a time period is the given by the eigenvector of the Cauchy-Green strain tensor associated with the largest eigenvalue. As in the infinitesimal-time limit, the eigenvectors of the Cauchy-Green and Eulerian tensors are

equal, we seek ridge-lines of  $-s_1$  and  $s_2$  which are orthogonal to their associated eigenvector. Following [19], we call these ridge-lines, S-ridges. S-ridges are the limit of C-ridges as integration time goes to 0. Because of this, S-ridges are mathematically equivalent to the variational definition of LCS as the integration time goes to 0.

Because an attracting iLCS is a ridge-line of  $-s_1$ , it can be defined as a trough-line of  $s_1$ . Mathematically, this can be expressed as,

$$s_1 < 0, \tag{2.42}$$

$$\nabla_{s_1} \cdot \boldsymbol{\xi}_{s_1} = 0, \tag{2.43}$$

$$(\mathbf{H}_{s_1} \cdot \boldsymbol{\xi}_{s_1}) \cdot \boldsymbol{\xi}_{s_1} > 0. \tag{2.44}$$

Additionally, as a ridge-line of  $s_n$ , a repelling iLCS can be mathematically expressed as,

$$s_n > 0, \tag{2.45}$$

$$\nabla_{s_n} \cdot \boldsymbol{\xi}_{s_n} = 0, \tag{2.46}$$

$$(\mathbf{H}_{s_n} \cdot \boldsymbol{\xi}_{s_n}) \cdot \boldsymbol{\xi}_{s_n} < 0. \tag{2.47}$$

It should be noted that iLCSs are not restricted to 2D flows, as other Eulerian diagnostics have been, but generalize to  $n$  dimensional systems. Section 2.5.3 examines iLCSs in a realistic 2D geophysical flow. Section 2.5.4 applies iLCSs to a time-dependent 3D double gyre flow. Finally section 2.5.5 explores the use of iLCSs in a full coupled 3D flow.

## 2.5 Examples

### 2.5.1 2D Nonlinear Saddle Flow

Consider the nonlinear saddle flow

$$\begin{aligned}\dot{x} &= x \\ \dot{y} &= -y - y^3\end{aligned}\tag{2.48}$$

These two uncoupled ODEs admit the explicit solutions,

$$\begin{aligned}x(t) &= x_0 e^t \\ y(t) &= \frac{y_0}{\sqrt{(1 + y_0^2)e^{2t} - y_0^2}}\end{aligned}\tag{2.49}$$

where the initial condition at time  $t_0 = 0$  is  $\mathbf{x}_0 = (x_0, y_0)$ . While the  $y$  solution goes to infinity in finite integration time, only times small enough to be below the singular limit are considered. The Cauchy-Green strain tensor for a small backward integration time  $T < 0$ , is

$$\mathbf{C}_0^T(\mathbf{x}_0) = \begin{bmatrix} e^{2T} & 0 \\ 0 & \frac{e^{4T}}{((1+y_0^2)e^{2T}-y_0^2)^3} \end{bmatrix},\tag{2.50}$$

which yields a backward time FTLE of

$$\sigma_0^T(\mathbf{x}_0) = -\frac{1}{2T} \log \left( \frac{e^{4T}}{((1 + y_0^2)e^{2T} - y_0^2)^3} \right)\tag{2.51}$$

Writing the log term as follows, using a Taylor series approximations for small  $|T|$ ,

$$\begin{aligned}
& \log(e^{4T}) - \log[(1 + y_0^2)e^{2T} - y_0^2]^3 \\
&= 4T - 3 \log[(1 + y_0^2)(1 + 2T + \frac{1}{2!}(2T)^2 + \frac{1}{3!}(2T)^3 + \mathcal{O}(T^4)) - y_0^2] \\
&= 4T - 3 \log[1 + (1 + y_0^2)2T + (1 + y_0^2)2T^2 + (1 + y_0^2)\frac{4}{3}T^3 + \mathcal{O}(T^4)] \\
&= 4T - 3[(1 + y_0^2)2T + (1 + y_0^2)2T^2 - \frac{1}{2}(1 + y_0^2)^2 4T^2 \\
&\quad + \frac{1}{3}(1 + y_0^2)^3(2T)^2 + \frac{4}{3}(1 + y_0^2)T^3 - \frac{1}{2}(1 + y_0^2)^2(2T)^3 + \mathcal{O}(T^4)] \\
&= 4T - (1 + y_0^2)6T + 6T^2 y_0^2(1 + y_0^2) - 4y_0^2(1 + y_0^2)(1 + 2y_0^2)T^3 + \mathcal{O}(T^4) \\
&= -2T[(1 + 3y_0^2) - 3y_0^2(1 + y_0^2)T + 2y_0^2(1 + y_0^2)(1 + 2y_0^2)T^2 + \mathcal{O}(T^3)]
\end{aligned} \tag{2.52}$$

So the FTLE is expanded in  $T$  as follows, obtained by dividing by  $-2T$ ,

$$\sigma_0^T(\mathbf{x}_0) = (1 + 3y_0^2) - 3y_0^2(1 + y_0^2)T + 2y_0^2(1 + y_0^2)(1 + 2y_0^2)T^2 + \mathcal{O}(T^3) \tag{2.53}$$

We would like to approximate the first, second, and third terms (the zeroth-order, first-order, and second-order in  $T$ , respectively) using the procedure outlined in a previous section. The gradient of the velocity is

$$\nabla_{\mathbf{v}}(\mathbf{x}_0) = \begin{bmatrix} 1 & 0 \\ 0 & -(1 + 3y_0^2) \end{bmatrix}, \tag{2.54}$$

which is also  $\mathbf{S}(\mathbf{x}_0)$ , since the gradient is diagonal. This has a minimum eigenvalue  $s_1 = -(1 + 3y_0^2)$ , the negative of which matches the first term of (2.53), as prescribed by (2.33). To calculate the second term of (2.53), the term first-order in  $T$ , we need to calculate the acceleration field and then  $\mathbf{B}(\mathbf{x}_0)$ . The acceleration field is, following (2.14),

$$\begin{aligned}
\ddot{x} &= \frac{d}{dt}\dot{x} = x, \\
\ddot{y} &= \frac{d}{dt}\dot{y} = y + 4y^3 + 3y^5.
\end{aligned} \tag{2.55}$$

Therefore (2.13) gives,

$$\begin{aligned} \mathbf{B}(\mathbf{x}_0) &= \begin{bmatrix} 1 & 0 \\ 0 & (1 + 12y_0^2 + 15y_0^4) \end{bmatrix} + \begin{bmatrix} 1 & 0 \\ 0 & (1 + 6y_0^2 + 9y_0^4) \end{bmatrix}, \\ &= \begin{bmatrix} 2 & 0 \\ 0 & (2 + 18y_0^2 + 24y_0^4) \end{bmatrix}. \end{aligned} \quad (2.56)$$

The normalized eigenvector of  $\mathbf{S}(\mathbf{x}_0)$  corresponding to  $s_1$  is simply  $\boldsymbol{\xi}_0 = [0, 1]^T$ , which yields,

$$\begin{aligned} \frac{1}{2}\lambda_1 &= \frac{1}{2}\boldsymbol{\xi}_0^T \mathbf{B}(\mathbf{x}_0) \boldsymbol{\xi}_0 = \frac{1}{2} \begin{bmatrix} 0 & 1 \end{bmatrix} \begin{bmatrix} 2 & 0 \\ 0 & (2 + 18y_0^2 + 24y_0^4) \end{bmatrix} \begin{bmatrix} 0 \\ 1 \end{bmatrix}, \\ &= \frac{1}{2}(2 + 18y_0^2 + 24y_0^4), \\ &= 1 + 9y_0^2 + 12y_0^4 \end{aligned} \quad (2.57)$$

hence,

$$\begin{aligned} -s_1^2 + \frac{1}{2}\boldsymbol{\xi}_0^T \mathbf{B}(\mathbf{x}_0) \boldsymbol{\xi}_0 &= -(1 + 6y_0^2 + 9y_0^4) + 1 + 9y_0^2 + 12y_0^4, \\ &= 3y_0^2 + 3y_0^4 \\ &= 3y_0^2(1 + y_0^2), \end{aligned} \quad (2.58)$$

the negative of which matches the  $T$  coefficient of the second term of (2.53), as prescribed by (2.33).

For the term second-order in  $T$ , we note that

$$\mathbf{Q}(\mathbf{x}_0) = \begin{bmatrix} \frac{8}{3} & 0 \\ 0 & -(\frac{8}{3} + 56y_0^2 + 192y_0^4 + 160y_0^6) \end{bmatrix}, \quad (2.59)$$

and since (2.98) implies that  $\xi_1$  is parallel to  $\xi_0$ , (2.102) yields,

$$\lambda_2 = \xi_0^T \mathbf{Q}(\mathbf{x}_0) \xi_0 = -\left(\frac{8}{3} + 56y_0^2 + 192y_0^4 + 160y_0^6\right) \quad (2.60)$$

According to (2.34), the second-order term is

$$\begin{aligned} & -T^2\left[\frac{4}{3}s_1^3 - s_1\lambda_1 + \frac{1}{4}\lambda_2\right] \\ & = -T^2\left[\left(-\frac{4}{3} + 2 - \frac{2}{3}\right) + (-12 + 24 - 14)y_0^2 \right. \\ & \quad \left. + (-36 + 78 - 48)y_0^4 + (-36 + 72 - 40)y_0^6\right] \\ & = -T^2[0 - 2y_0^2 - 6y_0^4 - 4y_0^6] \\ & = 2y_0^2(1 + y_0^2)(1 + 2y_0^2)T^2 \end{aligned} \quad (2.61)$$

which matches the  $T^2$  term of the true FTLE field, (2.53).

We have thus verified on this example the formulas of Sections 2.3.1 and 2.3.2 for approximating the true FTLE, (2.53), of the nonlinear saddle, (2.48), through second-order in the integration time  $T$ .

To illustrate the successive approximations, we show in Fig. 2.1 the root mean-squared error (RMSE) for the FTLE field as a function of integration time magnitude,  $|T|$ , over the domain  $U = \{(x_0, y_0) \in \mathbb{R}^2 \mid |y_0| < \frac{1}{2}\}$ . Notice that, as expected, the error grows linear in  $|T|$ , quadratic in  $|T|$ , and cubic in  $|T|$ , for the zeroth-order, first-order, and second-order approximations, respectively.

## 2.5.2 2D Time-Varying Double-Gyre Flow

While the time-varying double-gyre does not admit an explicit solution, as the previous example does, we can still analytically approximate the FTLE field up to first-order in  $T$

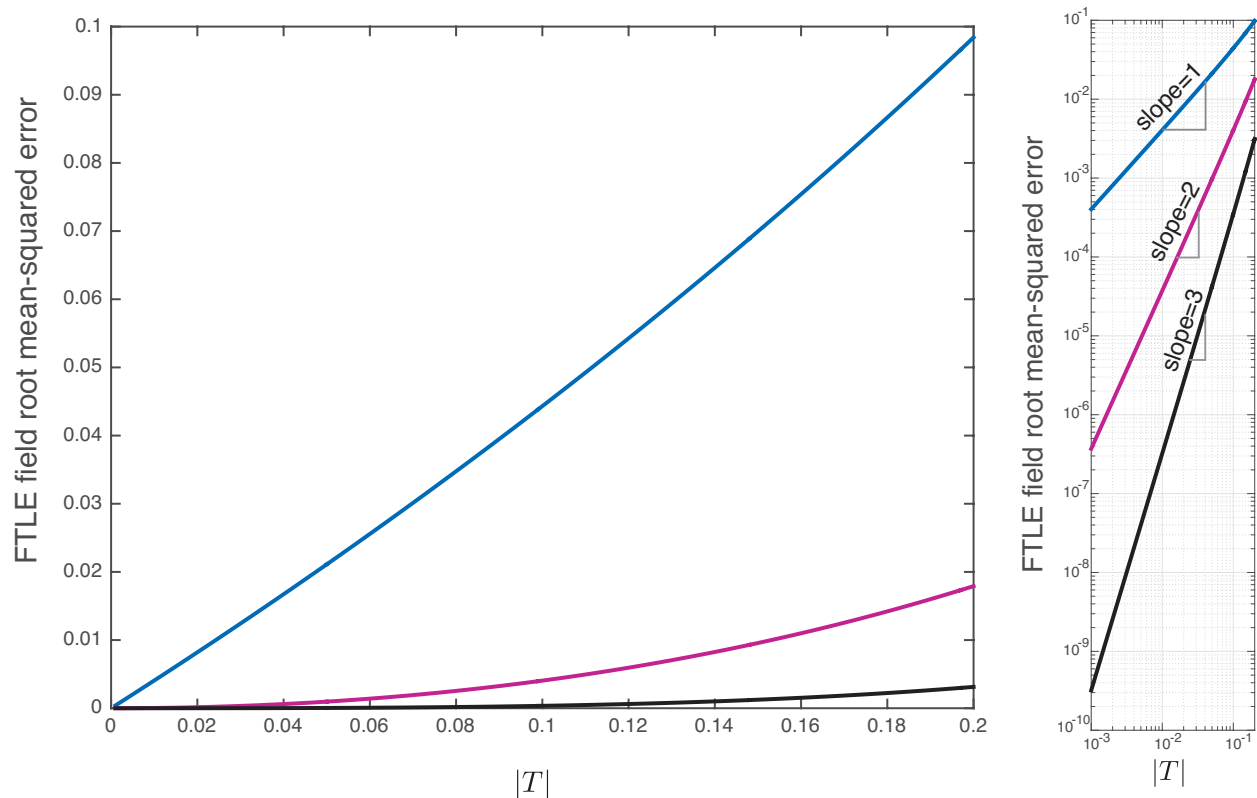


Figure 2.1: RMSE for successive approximations of the backward-time FTLE field for the nonlinear saddle (2.48) expanded in  $T$ : zeroth-order (blue), first-order (magenta), second-order (black). Notice that the error grows linear in  $|T|$ , quadratic in  $|T|$ , and cubic in  $|T|$ , respectively, as shown more clearly in the log-log plot on the right.

using the formulas of Section 2.3.2.

We look at the double-gyre flow as described in [1]. This flow comes from the Hamiltonian stream function,

$$\psi(x, y, t) = A \sin(\pi f(x, t)) \sin(\pi y), \quad (2.62)$$

where

$$f(x, t) = \epsilon \sin(\omega t)x^2 + (1 - 2\epsilon \sin(\omega t))x. \quad (2.63)$$

We can then calculate the velocity field,  $\mathbf{v} = (u, v)$  as,

$$\begin{aligned} \dot{x} = u(x, y, t) &= -\frac{\partial\psi}{\partial y} = -A\pi \sin(\pi f(x, t)) \cos(\pi y), \\ \dot{y} = v(x, y, t) &= \frac{\partial\psi}{\partial x} = A\pi \cos(\pi f(x, t)) \sin(\pi y) \frac{\partial f}{\partial x}(x, t). \end{aligned} \quad (2.64)$$

Following [1], we use parameters  $A = 0.1$ ,  $\omega = 0.2\pi$ , and  $\epsilon = 0.25$ . The gradient tensor is

$$\begin{aligned} \nabla_{\mathbf{v}} &= \begin{bmatrix} \frac{\partial u}{\partial x} & \frac{\partial u}{\partial y} \\ \frac{\partial v}{\partial x} & \frac{\partial v}{\partial y} \end{bmatrix} \\ &= \begin{bmatrix} -\pi^2 A \cos(\pi f) \cos(\pi y) \frac{\partial f}{\partial x} & \pi^2 A \sin(\pi f) \sin(\pi y) \\ -\pi^2 A \sin(\pi f) \sin(\pi y) \frac{\partial f}{\partial x} + \pi A \cos(\pi f) \sin(\pi y) \frac{\partial^2 f}{\partial x^2} & \pi^2 A \cos(\pi f) \cos(\pi y) \frac{\partial f}{\partial x} \end{bmatrix}. \end{aligned} \quad (2.65)$$

From this gradient, it can be analytically calculated via (2.27) that the zeroth order approximation to the backward-time FTLE for an initial condition  $\mathbf{x}_0 = (x_0, y_0)$  at initial time  $t_0$  in the infinitesimal integration time limit is,

$$\begin{aligned} s_1 &= -\frac{1}{2}\pi^2 A \left[ \left( \sin(\pi f) \sin(\pi y_0) \left( 1 - \frac{\partial f}{\partial x} \right) + \frac{1}{\pi} \cos(\pi f) \sin(\pi y_0) \frac{\partial^2 f}{\partial x^2} \right)^2 \right. \\ &\quad \left. + 4 \left( \cos(\pi f) \cos(\pi y_0) \frac{\partial f}{\partial x} \right)^2 \right]^{1/2}. \end{aligned} \quad (2.66)$$

where the dependence of  $s_1$  and  $f$  on  $(\mathbf{x}_0, t_0)$  is understood. We can also write this as,

$$\begin{aligned} s_1 &= -\pi^2 A \left[ \epsilon^2 \sin^2(\omega t) \left\{ \sin^2(\pi y_0) \left( \sin^2(\pi f)(1-x)^2 + \frac{1}{\pi} \sin(2\pi f)(1-x) \right. \right. \right. \\ &\quad \left. \left. + \frac{1}{\pi^2} \cos^2(\pi f) \right) + \cos^2(\pi y_0) \cos^2(\pi f)(1-x)^2 \right\} \\ &\quad \left. + \cos^2(\pi y_0) \cos^2(\pi f) \left( 1 - 4\epsilon \sin(\omega t)(1-x) \right) \right]^{1/2}. \end{aligned} \quad (2.67)$$

Note that the  $s_1$  field, just like the vector field, is a periodic function of  $t_0$  with period  $2\pi/\omega$ .

For  $t_0 = k2\pi/\omega$ , for  $k$  an integer, we have  $s_1(x_0, y_0, t_0) = -\pi^2 A |\cos(\pi x_0) \cos(\pi y_0)|$ .

The leading order term in the backward integration time  $T < 0$  can also be analytically determined. See the appendix for details.

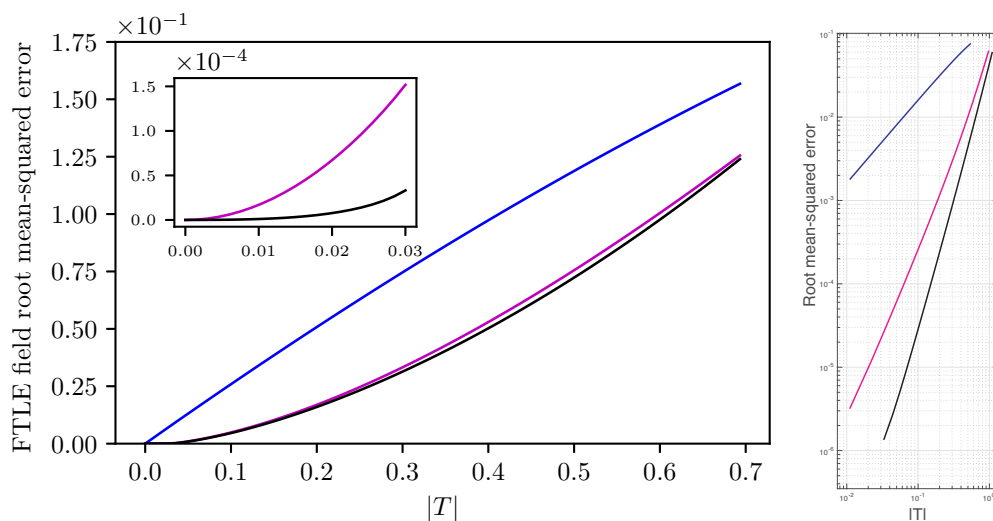


Figure 2.2: Left: RMSE vs.  $|T|$  for successive approximations of the backward-time FTLE field for the double-gyre expanded in  $T$ : zeroth-order (blue), first-order (magenta), second-order (black), showing the error grow linear, quadratic, and cubic in  $|T|$ , respectively. Right: Shows this RMSE vs.  $|T|$  in a log-log plot.

Figure 2.2 shows the RMSE between the backward-time FTLE field and the zeroth order (blue), first order (magenta), and second order (black) approximations. In this figure one can see that as the integration time,  $|T|$ , goes to 0 the approximations converge to the true FTLE field, as is expected. Figure 2.3 builds on this by showing a comparison of the FTLE field for a short integration time,  $T = -0.3$  (center), with an approximation to first order in  $T$  (left).

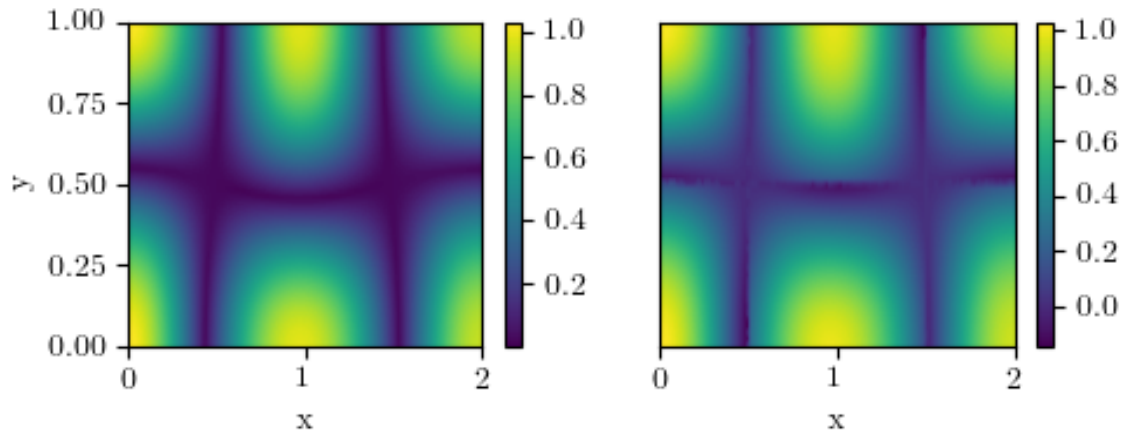


Figure 2.3: Left: FTLE field for the double-gyre flow for an integration period of  $T = -0.3$ . Right: approximation to the FTLE field to first-order in  $T$ . Parameters:  $A = 0.1$ ,  $\omega = 0.2\pi$ ,  $\epsilon = 0.25$ , and  $t_0 = 0$ .

### 2.5.3 2D Geophysical Flow Example

In this section the methods described above are applied to a realistic geophysical flow example, using wind data from a Weather Research and Forecasting (WRF) model simulation over the southeastern United States [20]. This model was run with a horizontal grid resolution of  $12 \text{ km} \times 12 \text{ km}$  and temporal resolution of 1 hr. Due to the scale mismatch between the horizontal resolution and the vertical resolution,  $\sim 0.05 - 1 \text{ km}$ , 1 vertical level was chosen to focus on for the analysis. The level that was chosen was  $\sim 100 \text{ m}$  above ground level, similar to what was done in [5, 7]. The simulation was performed for a 24 hr period beginning at 0000 GMT on July 1<sup>st</sup> 2011.

Using this data set the relationship between the attraction rate, higher order instantaneous approximations, and the backward-time FTLE field for a 2D geophysical fluid flow can be numerically verified. This can be seen in figure 2.4, which shows the RMSE of these approximations with the FTLE field as we integrate backward in time from 0000 GMT on July 2<sup>nd</sup> 2011. The blue line shows the RMSE for the attraction rate, the magenta for the attraction rate with a first order correction term, and the black for the attraction rate with

a second order correction. As  $|T|$  goes to 0, the RMSE of all 3 approximations also goes to 0. Thus numerically verifying the relationship shown in section 2.3.1 for a 2D geophysical flow. This figure also shows that for small  $|T|$  the second order approximation is the most accurate, as expected. However, for larger  $|T|$  the attraction rate will provide the most accurate approximation, which is to be expected of a Taylor series.

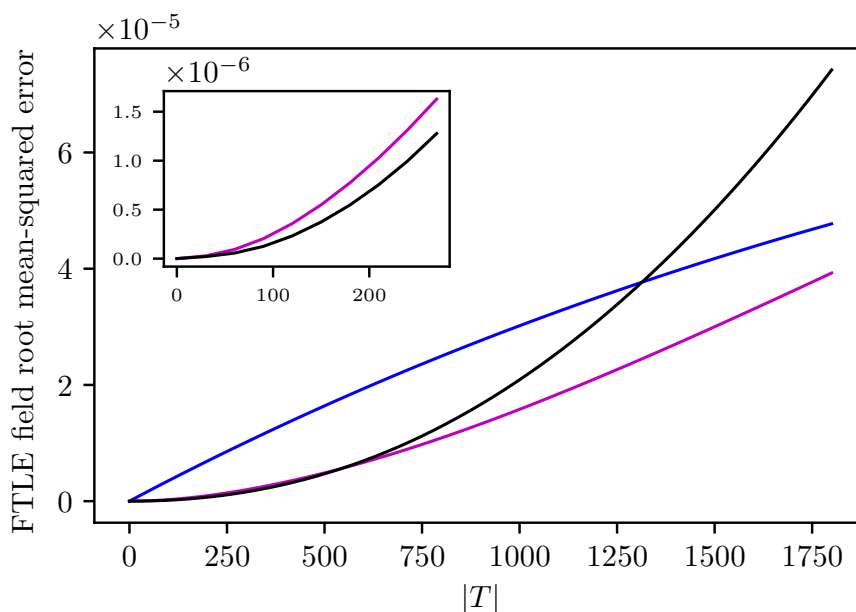


Figure 2.4: RMSE for successive approximations of the backward-time FTLE field for an atmospheric flow expanded in  $T$ : zeroth-order (blue), first-order (magenta), and second-order (black). Time is in seconds.

Figure 2.5 visually explores this connection between the attraction rate and the FTLE field. In Panel A we show the attraction rate field at 0000 GMT on July 2<sup>st</sup> 2011. Panels B, C, and D show the FTLE field after 1, 2, and 4 hours of backward-time integration. In these plots it can be seen that the important Lagrangian transport structures over the period examined are already present in the attracting rate field. As the field is integrated backward in time the transport structures become sharper and grow longer, but do not change significantly. For this particular flow, as the integration time is increased the transport patterns which are shown by the attracting rate field become more sharply defined. This relationship can

be quantified by the Pearson correlation coefficient, which is shown in figure 2.6. This figure shows that for short integration times, there is a strong correlation,  $> 0.6$ , between the attraction rate and backward-time FTLE field. Then, as the integration time is increased the correlation between the fields becomes weaker.

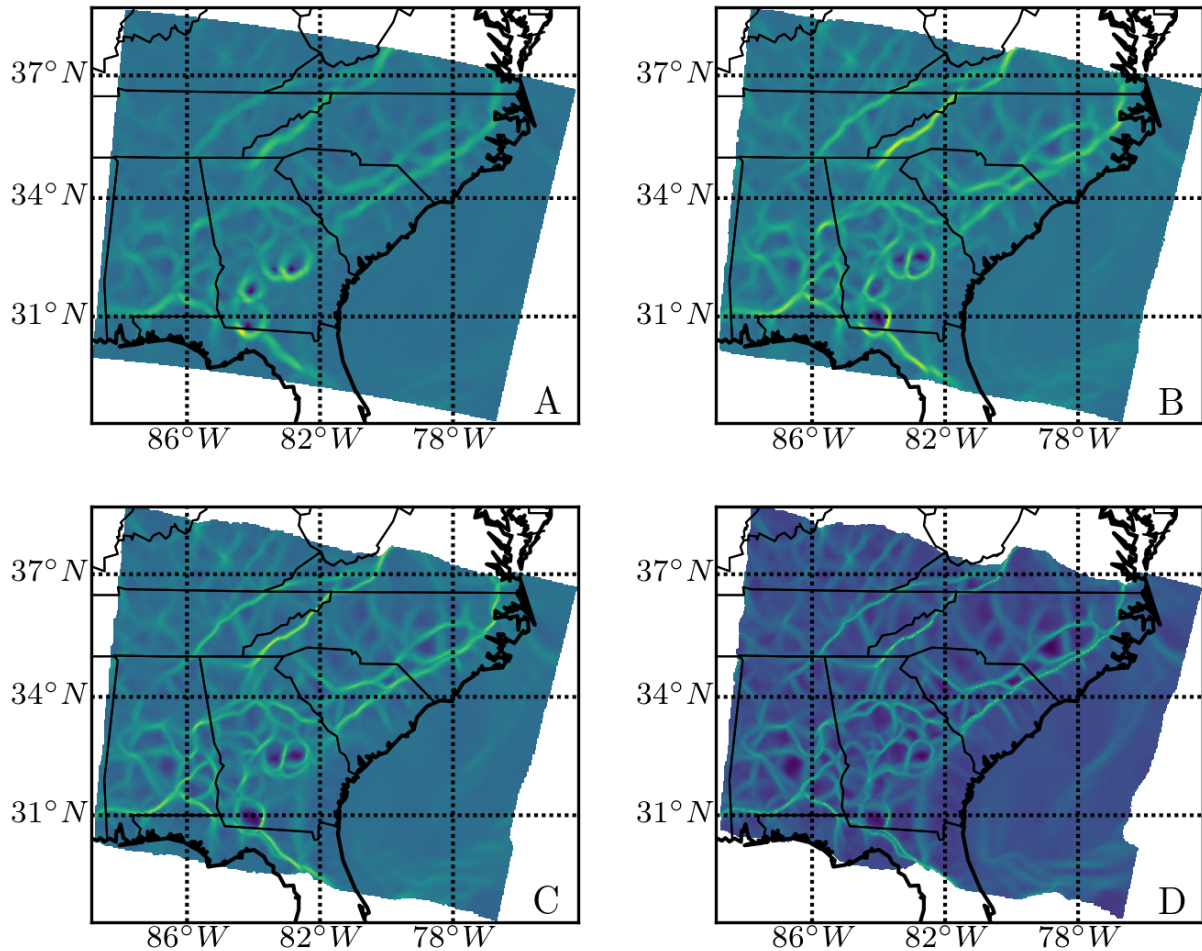


Figure 2.5: Comparison of the attraction rate (A), with FTLE fields of integration times  $T =$  (B)  $-1$  hr (C)  $-2$  hr, (D)  $-4$  hr. The spatial correlation between these fields can be seen in figure 2.6

Furthermore, this data set is able to verify that iLCSs are effective at predicting the Lagrangian behavior of passive tracer particles advected in a 2D geophysical flow. Figure 2.7 shows the evolution of attracting iLCSs (blue), repelling (red) iLCSs, and passive tracers

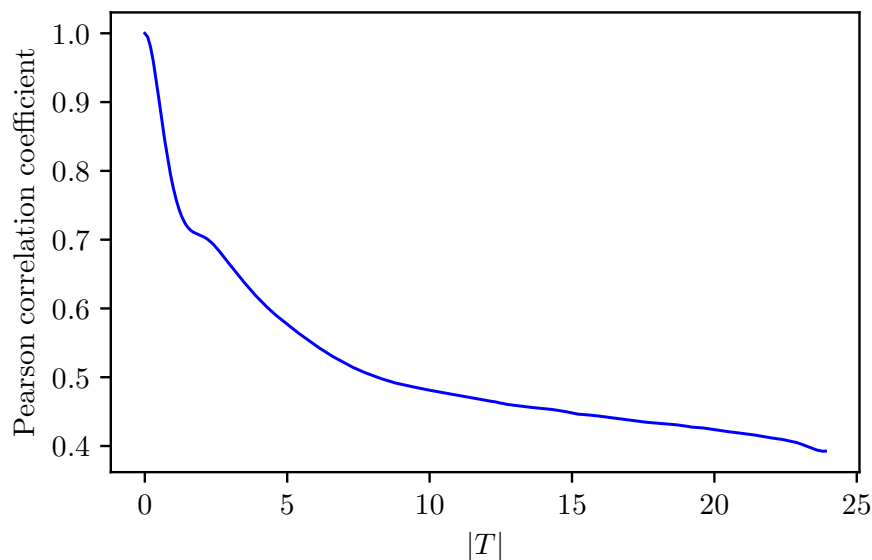


Figure 2.6: Pearson correlation coefficient between the attraction rate and the backward-time FTLE for different integration times,  $|T|$ .

(cyan). These structures were initialized at 0000 GMT on July 1<sup>st</sup> 2011 and advected forward in time. In panel A we show the iLCSs and tracers at the initial time. Panels B, C, and D show the iLCSs and tracers after 2, 4, and 8 hours, respectively. An animation of the evolution of the iLCSs and tracers over the entire 24 hr period can be found at <https://www.youtube.com/watch?v=h4UhJT8vsiU>. In these panels we can see that as time moves forward passive tracers are repelled away from the repelling iLCSs and attracted towards the attracting iLCSs, as we would expect. Interestingly, we can also see that some of the repelling iLCSs are attracted onto and effectively consumed by the attracting iLCSs. The explanation for this can be found in figure 2.8, where we show a comparison between the attracting rate and the repelling rate fields. In this figure we can see that the attracting rate field is stronger than the repelling rate field is, the most attractive points of the attracting rate field are more than twice as strong as the most repelling points in the repelling rate field. Thus it can be concluded that while the repelling iLCSs are repulsive, the attracting iLCSs are more attractive and thus overpower the repelling iLCSs after a sufficient period

of time.

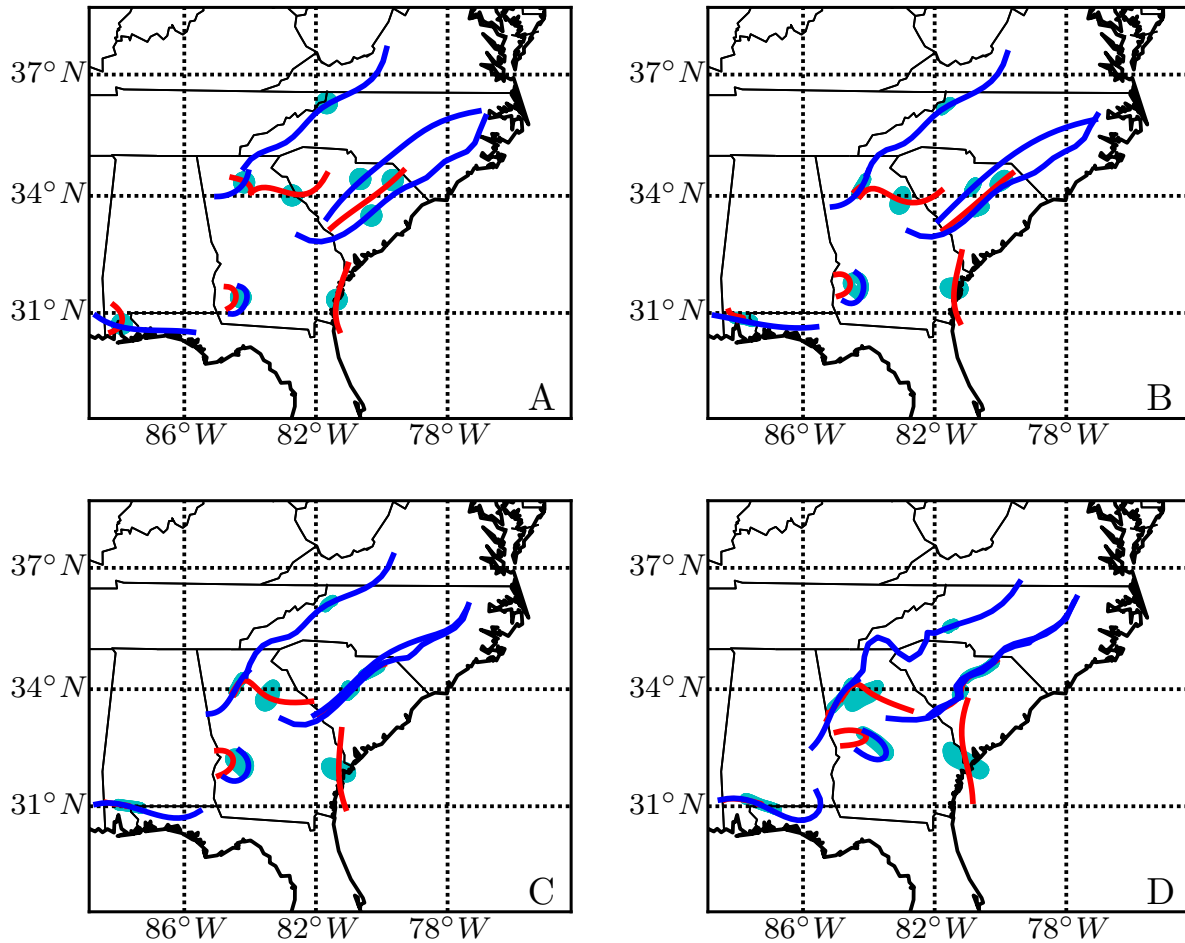


Figure 2.7: iLCSs and passive tracers at different integration times,  $T$ . A)  $T = 0$  hr, B)  $T = 2$  hr, C)  $T = 4$  hr, D)  $T = 8$  hr. Repelling iLCSs are shown in red, attraction iLCSs in blue, and passive tracers in cyan.

### 2.5.4 3D Time-varying Double Gyre Flow

In this section iLCSs are applied to a time-dependent three dimensional flow and the convergence of the attraction rate and higher order approximation to the backward-time FTLE field is further demonstrated. For this section the time-dependent double-gyre from section

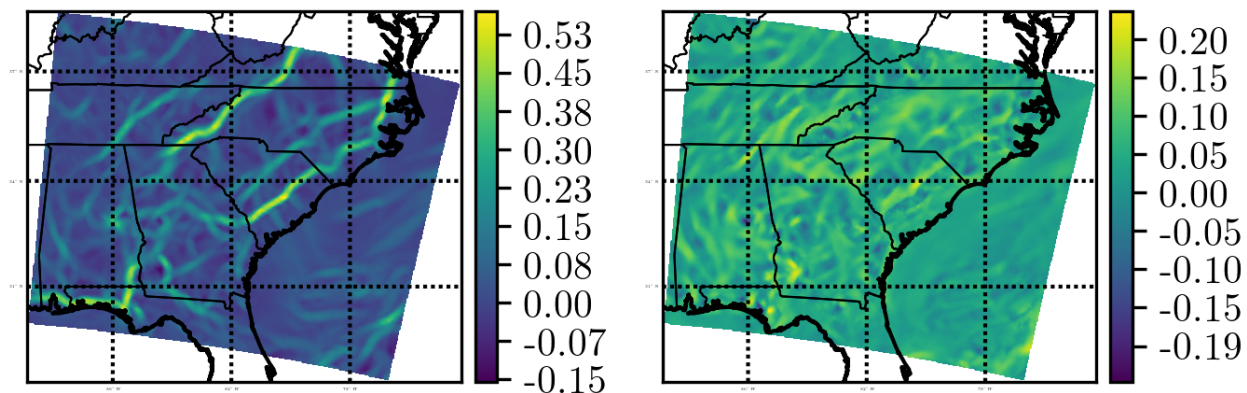


Figure 2.8: Comparison of the attraction rate field,  $s_1$ , left, and the repulsion rate field,  $s_2$ , right, at  $T = 0$ . Structures in the attraction rate field are noticeably stronger than in the repulsion rate field. The attraction rate field has been multiplied by  $-1$  to aid in visualization. Colorbar has units of  $\text{hr}^{-1}$ .

2.5.2 was extended to 3D. The new 3D equations are,

$$\dot{x} = -A\pi \sin(\pi f(x, t)) \cos(\pi y), \quad (2.68)$$

$$\dot{y} = A\pi \cos(\pi f(x, t)) \sin(\pi y) \frac{\partial f}{\partial x}(x, t), \quad (2.69)$$

$$\dot{z} = 0. \quad (2.70)$$

While this flow is still largely 2-dimensional (i.e. there is no motion in the vertical direction), it does serve as a proof of concept that iLCSs work for 3-dimensional systems.

Figure 2.12 shows the RMSE of Eulerian approximations with the FTLE field as the flow is integrated backward in time from  $t_0$ . For the sake of simplicity  $t_0 = 0$  was chosen. The RMSE for the attraction rate is shown in blue and the attraction rate with a first order correction in magenta. It can be seen that as the integration time goes to 0, the RMSE goes to 0 as well, as expected.

iLCSs for the 3D double gyre flow are shown in figures 2.10 and 2.11. Figure 2.10 shows an attracting iLCS (blue), along with a blob of passive tracers (green). Meanwhile, figure 2.11

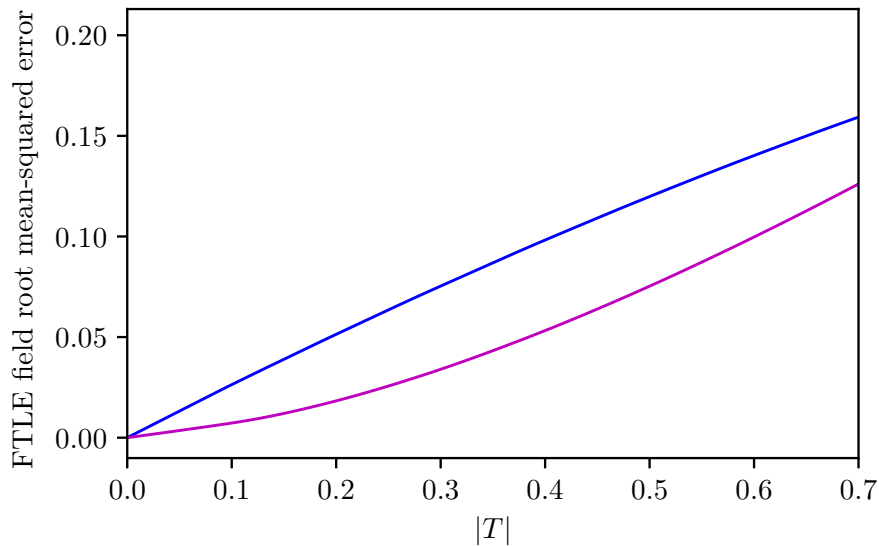


Figure 2.9: RMSE for successive approximations of the backward-time FTLE field for the 3D double-gyre flow (2.70) expanded in  $T$ : zeroth-order (blue), first-order (magenta). Time is in non-dimensional units.

show a repelling iLCS (red), along with blob of tracers (green). In both figures, the first row shows the the initial configuration from 2 different angles, while the second row shows the configuration after being advected by the flow for a time of 1.25, non-dimensional time. In figure 2.10, one can see that the green blob, starting out as a sphere around a portion of the iLCS, becomes squeezed towards and spread along the iLCS as the two are advected by the flow. In figure 2.11, the green blob, starting as a sphere, spreads out and away from the repelling iLCS as they are advected by the flow. These behaviors demonstrate that iLCSs are indeed the instantaneous approximation of traditional LCSs in 3D. Animations of these figures can be found online. The animation for the attracting iLCS can be found at [https://youtu.be/NWxdG7BY0\\_o](https://youtu.be/NWxdG7BY0_o), and the repelling iLCS at <https://youtu.be/ZkD3qBnrHL0>.

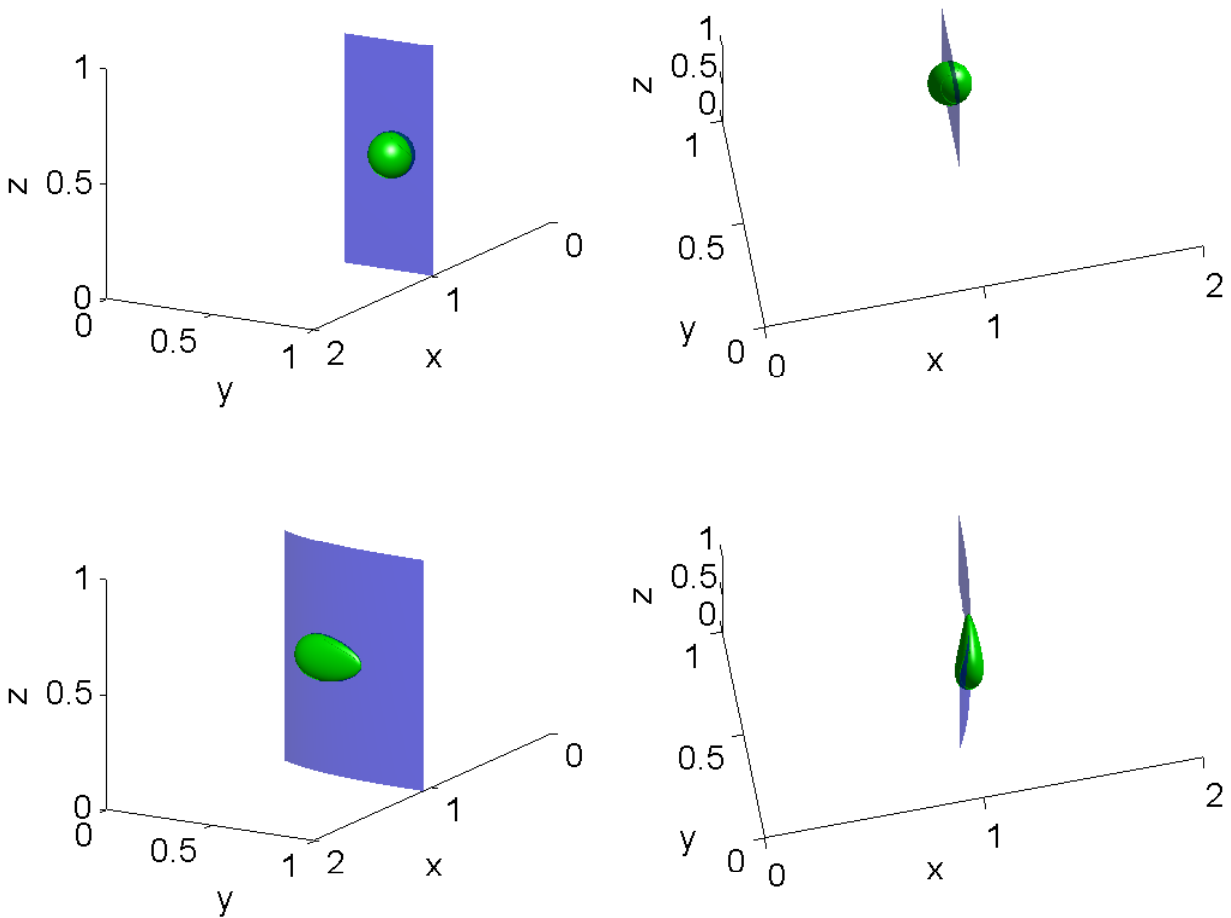


Figure 2.10: An attracting 3D iLCS, blue, with a blob of passive tracers, green, shown at different angles. Top row shows the iLCS and tracers at the initial time,  $t=0$ . Bottom row shows the iLCS and tracers after being advected forward in time 1.25.

### 2.5.5 3D ABC Flow

In this section iLCSs are applied to a fully coupled 3-dimensional flow, additionally the convergence of the attraction rate and higher order approximation to the backward-time FTLE field is further demonstrated. For this section the ArnoldBeltramiChildress (ABC)

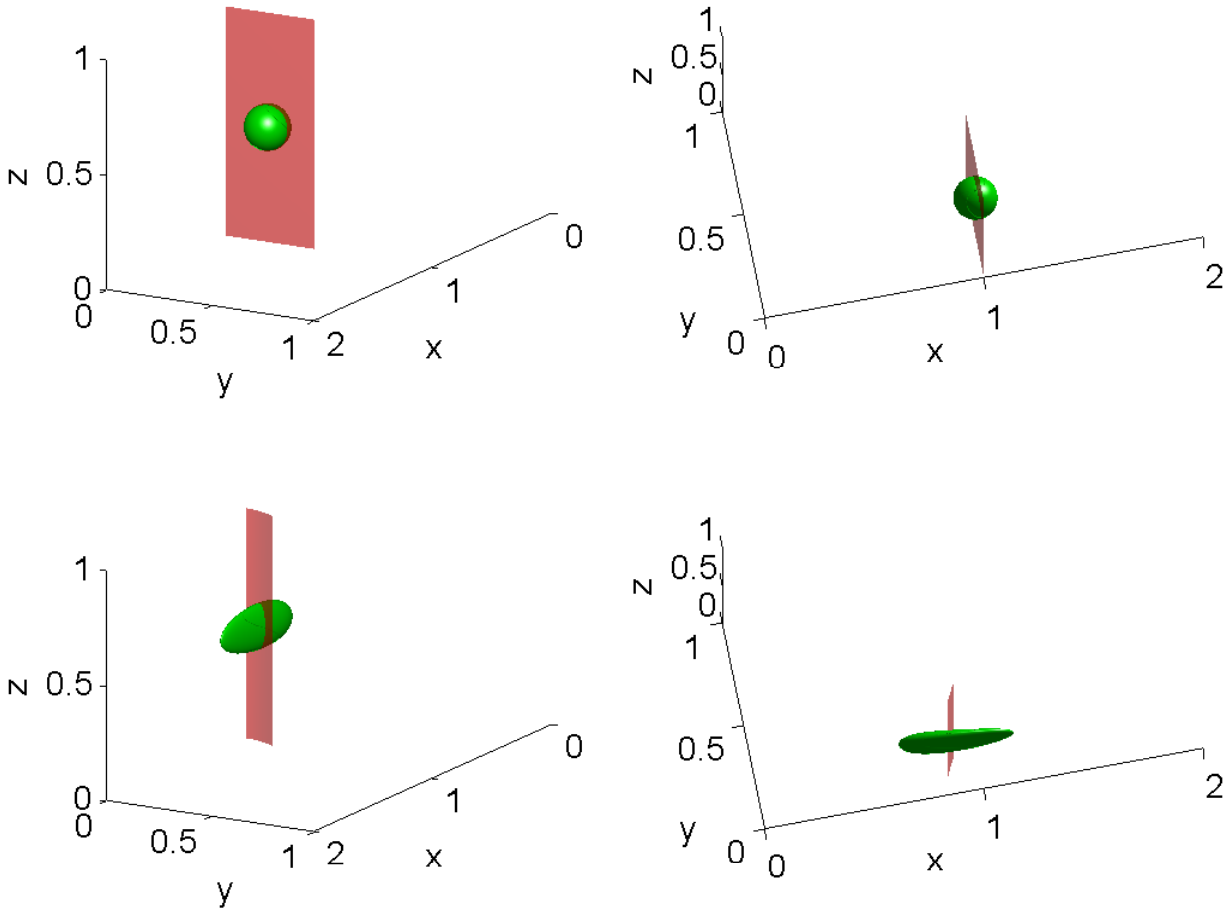


Figure 2.11: A repelling 3D iLCS, red, with a blob a passive tracers, green, shown at different angles. Top row shows the iLCS and tracers at the initial time,  $t=0$ . Bottom row shows the iLCS and tracers after being advected forward in time 1.25.

flow [21, 22] was chosen. The equations of the ABC flow are,

$$\begin{aligned}
 u &= A \sin(z) + C \cos(y), \\
 v &= B \sin(x) + A \cos(z), \\
 w &= C \sin(y) + B \cos(x).
 \end{aligned}
 \tag{2.71}$$

The ABC flow is an exact solution to Euler's fluid equations and has been shown to have chaotic trajectories [22]. The domain for  $(x, y, z)$  is the periodic cube  $U = [0, 2\pi]^3$ . For coefficients we choose  $A = \sqrt{3}$ ,  $B = \sqrt{2}$ ,  $C = 1$ , as was done in [23].

As the ABC flow is an analytical flow, we can also analytically express the repulsion and attraction rate fields, respectively, as,

$$\begin{aligned} s_3 &= 2\rho^{1/3} \cos\left(\frac{\theta}{3}\right) > 0, \\ s_1 &= -\frac{1}{2}s_3 - \sqrt{3}\rho^{1/3} \sin\left(\frac{\theta}{3}\right) < 0, \end{aligned} \tag{2.72}$$

where the dependence on position  $\mathbf{x} = (x, y, z)$  is understood and  $\rho$  and  $\theta$  are given by,

$$\begin{aligned} \rho &= \sqrt{q^2 + |p|}, \\ \theta &= \tan^{-1}\left(\frac{\text{Im}(\sqrt{p})}{q}\right), \end{aligned} \tag{2.73}$$

where

$$\begin{aligned} q &= -\frac{1}{2}a_0, \\ p &= \frac{1}{27}a_1^3 + \frac{1}{4}a_0^2, \\ a_0 &= -\frac{1}{4}(B \cos(x) - C \sin(y))(C \cos(y) - A \sin(z))(-B \sin(x) + A \cos(z)), \\ a_1 &= -\frac{1}{4}\left[(B \cos(x) - C \sin(y))^2 + (C \cos(y) - A \sin(z))^2 + (-B \sin(x) + A \cos(z))^2\right] \end{aligned} \tag{2.74}$$

where the coefficients  $a_1$  and  $a_0$  come from the characteristic polynomial for  $\mathbf{S}$  for this system,

$$s^3 + a_1s + a_0 = 0. \tag{2.75}$$

Figure 2.12 shows the RMSE of Eulerian approximations with the FTLE field as the flow

is integrated backward in time from  $t_0$ . Since this flow is autonomous,  $t_0$  is arbitrary. The RMSE for the attraction rate is shown in blue and the attraction rate with a first order correction in magenta. As in the previous sections, this figure shows that as the integration time goes to 0, the RMSE goes to 0 as well.

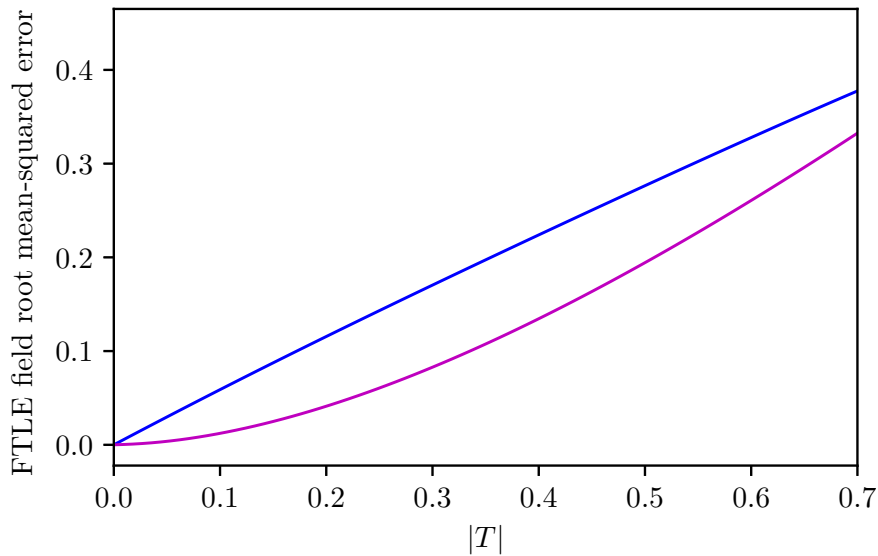


Figure 2.12: RMSE for successive approximations of the backward-time FTLE field for the ABC flow (2.71) expanded in  $T$ : zeroth-order (blue), first-order (magenta). Time is in non-dimensional units.

Figures 2.13 and 2.14 examine the efficacy of iLCSs for the ABC flow. As in the previous section, figure 2.13 shows an attracting iLCS (blue), along with a blob of passive tracers (green); while, figure 2.14 show a repelling iLCS (red), along with 2 blobs of passive tracers (green). In both figures, the first row shows the the initial configuration from 2 different angles, while the second row shows the configuration after being advected by the flow for a time of 1.309, non-dimensional time. In figure 2.13, one can see that the green blob, starting out as a sphere around a portion of the iLCS, becomes squeezed towards and spread along the iLCS as the two are advected by the flow. Due to the the large amounts of twisting and shear in the ABC flow, the repelling effects of iLCS are more difficult to visualize in this flow than in sections 2.5.3 and 2.5.4. To compensate for this, 2 blobs were used in figure 2.14.

The green blobs are initialized above and below a repelling iLCS. In this figure one can see that as the iLCS and tracers are advected by the flow, the tracer blobs are transported away from each other. This also demonstrates the effectiveness of iLCSs as an indicator of flow separatrices, as tracers on opposite sides of the iLCS do not interact with one another. An animation of the the attracting iLCS and tracer blob in figure 2.13 can be found online at <https://youtu.be/fmXFcpUEfaI>.

## 2.6 Conclusion

This manuscript has formulated a rigorous mathematical connection between the attraction rate and the backward-time FTLE, as well as the repulsion rate and the forward-time FTLE. These mathematical connections prove that the attraction and repulsion rates are the limits of the FTLE as integration time goes to 0. Additionally this manuscript has show that for small integration times  $|T| \ll 1$  the eigenvectors of the right Cauchy-Green strain tensor are equal to those of the Eulerian rate-of-strain tensor. These proofs laid the groundwork for a new Eulerian diagnostic, which was herein formulated, iLCS, the infinitesimal-time limit of Lagrangian coherent structures. In addition to this, higher order approximations of the FTLE field using Rivlin-Ericksen tensors were derived and explored. These resulted in findings that higher order FTLE approximations are more accurate for short integration periods, consistent with what would be expected from a Taylor series expansion.

This work provides a significant contribution to the field of dynamical systems analysis and has important applications for the study unsteady fluid flows. For example, iLCSs can be used to in the place of LCSs when studying geophysical flows. This manuscript showed that iLCSs are valid predictors of atmospheric transport for up to several hours; they would likely be valid even longer in oceanic flows. The use of iLCSs could thus provide an accurate

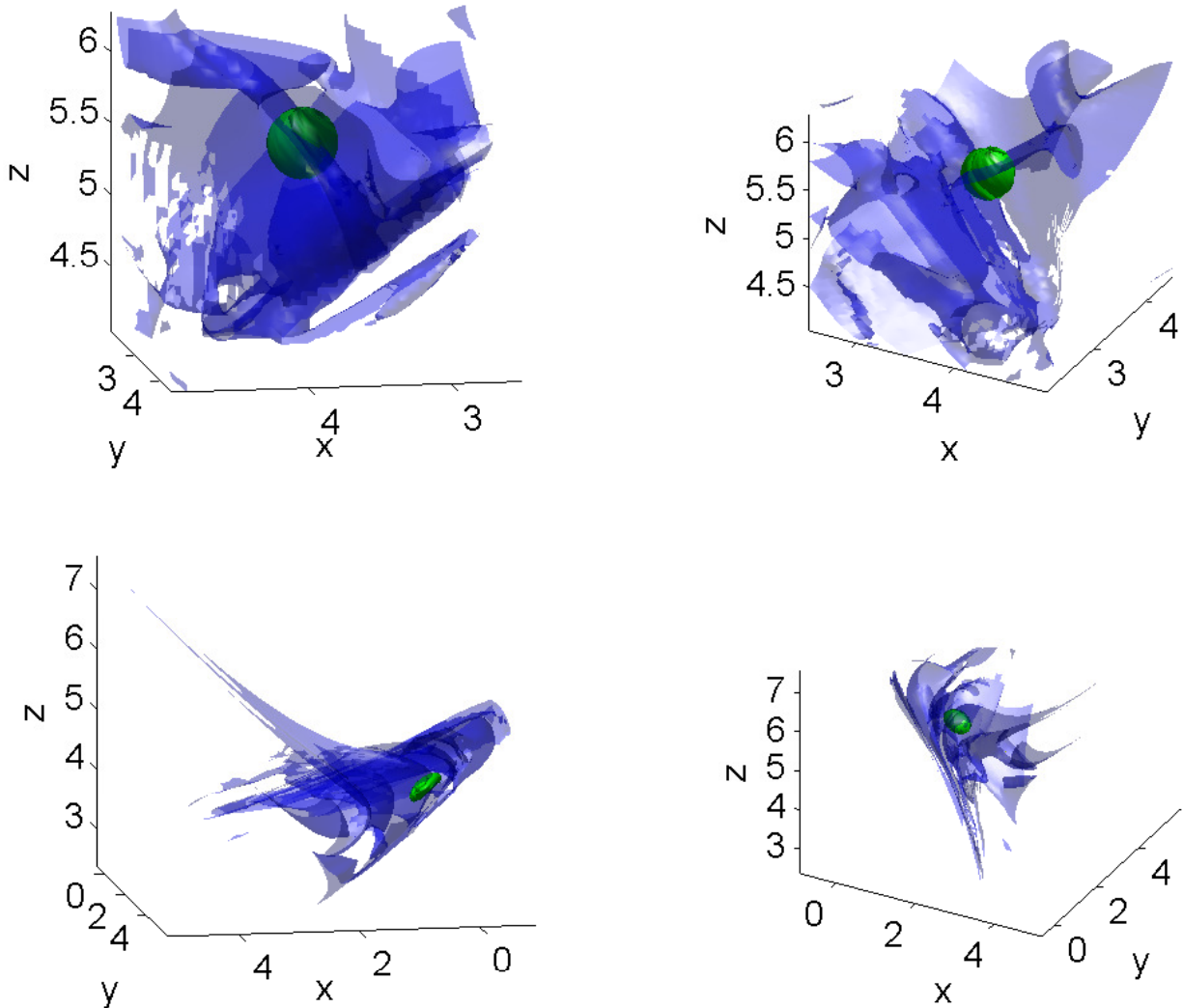


Figure 2.13: An attracting 3D iLCS, blue, with a blob of passive tracers, green, shown at different angles. Top row shows the iLCS and tracers at the initial time,  $t_0 = 0$ . Bottom row shows the iLCS and tracers after being advected forward in time to  $T = t - t_0 = 1.309$ .

analysis of these flows more quickly than traditional LCS analysis. This faster analysis would in turn be useful for time sensitive applications, such as search and rescue operations and hazardous release scenarios. Additionally, Lagrangian diagnostics, such as the FTLE, have recently been used to improve the calculation of reduced order models (ROMs) [24]. In place of these Lagrangian diagnostics, the higher order Eulerian diagnostics derived in

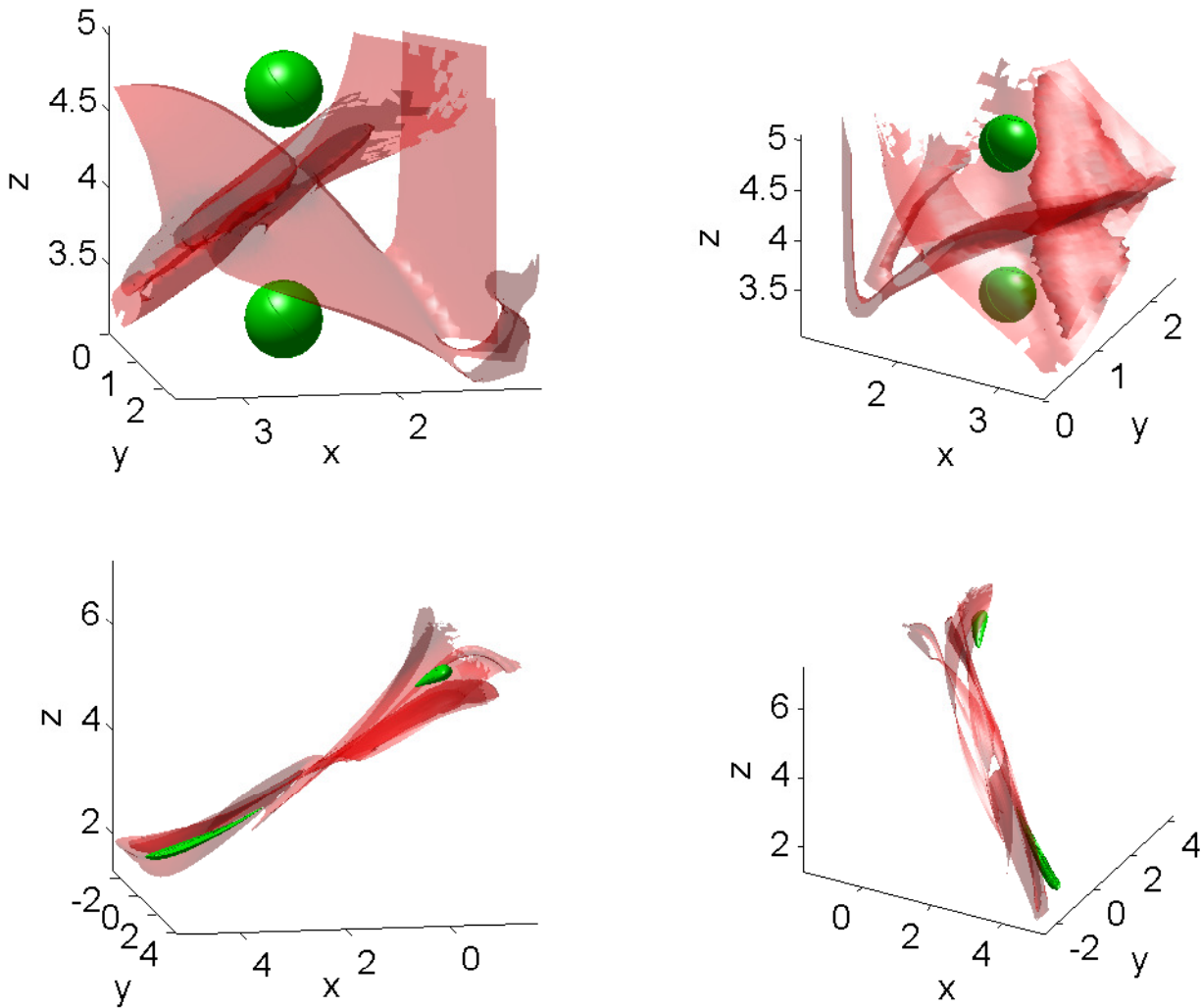


Figure 2.14: A repelling 3D iLCS, red, with a blob of passive tracers, green, shown at different angles. Top row shows the iLCS and tracers at the initial time,  $t_0 = 0$ . Bottom row shows the iLCS and tracers after being advected forward in time to  $T = t - t_0 = 1.309$ .

this manuscript could be used to improve ROMs. This would reduce both the time and the computational power needed to generate these ROMs.

Future work on this topic will explore: the existence of iLCSs embedding within higher-dimensional iLCSs, the application of iLCSs and higher order FTLE approximations to experimental data, the application of higher order FTLE approximation to ROMs, and

finding a way to determine the interval over which Eulerian diagnostics are most effective.

## Appendix A

### A.1 Expansion of the right Cauchy-Green tensor $\mathbf{C}$

Evaluation of the flow map and therefore the right Cauchy-Green tensor  $\mathbf{C}_{t_0}^t$ , from (2.5), can be computationally expensive. Therefore, this section seeks an instantaneous approximation that gives the leading order behavior of this tensor field, expanded in terms of the integration time  $T = t - t_0$ .

For tensor fields in what follows, the dependence on  $\mathbf{x}_0$  and  $t_0$  will be notationally dropped for clarity, as it will be understood. For small time  $T$ , the right Cauchy-Green tensor,  $\mathbf{C}$ , may be expanded, as in [17], in terms of the integration time  $T$ ,

$$\mathbf{C} = \mathbf{C}|_{T=0} + \left. \frac{d\mathbf{C}}{dT} \right|_{T=0} T + \frac{1}{2!} \left. \frac{d^2\mathbf{C}}{dT^2} \right|_{T=0} T^2 + \frac{1}{3!} \left. \frac{d^3\mathbf{C}}{dT^3} \right|_{T=0} T^3 + \mathcal{O}(T^4). \quad (2.76)$$

where the dependence on the initial position and time is understood. Because all derivatives are evaluated at  $T = 0$ ,  $\left. \frac{d}{dt} \right|_{t=t_0} = \left. \frac{d}{dT} \right|_{T=0}$ . The first term on the right denotes the situation of no deformation, therefore,  $\mathbf{C}|_{T=0} = \mathbb{1}$ . The derivatives of the right Cauchy-Green tensor are given by the Rivlin-Ericksen tensors [17, 25],

$$\begin{aligned} \frac{d^k\mathbf{C}}{dt^k} &= \nabla \frac{d\mathbf{x}}{dt} + \left( \nabla \frac{d\mathbf{x}}{dt} \right)^T, & k = 1, \\ \frac{d^k\mathbf{C}}{dt^k} &= \nabla \frac{d^k\mathbf{x}}{dt^k} + \left( \nabla \frac{d^k\mathbf{x}}{dt^k} \right)^T + \sum_{i=1}^{k-1} \binom{k}{i} \left( \nabla \frac{d^i\mathbf{x}}{dt^i} \right)^T \nabla \frac{d^{k-i}\mathbf{x}}{dt^{k-i}}, & k \geq 2. \end{aligned} \quad (2.77)$$

For small  $|T| \ll 1$ , the leading order behavior is given by the first Rivlin-Ericksen tensor

$(\nabla \mathbf{v} + (\nabla \mathbf{v})^T)$ , which is twice  $\mathbf{S}$ . The second-order term is,

$$\begin{aligned} \frac{d^2 \mathbf{C}}{dt^2} &= \nabla \frac{d^2 \mathbf{x}}{dt^2} + \left( \nabla \frac{d^2 \mathbf{x}}{dt^2} \right)^T + 2 \left( \nabla \frac{d\mathbf{x}}{dt} \right)^T \nabla \frac{d\mathbf{x}}{dt}, \\ &= \nabla \frac{d\mathbf{v}}{dt} + \left( \nabla \frac{d\mathbf{v}}{dt} \right)^T + 2 (\nabla \mathbf{v})^T \nabla \mathbf{v}, \\ &= 2\mathbf{B} \end{aligned} \tag{2.78}$$

where  $\mathbf{B}$  is the same as given in (2.13).

The third-order term is

$$\begin{aligned} \frac{d^3 \mathbf{C}}{dt^3} &= \nabla \frac{d^3 \mathbf{x}}{dt^3} + \left( \nabla \frac{d^3 \mathbf{x}}{dt^3} \right)^T + 3 \left[ \left( \nabla \frac{d\mathbf{x}}{dt} \right)^T \nabla \frac{d^2 \mathbf{x}}{dt^2} + \left( \nabla \frac{d^2 \mathbf{x}}{dt^2} \right)^T \nabla \frac{d\mathbf{x}}{dt} \right], \\ &= \nabla \frac{d\mathbf{a}}{dt} + \left( \nabla \frac{d\mathbf{a}}{dt} \right)^T + 3 \left[ (\nabla \mathbf{v})^T \nabla \mathbf{a} + (\nabla \mathbf{a})^T \nabla \mathbf{v} \right] \\ &= 3\mathbf{Q} \end{aligned} \tag{2.79}$$

where

$$\mathbf{Q} \equiv \frac{1}{3} \left[ \nabla \frac{d\mathbf{a}}{dt} + \left( \nabla \frac{d\mathbf{a}}{dt} \right)^T \right] + \left[ (\nabla \mathbf{v})^T \nabla \mathbf{a} + (\nabla \mathbf{a})^T \nabla \mathbf{v} \right] \tag{2.80}$$

The expansion of the right Cauchy-Green tensor (2.76) can be written as,

$$\begin{aligned} \mathbf{C} &= \mathbb{1} + 2T\mathbf{S} + T^2\mathbf{B} + \frac{1}{2}T^3\mathbf{Q} + \mathcal{O}(T^4), \\ &= \mathbb{1} + 2T \left( \mathbf{S} + \frac{1}{2}T\mathbf{B} + \left(\frac{1}{2}T\right)^2\mathbf{Q} + \mathcal{O}(T^3) \right). \end{aligned} \tag{2.81}$$

## A.2 Proof of Eq. (2.16)

Let  $\mathbf{A}$  be an  $n \times n$  matrix,  $\lambda$  an eigenvalue of  $\mathbf{A}$ ,  $\boldsymbol{\xi}$  an eigenvector of  $\mathbf{A}$ ,  $\mathbb{1}$  be the  $n \times n$  identity matrix and  $c \in \mathbb{R}$ .

By the definition of an eigenvalue we have  $\mathbf{A}\boldsymbol{\xi} = \lambda\boldsymbol{\xi}$  thus,

$$(\mathbf{A} + c \mathbb{1}) \boldsymbol{\xi} = \mathbf{A} \boldsymbol{\xi} + c \boldsymbol{\xi} = \lambda \boldsymbol{\xi} + c \boldsymbol{\xi} = (\lambda + c) \boldsymbol{\xi}. \quad (2.82)$$

Therefore, if  $\lambda$  is an eigenvalue of  $\mathbf{A}$ , then  $(\lambda + c)$  is an eigenvalue for  $\mathbf{A} + c \mathbb{1}$ .

### A.3 Eigenvalues of the Taylor expanded Cauchy-Green tensor

Let  $\mathbf{S}$  be a real, symmetric  $n \times n$  matrix with  $n$  distinct eigenvalues, and let  $\mathbf{B}$  and  $\mathbf{Q}$  also be real, symmetric  $n \times n$  matrices. We seek the eigenvalues of

$$\mathbf{S}_\varepsilon = \mathbf{S} + \varepsilon \mathbf{B} + \varepsilon^2 \mathbf{Q}, \quad (2.83)$$

a perturbation of  $\mathbf{S}$ , where  $\varepsilon$  is a small scalar. In our case, from (2.81), our small parameter is  $\varepsilon = \frac{1}{2}T$ .

Consider the eigenvalue  $\lambda_0$  of  $\mathbf{S}$  with corresponding normalized eigenvector  $\boldsymbol{\xi}_0$ . Let's refer to the perturbed eigenvalue and corresponding perturbed eigenvector of  $\mathbf{S}_\varepsilon$  as  $\lambda_\varepsilon$  and  $\boldsymbol{\xi}_\varepsilon$ . We can expand  $\boldsymbol{\xi}_\varepsilon$  and  $\lambda_\varepsilon$  in powers of  $\varepsilon$  as

$$\boldsymbol{\xi}_\varepsilon = \boldsymbol{\xi}_0 + \varepsilon \boldsymbol{\xi}_1 + \varepsilon^2 \boldsymbol{\xi}_2 + \mathcal{O}(\varepsilon^3), \quad (2.84)$$

$$\lambda_\varepsilon = \lambda_0 + \varepsilon \lambda_1 + \varepsilon^2 \lambda_2 + \mathcal{O}(\varepsilon^3). \quad (2.85)$$

The eigenvector equation  $\mathbf{S}_\varepsilon \boldsymbol{\xi}_\varepsilon = \lambda_\varepsilon \boldsymbol{\xi}_\varepsilon$  can be approximated as

$$(\mathbf{S} + \varepsilon \mathbf{B} + \varepsilon^2 \mathbf{Q})(\boldsymbol{\xi}_0 + \varepsilon \boldsymbol{\xi}_1 + \varepsilon^2 \boldsymbol{\xi}_2) = (\lambda_0 + \varepsilon \lambda_1 + \varepsilon^2 \lambda_2)(\boldsymbol{\xi}_0 + \varepsilon \boldsymbol{\xi}_1 + \varepsilon^2 \boldsymbol{\xi}_2) \quad (2.86)$$

which leads to the following three expressions, corresponding to the order one terms, order

$\varepsilon$ , and order  $\varepsilon^2$  terms, respectively,

$$\mathbf{S}\boldsymbol{\xi}_0 = \lambda_0\boldsymbol{\xi}_0, \quad (2.87)$$

$$\mathbf{S}\boldsymbol{\xi}_1 + \mathbf{B}\boldsymbol{\xi}_0 = \lambda_0\boldsymbol{\xi}_1 + \lambda_1\boldsymbol{\xi}_0, \quad (2.88)$$

$$\mathbf{S}\boldsymbol{\xi}_2 + \mathbf{B}\boldsymbol{\xi}_1 + \mathbf{Q}\boldsymbol{\xi}_0 = \lambda_0\boldsymbol{\xi}_2 + \lambda_1\boldsymbol{\xi}_1 + \lambda_2\boldsymbol{\xi}_0. \quad (2.89)$$

Multiply (2.88) by  $\boldsymbol{\xi}_0^T$  to get

$$\boldsymbol{\xi}_0^T \mathbf{S}\boldsymbol{\xi}_1 + \boldsymbol{\xi}_0^T \mathbf{B}\boldsymbol{\xi}_0 = \lambda_0 \boldsymbol{\xi}_0^T \boldsymbol{\xi}_1 + \lambda_1 \boldsymbol{\xi}_0^T \boldsymbol{\xi}_0 \quad (2.90)$$

Since  $\boldsymbol{\xi}_0$  is normalized,  $\boldsymbol{\xi}_0^T \boldsymbol{\xi}_0 = 1$ . Also, since  $\mathbf{S}$  is symmetric, we have

$$\begin{aligned} \boldsymbol{\xi}_0^T \mathbf{S}\boldsymbol{\xi}_1 &= (\boldsymbol{\xi}_1^T \mathbf{S}\boldsymbol{\xi}_0)^T \\ &= (\boldsymbol{\xi}_1^T \lambda_0 \boldsymbol{\xi}_0)^T \\ &= \lambda_0 \boldsymbol{\xi}_0^T \boldsymbol{\xi}_1 \end{aligned} \quad (2.91)$$

where we used (2.87). Now (2.90) is

$$\lambda_0 \boldsymbol{\xi}_0^T \boldsymbol{\xi}_1 + \boldsymbol{\xi}_0^T \mathbf{B}\boldsymbol{\xi}_0 = \lambda_0 \boldsymbol{\xi}_0^T \boldsymbol{\xi}_1 + \lambda_1 \quad (2.92)$$

Thus,

$$\lambda_1 = \boldsymbol{\xi}_0^T \mathbf{B}\boldsymbol{\xi}_0, \quad (2.93)$$

which, since  $\mathbf{B}$  is symmetric, represents a quadratic form.

We can put bounds on the term  $\boldsymbol{\xi}_0^T \mathbf{B}\boldsymbol{\xi}_0$ , noting that  $\boldsymbol{\xi}_0$  is a unit vector. If  $b_n$  is the maximum eigenvalue of  $\mathbf{B}$ , then

$$\max_{\boldsymbol{\xi}_0} \boldsymbol{\xi}_0^T \mathbf{B}\boldsymbol{\xi}_0 = b_n \quad (2.94)$$

Similarly, if  $b_1$  is the minimum eigenvalue of  $\mathbf{B}$ , then

$$\min_{\xi_0} \xi_0^T \mathbf{B} \xi_0 = b_1 \quad (2.95)$$

So

$$\lambda_1 = \xi_0^T \mathbf{B} \xi_0 \in [b_1, b_n] \quad (2.96)$$

So (2.85) becomes

$$\lambda_\varepsilon = \lambda_0 + \varepsilon \lambda_1 + \mathcal{O}(\varepsilon^2) \quad (2.97)$$

where  $\lambda_1$  is from (2.93).

With  $\lambda_1$  in hand, we can also determine  $\xi_1$ , which solves the following re-arranged version of (2.88),

$$(\mathbf{S} - \lambda_0 \mathbb{1}) \xi_1 = -(\mathbf{B} - \lambda_1 \mathbb{1}) \xi_0 \quad (2.98)$$

Note that  $(\mathbf{S} - \lambda_0 \mathbb{1})$  is not invertible as it has zero determinant, since  $\lambda_0$  is an eigenvalue of  $\mathbf{S}$ . The null space of  $(\mathbf{S} - \lambda_0 \mathbb{1})$  is  $\text{span}\{\xi_0\}$ . Note that (2.98) is of the form  $\mathbf{A}\mathbf{x} = \mathbf{b}$  with a square matrix  $\mathbf{A}$  of nullity 1 and a vector  $\mathbf{b}$  which is in the image of  $\mathbf{A}$ , as shown below.

Note that the vector  $\mathbf{B}\xi_0$  can be written as,

$$\mathbf{B}\xi_0 = \lambda_1 \xi_0 + d \xi_0'^{\perp}, \quad (2.99)$$

where  $d \in \mathbb{R}$  and  $\xi_0'^{\perp}$  is, in general, a vector in  $\text{im}(\mathbf{S} - \lambda_0 \mathbb{1})$ . We know that the coefficient of  $\xi_0$  in (2.99) is  $\lambda_1$  from (2.93).

The right-hand side of (2.98) can be written as,

$$-\mathbf{B}\xi_0 + \lambda_1 \xi_0 = -d \xi_0'^{\perp} \quad (2.100)$$

since the  $\lambda_1 \boldsymbol{\xi}_0$  terms cancel. This means the right-hand side of (2.98) is a vector  $\mathbf{b}$  which is in  $\text{im}(\mathbf{S} - \lambda_0 \mathbb{1})$ , the image of the operator on the left-hand side of (2.98).

We can further determine  $\lambda_2$  by multiplying (2.89) by  $\boldsymbol{\xi}_0^T$  to get, by a similar procedure as before,

$$\lambda_0 \boldsymbol{\xi}_0^T \boldsymbol{\xi}_2 + \boldsymbol{\xi}_0^T \mathbf{B} \boldsymbol{\xi}_1 + \boldsymbol{\xi}_0^T \mathbf{Q} \boldsymbol{\xi}_0 = \lambda_0 \boldsymbol{\xi}_0^T \boldsymbol{\xi}_2 + \lambda_1 \boldsymbol{\xi}_0^T \boldsymbol{\xi}_1 + \lambda_2. \quad (2.101)$$

Thus,

$$\lambda_2 = \boldsymbol{\xi}_0^T \mathbf{Q} \boldsymbol{\xi}_0 + \boldsymbol{\xi}_0^T \mathbf{B} \boldsymbol{\xi}_1 - \lambda_1 \boldsymbol{\xi}_0^T \boldsymbol{\xi}_1. \quad (2.102)$$

But take the transpose and we see,

$$\lambda_2 = \boldsymbol{\xi}_0^T \mathbf{Q} \boldsymbol{\xi}_0 + \boldsymbol{\xi}_1^T (\mathbf{B} - \lambda_1 \mathbb{1}) \boldsymbol{\xi}_0, \quad (2.103)$$

$$= \boldsymbol{\xi}_0^T \mathbf{Q} \boldsymbol{\xi}_0 - \boldsymbol{\xi}_1^T (\mathbf{S} - \lambda_0 \mathbb{1}) \boldsymbol{\xi}_1, \quad (2.104)$$

where we used (2.98). We can write  $\boldsymbol{\xi}_1$  as

$$\boldsymbol{\xi}_1 = a \boldsymbol{\xi}_0 + b \boldsymbol{\xi}_0^\perp, \quad (2.105)$$

where  $a, b \in \mathbb{R}$  and  $\boldsymbol{\xi}_0^\perp \in \text{im}(\mathbf{S} - \lambda_0 \mathbb{1})$ , which is, in general, not equal to  $\boldsymbol{\xi}_0'^\perp$ . Hence,

$$\lambda_2 = \boldsymbol{\xi}_0^T \mathbf{Q} \boldsymbol{\xi}_0 - b^2 \boldsymbol{\xi}_0'^{\perp T} (\mathbf{S} - \lambda_0 \mathbb{1}) \boldsymbol{\xi}_0^\perp, \quad (2.106)$$

therefore the only part of  $\boldsymbol{\xi}_1$  which contributes to  $\lambda_2$  is the part which is in the image of  $(\mathbf{S} - \lambda_0 \mathbb{1})$ .

When dealing with a 2-dimensional flow field,  $\text{im}(\mathbf{S} - \lambda_0 \mathbb{1})$  is just a 1-dimensional subspace of  $\mathbb{R}^2$ , and thus  $\boldsymbol{\xi}_0'^\perp$  in (2.100) is parallel to  $\boldsymbol{\xi}_0^\perp$  in (2.105). Without loss of generality, we can

take them to be equal unit vectors,  $\boldsymbol{\xi}_0^\perp = \boldsymbol{\xi}'_0{}^\perp$ . Thus, (2.98) becomes

$$b(\mathbf{S} - \lambda_0 \mathbb{1})\boldsymbol{\xi}_0^\perp = -d\boldsymbol{\xi}_0^\perp, \quad (2.107)$$

or,

$$(\mathbf{S} - \lambda_0 \mathbb{1})\boldsymbol{\xi}_0^\perp = -\frac{d}{b}\boldsymbol{\xi}_0^\perp, \quad (2.108)$$

which is an eigenvector equation for the matrix  $(\mathbf{S} - \lambda_0 \mathbb{1})$  with the eigenvector  $\boldsymbol{\xi}_0^\perp$  and corresponding eigenvalue  $\mu = -\frac{d}{b}$ , assuming  $b \neq 0$ . Note that if  $b = 0$ , then we also have  $d = 0$ , from (2.107).

For 2-dimensional flows, from  $\boldsymbol{\xi}_0$ , we can obtain  $\boldsymbol{\xi}_0^\perp$  from a  $90^\circ$  counterclockwise rotation,

$$\boldsymbol{\xi}_0^\perp = \mathbf{R}\boldsymbol{\xi}_0, \quad (2.109)$$

where

$$\mathbf{R} = \begin{bmatrix} 0 & -1 \\ 1 & 0 \end{bmatrix}. \quad (2.110)$$

We use  $\boldsymbol{\xi}_0^\perp$  so obtained to calculate  $\mu$  from (2.108) for the case  $d \neq 0$ , which becomes the following eigenvector equation for  $\mathbf{R}^T(\mathbf{S} - \lambda_0 \mathbb{1})\mathbf{R}$  with eigenvector  $\boldsymbol{\xi}_0$ ,

$$\mathbf{R}^T(\mathbf{S} - \lambda_0 \mathbb{1})\mathbf{R}\boldsymbol{\xi}_0 = \mu\boldsymbol{\xi}_0, \quad (2.111)$$

Therefore we obtain  $\mu$  by taking the dot product with  $\boldsymbol{\xi}_0$ ,

$$\mu = \boldsymbol{\xi}_0^T \mathbf{R}^T (\mathbf{S} - \lambda_0 \mathbb{1}) \mathbf{R} \boldsymbol{\xi}_0, \quad (2.112)$$

and we obtain  $d$  from (2.100), noting that  $\boldsymbol{\xi}_0^{\perp T} \boldsymbol{\xi}_0 = 0$ ,

$$\begin{aligned} d &= \boldsymbol{\xi}_0^{\perp T} \mathbf{B} \boldsymbol{\xi}_0, \\ &= \boldsymbol{\xi}_0^T \mathbf{R}^T \mathbf{B} \boldsymbol{\xi}_0. \end{aligned} \tag{2.113}$$

Thus, (2.106), for 2-dimensional systems, simplifies to,

$$\lambda_2 = \begin{cases} \boldsymbol{\xi}_0^T \mathbf{Q} \boldsymbol{\xi}_0, & \text{if } d = 0 \\ \boldsymbol{\xi}_0^T \mathbf{Q} \boldsymbol{\xi}_0 - \frac{d^2}{\mu}, & \text{if } d \neq 0 \end{cases} \tag{2.114}$$

where  $d$  and  $\mu$  are from (2.113) and (2.112), respectively.

#### A.4 Details for Time-Varying Double-Gyre Example

The acceleration field,  $\mathbf{a} = \frac{d}{dt} \mathbf{v} = (a_x, a_y)$ , for the double-gyre, (2.64), is given by

$$\begin{aligned} a_x &= -\pi^2 A \cos(\pi f) \cos(\pi y) \frac{\partial f}{\partial t} + \frac{1}{2} \pi^3 A^2 \sin(2\pi f) \frac{\partial f}{\partial x}, \\ a_y &= \pi^2 A \left[ -\sin(\pi f) \sin(\pi y) \frac{\partial f}{\partial x} \frac{\partial f}{\partial t} + \frac{1}{\pi} \cos(\pi f) \sin(\pi y) \frac{\partial^2 f}{\partial x \partial t} \right] \\ &\quad + \frac{1}{2} \pi^3 A^2 \sin(2\pi y) \left[ \sin^2(\pi f) \frac{\partial f}{\partial x} + \cos^2(\pi f) \left( \frac{\partial f}{\partial x} \right)^2 - \frac{1}{2\pi} \sin(2\pi f) \frac{\partial^2 f}{\partial x^2} \right], \end{aligned} \tag{2.115}$$

where the dependence of the term  $f$  is understood.

The components of the symmetric  $\mathbf{B}$  matrix are,

$$\begin{aligned} B_{xx} &= -A\pi^2 \cos(\pi f) \cos(\pi y) \frac{\partial^2 f}{\partial x \partial t} + \frac{1}{2} A\pi^3 \sin(2\pi f) \frac{\partial f}{\partial x} \frac{\partial f}{\partial t} \\ &\quad + A^2 \pi^3 \sin(2\pi f) \frac{\partial^2 f}{\partial x^2} \left( \frac{1}{2} - \sin^2(\pi y) \left( \frac{\partial f}{\partial x} \right)^2 \right) + A^2 \pi^4 \cos(2\pi f) \left( \frac{\partial f}{\partial x} \right)^2 \\ &\quad + A^2 \pi^4 \sin^2(\pi f) \sin^2(\pi y) \left( \frac{\partial f}{\partial x} \right)^4 + A^2 \pi^2 \cos^2(\pi f) \sin^2(\pi y) \frac{\partial^2 f}{\partial x^2} \\ &\quad + A^2 \pi^4 \cos^2(\pi f) \cos^2(\pi y) \left( \frac{\partial f}{\partial x} \right)^2, \end{aligned} \tag{2.116}$$

$$\begin{aligned}
B_{xy} &= \frac{1}{2}A\pi \cos(\pi f) \sin(\pi y) \left[ \frac{\partial^3 f}{\partial x^2 \partial t} + \pi^2 \left( 1 - \left( \frac{\partial f}{\partial x} \right)^2 \right) \right] \\
&\quad - A\pi^2 \sin(\pi f) \sin(\pi y) \left( \frac{\partial f}{\partial x} \frac{\partial^2 f}{\partial x \partial t} - \frac{1}{2} \frac{\partial^2 f}{\partial x^2} \frac{\partial f}{\partial t} \right) \\
&\quad - \frac{1}{4}A^2\pi^4 \sin(2\pi f) \sin(2\pi y) \left[ \frac{\partial f}{\partial x} \left( 1 + \left( \frac{\partial f}{\partial x} \right)^2 \right) + \frac{1}{2} \frac{\partial^3 f}{\partial x^3} \right],
\end{aligned} \tag{2.117}$$

$$\begin{aligned}
B_{yy} &= A\pi^2 \cos(\pi f) \cos(\pi y) \frac{\partial^2 f}{\partial x \partial t} - A\pi^3 \sin(\pi f) \cos(\pi y) \frac{\partial f}{\partial x} \frac{\partial f}{\partial t} \\
&\quad - \frac{1}{2}A^2\pi^3 \sin(2\pi f) \sin(2\pi y) \frac{\partial^2 f}{\partial x^2} \\
&\quad + A^2\pi^4 \cos^2(\pi f) \cos^2(\pi y) \left( \frac{\partial f}{\partial x} \right)^2 + A^2\pi^4 \sin^2(\pi f) \sin^2(\pi y) \\
&\quad + A^2\pi^4 \left( \frac{\partial f}{\partial x} \right)^2 \left( \cos^2(\pi f) - \sin^2(\pi y) \right).
\end{aligned} \tag{2.118}$$

The normalized eigenvector of  $\mathbf{S}(\mathbf{x}_0, t_0)$  corresponding to the eigenvalue  $s_1(\mathbf{x}_0, t_0)$  given in (2.66) is,

$$\boldsymbol{\xi}_{s_1} = \begin{bmatrix} \xi_x \\ \xi_y \end{bmatrix} = \frac{1}{N} \begin{bmatrix} \frac{1}{2}\alpha \\ \bar{s}_1 + \beta \end{bmatrix} \tag{2.119}$$

where

$$\begin{aligned}
\bar{s}_1 &= \frac{s_1}{\pi^2 A} = -\frac{1}{2}\sqrt{\alpha^2 + 4\beta^2}, \\
N &= \sqrt{\frac{1}{4}\alpha^2 + (\bar{s}_1 + \beta)^2}, \\
\alpha &= \sin(\pi f) \sin(\pi y) \left( 1 - \frac{\partial f}{\partial x} \right) + \frac{1}{\pi} \cos(\pi f) \sin(\pi y) \frac{\partial^2 f}{\partial x^2}, \\
\beta &= \cos(\pi f) \cos(\pi y) \frac{\partial f}{\partial x}
\end{aligned} \tag{2.120}$$

The coefficient of  $T$  in the approximation of the backward FTLE for the double gyre is thus given by  $s_1^2 - \frac{1}{2}\boldsymbol{\xi}_{s_1}^T \mathbf{B} \boldsymbol{\xi}_{s_1}$  which can be expressed as,

$$a(\mathbf{x}_0, t_0) = s_1^2 - \frac{1}{2}(B_{xx}\xi_x^2 + 2B_{xy}\xi_x\xi_y + B_{yy}\xi_y^2), \tag{2.121}$$

using the above formulas. This yields a backward time FTLE approximation for small

backward times  $T < 0$  of,

$$\sigma_{t_0}^{t_0+T}(\mathbf{x}_0) = s_1(\mathbf{x}_0, t_0) + a(\mathbf{x}_0, t_0)T + \mathcal{O}(T^2). \quad (2.122)$$

We note that the first and second terms have explicit dependence on both initial position and initial time.

**Funding:** This research was supported in part by grants from the National Science Foundation (NSF) under grant numbers AGS 1520825 (Hazards SEES: Advanced Lagrangian Methods for Prediction, Mitigation and Response to Environmental Flow Hazards) and DMS 1821145 (Data-Driven Computation of Lagrangian Transport Structure in Realistic Flows). Any opinions, findings, and conclusions or recommendations expressed in this material are those of the authors and do not necessarily reflect the views of the sponsors.

**Acknowledgments:** We thank Hosein Foroutan for providing us with WRF model data, Nicole Abaid for help with the perturbation analysis, Gary Nave for fruitful conversations related to some of the ideas covered in this work during their nascent stage, Siavash Ameli and the Shadden Lab for developing and maintaining the TRACE server.

**Conflicts of interest:** The authors declare no conflict of interest.

**Abbreviations:** The following abbreviations are used in this manuscript,

FTLE	Finite-time Lyapunov exponent
LCS	Lagrangian coherent structure
iLCS	Infinitesimal-time LCS
OECS	Objective Eulerian coherent structure
WRF	Weather research and forecasting
NAM	North American Mesoscale model
RMSE	Root-mean-square error

# Bibliography

- [1] Shawn C Shadden, Francois Lekien, and Jerrold E Marsden. Definition and properties of Lagrangian coherent structures from finite-time Lyapunov exponents in two-dimensional aperiodic flows. *Physica D: Nonlinear Phenomena*, 212(3):271–304, 2005.
- [2] Benjamin Schindler, Ronald Peikert, Raphael Fuchs, and Holger Theisel. Ridge concepts for the visualization of Lagrangian coherent structures. *Topological Methods in Data Analysis and Visualization II*, pages 221–235, 2012.
- [3] Carmine Senatore and Shane D Ross. Detection and characterization of transport barriers in complex flows via ridge extraction of the finite time Lyapunov exponent field. *International Journal for Numerical Methods in Engineering*, 86(9):1163–1174, 2011.
- [4] Phanindra Tallapragada and Shane D Ross. A set oriented definition of finite-time Lyapunov exponents and coherent sets. *Communications in Nonlinear Science and Numerical Simulation*, 18(5):1106–1126, 2013.
- [5] Amir E BozorgMagham, Shane D Ross, and David G Schmale III. Real-time prediction of atmospheric Lagrangian coherent structures based on forecast data: An application and error analysis. *Physica D: Nonlinear Phenomena*, 258:47–60, 2013.
- [6] Amir E BozorgMagham and Shane D Ross. Atmospheric Lagrangian coherent struc-

- tures considering unresolved turbulence and forecast uncertainty. *Communications in Nonlinear Science and Numerical Simulation*, 22(1):964–979, 2015.
- [7] Phanindra Tallapragada, Shane D Ross, and David G Schmale III. Lagrangian coherent structures are associated with fluctuations in airborne microbial populations. *Chaos*, 21:033122, 2011.
- [8] David G Schmale III and Shane D Ross. Highways in the sky: Scales of atmospheric transport of plant pathogens. *Annual Review of Phytopathology*, 53:591–611, 2015.
- [9] David G Schmale III and Shane D Ross. High-flying microbes: Aerial drones and chaos theory help researchers explore the many ways that microorganisms spread havoc around the world. *Scientific American*, February:32–37, 2017.
- [10] Amir E BozorgMagham, Shane D Ross, and David G Schmale III. Local finite-time Lyapunov exponent, local sampling and probabilistic source and destination regions. *Nonlinear Processes in Geophysics*, 22(6):663–677, 2015.
- [11] Jifeng Peng and Rorik Peterson. Attracting structures in volcanic ash transport. *Atmospheric environment*, 48:230–239, 2012.
- [12] Daniel Garaboa-Paz, Jorge Eiras-Barca, Florian Huhn, and Vicente Pérez-Muñuzuri. Lagrangian coherent structures along atmospheric rivers. *Chaos: An Interdisciplinary Journal of Nonlinear Science*, 25(6):063105, 2015.
- [13] George Haller. A variational theory of hyperbolic Lagrangian coherent structures. *Physica D: Nonlinear Phenomena*, 240(7):574–598, 2011.
- [14] George Haller. Lagrangian coherent structures. *Annual Review of Fluid Mechanics*, 47(1):137–162, 2015. doi: 10.1146/annurev-fluid-010313-141322. URL <https://doi.org/10.1146/annurev-fluid-010313-141322>.

- [15] Alireza Hadjighasem, Mohammad Farazmand, Daniel Blazevski, Gary Froyland, and George Haller. A critical comparison of lagrangian methods for coherent structure detection. *Chaos: An Interdisciplinary Journal of Nonlinear Science*, 27(5):053104, 2017.
- [16] Mattia Serra and George Haller. Objective Eulerian coherent structures. *Chaos: An Interdisciplinary Journal of Nonlinear Science*, 26(5):053110, 2016.
- [17] Gary K Nave Jr, Peter J Nolan, and Shane D Ross. Trajectory-free approximation of phase space structures using the trajectory divergence rate. *Nonlinear Dynamics*, 2019.
- [18] Peter J Nolan, James Pinto, Javier González-Rocha, Anders Jensen, Christina Vezzi, Sean Bailey, Gijs de Boer, Constantin Diehl, Roger Laurence, Craig Powers, Hosein Foroutan, Shane D Ross, and David G Schmale III. Coordinated unmanned aircraft system (UAS) and ground-based weather measurements to predict Lagrangian coherent structures (LCSs). *Sensors*, 18(12):4448, 2018.
- [19] Ronald Peikert, Benjamin Schindler, and Robert Carnecky. Ridge surface methods for the visualization of Lagrangian coherent structures. In *Proceedings of the Ninth International Conference on Flow Dynamics, Sendai, Japan*, pages 206–207, 2012.
- [20] Weather research and forecasting model. <https://www.mmm.ucar.edu/weather-research-and-forecasting-model>. Accessed: 2019-02-02.
- [21] Vladimir I Arnold. *Sur la topologie des écoulements stationnaires des fluides parfaits*, pages 15–18. Springer Berlin Heidelberg, Berlin, Heidelberg, 2014. ISBN 978-3-642-31031-7. doi: 10.1007/978-3-642-31031-7\_3. URL [https://doi.org/10.1007/978-3-642-31031-7\\_3](https://doi.org/10.1007/978-3-642-31031-7_3).
- [22] Thierry Dombre, Uriel Frisch, John M Greene, Michel Hénon, A Mehr, and Andrew M

- Soward. Chaotic streamlines in the abc flows. *Journal of Fluid Mechanics*, 167:353–391, 1986.
- [23] Michel Henon. Sur la topologie des lignes de courant dans un cas particulier. *Comptes Rendus Acad. Sci. Paris A*, 262:312–314, 1966.
- [24] Xuping Xie, Peter J Nolan, Shane D Ross, and Traian Iliescu. Lagrangian data-driven reduced order modeling of finite time Lyapunov exponents, 2019. <https://arxiv.org/abs/1808.05635>.
- [25] Clifford Truesdell and Walter Noll. The non-linear field theories of mechanics. In *The non-linear field theories of mechanics*, pages 1–579. Springer, 2004.

## Chapter 3

# A Method for Detecting Atmospheric Lagrangian Coherent Structures using a Single Fixed-Wing Unmanned Aircraft System

### Attribution

This manuscript represents a collaborative work with Hunter G. McClelland, Craig A. Woolsey, and Shane D. Ross which has been submitted to the journal *Sensors*.

Peter J. Nolan computed the Lagrangian-Eulerian diagnostics, analyzed data, and led the writing of the manuscript. Hunter G. McClelland performed the UAS simulations, analyzed data, and assisted with writing the manuscript. Craig A. Woolsey and Shane D. Ross managed the project, assisted in analyzing the data, and assisted in writing the manuscript.

## abstract

The transport of material through the atmosphere is an issue with wide ranging implications for fields as diverse as agriculture, aviation, and human health. Due to the unsteady nature of the atmosphere, predicting how material will be transported via Earth's wind field is challenging. Lagrangian diagnostics, such as Lagrangian coherent structures (LCSs), have been used to discover the most significant regions of material collection or dispersion. However, Lagrangian diagnostics can be time consuming to calculate and often rely on weather forecasts that may not be completely accurate. Recently, Eulerian diagnostics have been developed which can provide indications of LCS and have computational advantages over their Lagrangian counterparts. In this manuscript, a methodology is developed for estimating local Eulerian diagnostics from wind velocity data measured by a fixed-wing unmanned aircraft system (UAS) flying in circular arcs. Using a simulation environment, driven by realistic atmospheric velocity data from the North American Mesoscale (NAM) model, it is shown that the Eulerian diagnostic estimates from UAS measurements approximate the true local Eulerian diagnostics, therefore also predicting the passage of LCSs. This methodology requires only a single flying UAS, making it easier and more affordable to implement in the field than existing alternatives, such as multiple UASs and Doppler LiDAR measurements.

## 1 Introduction

The transport of material in the atmosphere is a problem with important implications for agriculture [1, 2, 3, 4], aviation [5, 6], and human health [7, 8]. Given the unsteady nature of atmospheric flows it can be difficult to predict where a fluid parcel, such as one containing an airborne pathogen, will be transported. Tools from dynamical systems theory, such as

Lagrangian coherent structures (LCSs), can help us to understand how fluid parcels in a flow will evolve. The study of atmospheric transport from a dynamical systems perspective has long focused on the study of large scale phenomena [1, 2, 3, 4, 5, 9, 10, 11, 12]. This has been largely due to the larger scale grid spacing of readily available atmospheric model data and the lack of high resolution atmospheric measurements on a scale large enough to calculate Lagrangian data. Furthermore, this field of study has been largely relegated to numerical simulations. Few works have attempted to find ways to directly detect LCSs from experimental measurements in the field. In [6, 13] the authors used wind velocity measurements from a Doppler light detection and ranging (LiDAR) to detect LCS which had passed near Hong Kong International Airport. Rather than measure the wind velocity to try and detect LCSs, the authors of [1] looked at sudden changes in pathogen concentrations in the atmosphere. They were then able to link those changes to the passage of LCSs using atmospheric velocity data from the North American Mesoscale (NAM) Weather Research and Forecasting (WRF) model. Recent advances in dynamical systems theory, such as new Eulerian diagnostics, as well as new atmospheric sensing technology, such as unmanned aircraft systems (UAS) [14], have brought the local detection of LCSs within the reach of operators in the field at any location, without the need for expensive infrastructure. One recent paper took advantage of these new advances to attempt to predict the passage of LCSs based on experimental data. The authors of [15] used multiple sonic anemometers attached to two stationary quadcopter UASs and one tower to measure the wind velocity around the San Luis Valley in Colorado. From these wind measurements the authors were able to calculate the local attraction rate, which was then compared to the attraction rate from a WRF simulation. From these comparisons, the authors found likely indicators of LCSs associated with convective cells and a front which passed through the region. In this manuscript, we build upon these recent developments to establish a method to detect LCSs which can be readily implemented by operators in the field at any location, using only a

single fixed-wing UAS.

The first of these developments are new Eulerian techniques for measuring the attraction and repulsion of regions in a fluid flow [16, 17]. In traditional Lagrangian analyses, a velocity field is needed which is defined over a large enough spatiotemporal scale to allow the accurate simulation of fluid parcel trajectories. How the parcels are transported by the flow is then used to determine which parts of the flow are more attractive or repulsive. These new Eulerian methods do not rely on the simulation of fluid parcel trajectories; instead they are based on the instantaneous gradients of the velocity field. Since they rely on gradients, these techniques only require enough velocity data points to enact a finite-differencing scheme. Furthermore, these methods are Eulerian and thus can be applied to data sets which are temporally coarse.

The second of these developments is the use of inexpensive UASs to sample the atmospheric velocity instead of piloted aircraft or other traditional assets. Ground-based wind sensors such as LiDAR, sonic detection and ranging (SoDAR), or tower-mounted anemometers can be prohibitively expensive and difficult to relocate in real-time to regions of interest, such as a chemical spill, wild fire, or radioactive release. Airborne wind measurement from aircraft has a long history [18, 19] and well-developed existing programs, such as the NASA Airborne Science Program [20]. The advancement of UASs has enabled wind measurement missions which may be lower cost, longer duration, and can be implemented in more dangerous environments. Elston et. al. [21] provide a review of many UAS atmospheric measurement efforts, and recent works continue to advance both theoretical and practical UAS capabilities [22, 23, 24, 25, 26, 27].

This manuscript develops a methodology which will enable researchers in the field to utilize local wind measurements to detect LCSs using only a single fixed-wing UAS. This methodology will be less complex, less expensive, and less time consuming to implement than those

utilized in previous studies [1, 6, 13, 15]. Furthermore, by requiring only a single UAS, the need for expensive infrastructure and multiple pilot/spotter teams is eliminated. Additionally, since this methodology takes advantage of Eulerian diagnostics, there is no need for expensive computer clusters or time consuming trajectory integration as with Lagrangian diagnostics. This methodology is developed and tested using an observing system simulation experiment (OSSE). A Historical wind velocity forecast from the NAM model is taken and passed to a UAS flight simulator, which is assumed to have a perfect anemometer, but still includes the effects of the wind field on the aircraft's flight trajectory. The simulated UAS attempts to fly in a circular orbit about a portion of the NAM model centered on the coordinates of the Virginia Tech experimental site, Kentland Farm, figure 3.1. From wind measurements along these circular orbits, we are able to calculate the local trajectory divergence rate and attraction rate, described in section 2.1. Using these calculations it is then possible to look for signals of LCSs passing through the area.

This manuscript is organized as follows. Section 3.2.1, describes the Eulerian and Lagrangian diagnostics which are used to analyze the atmospheric velocity data. Section 3.2.2 describes the algorithm we developed to calculate the gradient of a scalar field from measurements along a circular arc, this gradient is necessary for the computation of the Eulerian diagnostics. Section 3.2.3 briefly describes the NAM model which was used, how the model data were prepared for analysis, and the flight simulator which was used. In section 3.3.1 the results of a parametric study which analyzes the ability of a UAS flying in a circular arc to approximate Eulerian diagnostics over various radii are presented. Section 3.3.2 presents results concerning the ability of Eulerian diagnostics to approximate Lagrangian diagnostics and detect LCSs passing through an area using receiver operating characteristic (ROC) curves. Due to the discrete nature of numerical computations, a parametric study to investigate various area thresholds for the detection of LCSs was performed. Section 3.3.3

presents results concerning the ability of Eulerian diagnostics, as approximated from a UAS flight, to detect LCSs passing through an area. Once again a parametric study to investigate various area thresholds for the detection of LCSs using ROC curves is performed. Section 3.4 discusses the results presented in section 3.3. Finally section 3.5 presents the conclusion of the manuscript.



Figure 3.1: Map of the Mid-Atlantic United States, Kentland Farm in Virginia is shown in red.

## 2 Methods

### 2.1 Lagrangian-Eulerian Analysis

Consider the dynamical system

$$\frac{d}{dt}\mathbf{x}(t) = \mathbf{v}(\mathbf{x}(t), t), \quad (3.1)$$

$$\mathbf{x}_0 = \mathbf{x}(t_0), \quad (3.2)$$

$$\mathbf{x} \in \mathbb{R}^2, t \in \mathbb{R}, \quad (3.3)$$

where  $\mathbf{x}(t)$  is the position vector of a fluid parcel at time  $t$  and  $\mathbf{v}(\mathbf{x}, t)$  is the time varying horizontal wind velocity vector at position  $\mathbf{x}(t)$ , time  $t$ . The components of the horizontal position vector are  $\mathbf{x} = (x, y)$ , where  $x$  is the eastward position and  $y$  is the northward position, and the horizontal velocity vector,  $\mathbf{v} = (u, v)$ , where  $u$  is the eastward velocity and  $v$  is the northward velocity. This system can be analyzed using both Lagrangian and Eulerian tools. For the Lagrangian analysis, the finite-time Lyapunov exponent (FTLE),  $\sigma$ , and LCSs are used. For this study, LCSs are defined as C-ridges of the FTLE field following [28]. The FTLE field is a measure of the stretching of fluid parcels within a flow, the forward-time FTLE measures repulsion and the backward-time FTLE measures attraction. LCSs are the most attracting and repelling material surfaces within a fluid flow; as such, they provide a means of visualizing how particles within the flow will evolve. For the Eulerian analyses the attraction rate,  $s_1$ , and the trajectory divergence rate,  $\dot{\rho}$ , are used. Both of these rates are derived from the Eulerian rate-of-strain tensor,  $\mathbf{S}$ , described below. The attraction rate is the minimum eigenvalue of  $\mathbf{S}$  and was shown in [16] to provide a measure of instantaneous hyperbolic attraction, with isolated minima of  $s_1$  providing the cores of attracting objective Eulerian coherent structures (OECS). Recent work has shown that in 2D,  $s_1$  is the limit of the

backward-time FTLE as the integration time goes to 0 and that troughs of  $s_1$  are attracting infinitesimal-time LCS (iLCS) [29]. A schematic of which can be seen in figure 3.2. The trajectory divergence rate is a measure of how much repulsion/attraction is changing along streamlines of the velocity field, as depicted in figure 3.3 [17].

To calculate the Lagrangian metrics, first calculate the flow map for the time period of interest,

$$\mathbf{F}_{t_0}^t(\mathbf{x}_0) = \mathbf{x}_0 + \int_{t_0}^t \mathbf{v}(\mathbf{x}(t), t) dt. \quad (3.4)$$

Taking the gradient of the flow map, the right Cauchy-Green strain tensor is then calculated,

$$\mathbf{C}_{t_0}^t(\mathbf{x}_0) = \nabla \mathbf{F}_{t_0}^t(\mathbf{x}_0)^T \cdot \nabla \mathbf{F}_{t_0}^t(\mathbf{x}_0), \quad (3.5)$$

with ordered eigenvalues,  $\lambda_1 \leq \lambda_2$ . From the largest eigenvalue of the right Cauchy-Green strain tensor,  $\lambda_2$ , the FTLE field is derived,

$$\sigma_{t_0}^t(\mathbf{x}_0) = \frac{1}{2|t - t_0|} \log(\lambda_2(\mathbf{x}_0)). \quad (3.6)$$

Ridges of this field can then be identified as LCSs.

For the Eulerian metrics, the Eulerian rate-of-strain tensor is defined as

$$\mathbf{S}(\mathbf{x}_0, t_0) = \frac{1}{2} (\nabla \mathbf{v}(\mathbf{x}_0, t_0) + \nabla \mathbf{v}(\mathbf{x}_0, t_0)^T), \quad (3.7)$$

with ordered eigenvalues  $s_1 \leq s_2$ . The attraction rate is defined as the minimum eigenvalue of  $\mathbf{S}$ ,  $s_1$ . The attraction rate can be directly calculated from the velocity gradient using the formula,

$$s_1 = \frac{1}{2} \left( \frac{\partial u}{\partial x} + \frac{\partial v}{\partial y} \right) - \frac{1}{2} \sqrt{\left( \frac{\partial u}{\partial x} - \frac{\partial v}{\partial y} \right)^2 + \left( \frac{\partial u}{\partial y} + \frac{\partial v}{\partial x} \right)^2}. \quad (3.8)$$

The trajectory divergence rate is defined as

$$\dot{\rho}(\mathbf{x}_0, t_0) = \hat{\mathbf{n}}(\mathbf{x}_0, t_0)^T \cdot \mathbf{S}(\mathbf{x}_0, t_0) \cdot \hat{\mathbf{n}}(\mathbf{x}_0, t_0) = \frac{(\mathbf{v}(\mathbf{x}_0, t_0)^T \cdot \mathbf{J}^T \cdot \mathbf{S}(\mathbf{x}_0, t_0) \cdot \mathbf{J} \cdot \mathbf{v}(\mathbf{x}_0, t_0))}{\|\mathbf{v}(\mathbf{x}_0, t_0)\|^2}, \quad (3.9)$$

where  $\hat{\mathbf{n}}(\mathbf{x}_0, t_0)$  is the unit vector normal to the trajectory and  $\mathbf{J}$  is the symplectic matrix,  $\mathbf{J} = \begin{bmatrix} 0 & 1 \\ -1 & 0 \end{bmatrix}$  [17].

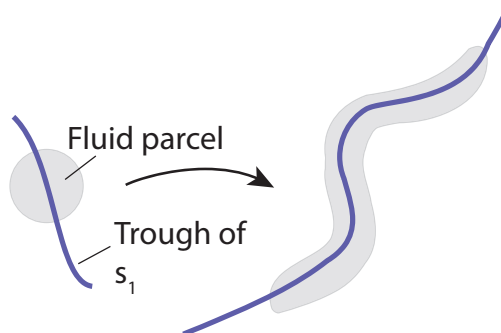


Figure 3.2: Schematic of the effect of a trough of the attraction rate,  $s_1$ , field on a fluid parcel.

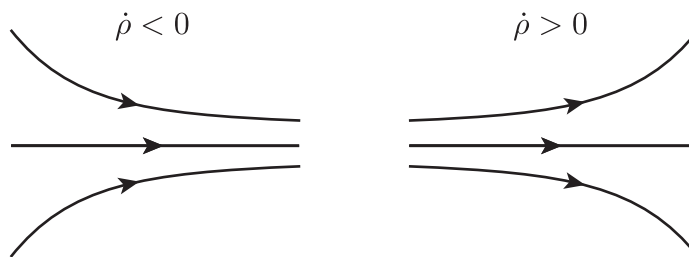


Figure 3.3: Schematic of the trajectory divergence rate. Where  $\dot{\rho} < 0$ , trajectories are converging; where  $\dot{\rho} > 0$  trajectories are diverging.

## 2.2 Gradient Approximation from UAS Flight

In order to calculate the Eulerian rate-of-strain tensor from wind measurements along a simulated UAS flight path, we have developed an algorithm to approximate the gradient of a scalar field based on measurements along a circular arc, figure 3.4. The algorithm is based on the assumption that the scalar field is not significantly changing in time during the period

of one full orbit, but is changing in space. We believe this assumption is appropriate to apply to atmospheric velocity fields, as mid to larger scale atmospheric flows tend to change on the order of hours, while UAS orbits on the spatial scale of interest are on the order of minutes. This assumption of course ignores small scale turbulent motion which would fall below the scale which is being sampled. This algorithm also assumes that the important features will be in the horizontal plane. This assumption was previously applied to atmospheric model data in [9, 10, 30] and atmospheric measurements in [15]. It is based on the fact that the vertical component of the wind velocity tends to be two orders of magnitude less than the horizontal components.

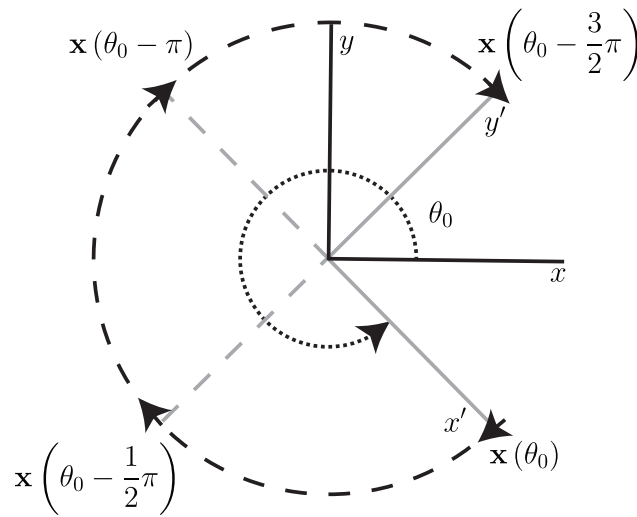


Figure 3.4: Schematic showing positions where velocity measurements were made and the position of the circle gradient frame to the reference frame.

This algorithm takes as inputs:

- a scalar field measured along a circular arc,  $f(\theta)$ , as an  $n \times 1$  array input, where  $n$  is the number of measurements taken,
- the angle  $\theta$  as a monotonically decreasing  $n \times 1$  array input,
- and the radius of the circular arc,  $r$ , which is assumed to be constant, as a scalar input.

Note, this algorithm is currently written for a clockwise trajectory. The algorithm starts with an initial point along the circular arc  $(r, \theta_0)$  and the value  $f$  at that point. Then, provided the path continues for at least another three quarters of a circle, the value of  $f$  is obtained at 3 additional points along the path at  $(r, \theta_0 - \frac{1}{2}\pi)$ ,  $(r, \theta_0 - \pi)$ , and  $(r, \theta_0 - \frac{3}{2}\pi)$ . With  $f$  at 4 individual points along the circular arc, a central finite-difference scheme is used to approximate the gradient of  $f$  at the center point of the circle. Since the 4 points are along an arc, each subsequent approximation the gradient will be in a reference frame which has a different orientation from the initial gradient approximation, figure 3.4. To correct for this apply a counterclockwise rotation to the gradient of  $f$  to obtain the gradient in a consistent reference frame oriented North-South, East-West. Continue for each additional point along the circular arc until there is less than an additional three quarters of a circle left. A pseudo-code version of this algorithm can be found in Algorithm 3.1, and a schematic can be found in figure 3.4.

**Algorithm 3.1.** Circle gradient, approximates the gradient of a scalar from samples along an arc.

**Input:**  $r, \theta, f(\theta)$

**Output:** Approximation of  $\nabla f$

1) **for:**  $i \leftarrow 1$  **to**  $\text{length}(\theta)$  **do**

2) **if**  $\theta(i) - \frac{3}{2}\pi \geq \theta(\text{end})$  **then**

3) Obtain  $f(\theta)$  at  $f(\theta(i)), f(\theta(i) - \frac{1}{2}\pi), f(\theta(i) - \pi), f(\theta(i) - \frac{3}{2}\pi)$

4)  $\frac{\partial f}{\partial x'} \approx \frac{f(\theta(i)) - f(\theta(i) - \pi)}{2 \cdot r}$

5)  $\frac{\partial f}{\partial y'} \approx \frac{f(\theta(i) - \frac{3}{2}\pi) - f(\theta(i) - \frac{1}{2}\pi)}{2 \cdot r}$

6)  $\nabla f(i) \approx \begin{bmatrix} \cos(\theta(i)) & \sin(\theta(i)) \\ -\sin(\theta(i)) & \cos(\theta(i)) \end{bmatrix} \begin{bmatrix} \frac{\partial f}{\partial x'} \\ \frac{\partial f}{\partial y'} \end{bmatrix}$

7) **return**  $\nabla f$

## 2.3 Model Data

For the OSSE, velocity field data from the 3 km NAM model [31] is utilized. This velocity field was from the portion the model over southwestern Virginia and was centered at the Virginia Tech experimental site, Kentland Farm (figure 3.1), during a 215 hr period beginning Sept 4<sup>th</sup>, 2017 at 00:00 UTC. The NAM data was divided into 2 data sets. The first part was a strictly 2D data set that was restricted to the 850 mb isosurface. The second was a 3D data set. Both data sets were interpolated in time from 1 hr resolution down to 10 min resolution using cubic splines. The 3D data were then interpolated from pressure based vertical levels to height above sea level (ASL) vertical levels using linear interpolation. Both data sets were also interpolated from a 3 km horizontal resolution to a 300 m horizontal resolution using cubic Lagrange polynomials. An aircraft is simulated using closed-loop trajectory control to fly fixed-radius circles. These circles vary in radius from 2-15 km, smaller radii more consistent with the federal regulations in FAA part 107 [32] were examined, however the simulated wind velocity field lacked the spatial inhomogeneity necessary to compute meaningful gradients below a 2 km flight radius. The simulated aircraft was also set to track the 850 mb isosurface with the 3D wind velocity field acting as a disturbance. While the altitude of the 850 mb isosurface varies in time, it is approximately at 1545 m ASL. A subscale model of a transport-style aircraft, named the T-2 [33], was used as the simulated unmanned aircraft. To get a sense of the aircraft's scale, some of its physical properties are

$$\text{mass } m = 22.5 \text{ kg, wingspan } b = 2.09 \text{ m, chord } \bar{c} = 0.28 \text{ m, airspeed } \|\mathbf{u}\| \approx 42 \text{ m/s.}$$

With the T-2's cruising airspeed of approximately 42 m/s, a full orbit takes between 300 to 2250 seconds, depending on the orbit radius. For a comparison, the average horizontal windspeed of the NAM model at the 850mb isosurface was approximately 9.8 m/s. The

details of the flight dynamic model are included in Appendix . The simulated wind measurements taken by the aircraft are wind field components  $\mathbf{v}$  along the aircraft's center-of-mass trajectory  $\mathbf{x}(t)$ . Figure 3.5 shows several orbits during the aircraft's flight. Note that the vertical dimension is scaled to be 500 times bigger than the horizontal, in order to show flight path differences between consecutive orbits.

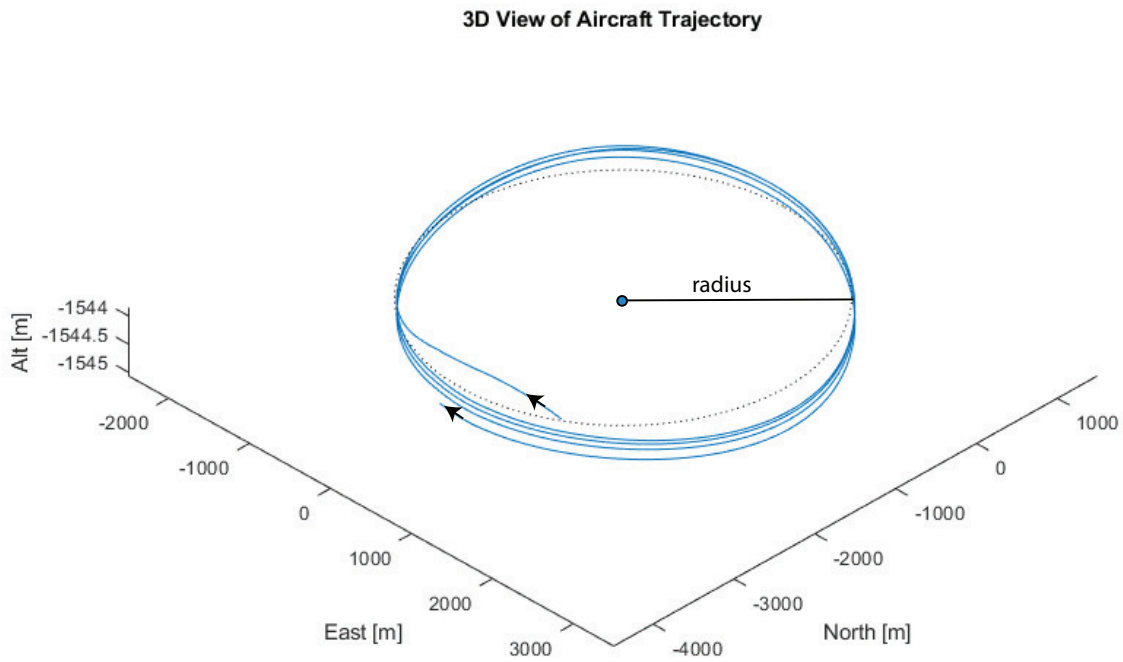


Figure 3.5: Simulated 3D UAS flight path (solid blue line) along with a 2D perfect circle (dotted black line). The 2D circle is at a constant altitude, while the 3D UAS flight tracks the 850mb isosurface. The vertical dimension is shown highly exaggerated.

	2 km circle	5 km circle	10 km circle	15 km circle	2 km flight	5 km flight	10 km flight	15 km flight
center point	0.955	0.854	0.790	0.730	0.931	0.827	0.781	0.730
2 km circle	--	0.946	0.815	0.751	0.981	0.923	0.811	0.765
5 km circle		--	0.866	0.768	0.935	0.981	0.865	0.784
10 km circle			--	0.928	0.804	0.836	0.974	0.902
15 km circle				--	0.745	0.738	0.904	0.955
2 km flight					--	0.944	0.824	0.783
5 km flight						--	0.870	0.793
10 km flight							--	0.937

Table 3.1: Pearson correlation coefficients for trajectory divergence rate,  $\dot{\rho}$ , measurements. Coefficients range from 0.730 to 0.965.

### 3 Results

#### 3.1 Approximating local Eulerian Metrics from UAS flights

This section presents results which indicate how well the attraction rate,  $s_1$ , and the trajectory divergence rate,  $\dot{\rho}$ , can be approximated from a UAS flight. Figure 3.6 shows the results for the trajectory divergence rate. From the 2D velocity field, restricted to the 850 mb isosurface, measurements along perfectly circular paths, with radii fixed between 2 km and 15 km, were used to approximate the trajectory divergence rate, shown in black. Then, velocity measurements from 3D simulated UAS flight paths with radii fixed between 2 km and 15 km, attempting to follow the 850 mb isosurface, were used to approximate the trajectory divergence rate, shown in blue. Finally, using the 850 mb isosurface velocity field, the true trajectory divergence rate at the center point of the circle/flight radius was calculated, shown in red. Pearson correlation coefficients for these measurements can be found in Table 3.1.

Figure 3.7 shows the results for the attraction rate. As before, using measurements along perfectly circular paths, with radii fixed between 2 km and 15 km, from a 2D velocity field restricted to the 850 mb isosurface, the attraction rate was approximated, shown in black. Then, the attraction rate was approximated using velocity measurements from a 3D

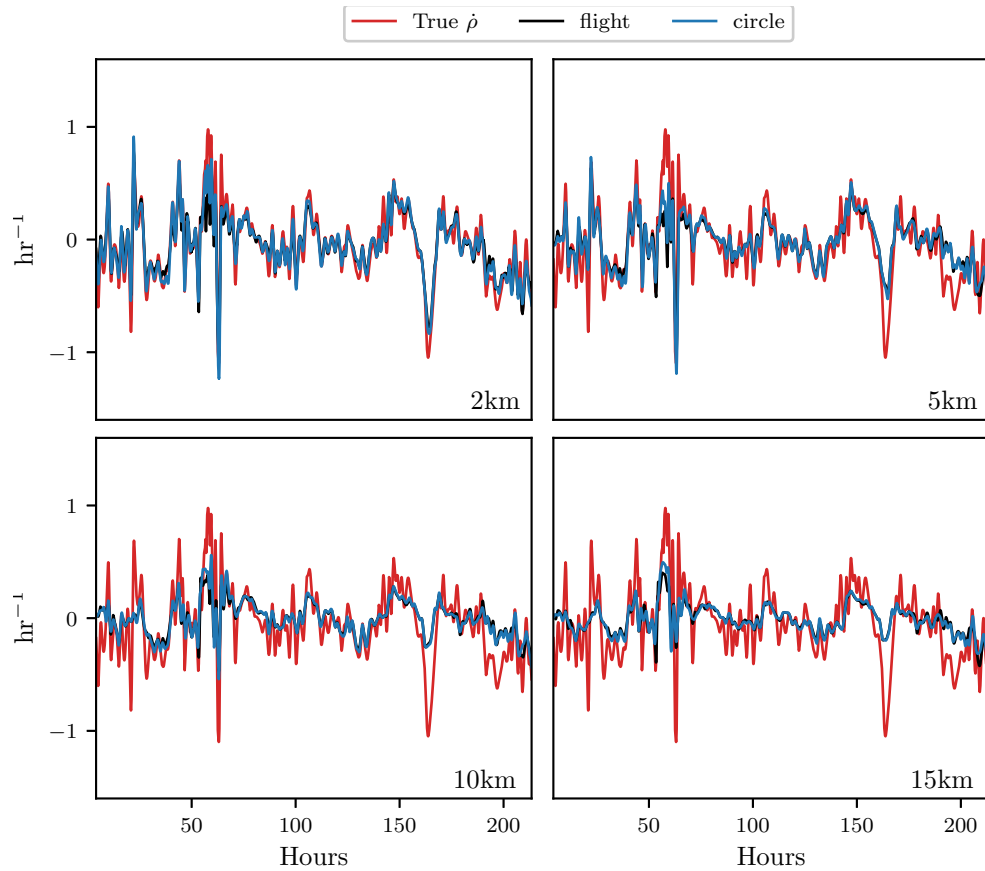


Figure 3.6: Comparison of measurements of the trajectory divergence rate  $\dot{\rho}$  at the center point of the circular sampling orbit (red), along the path of a simulated UAS flight (black), and along a circular arc (blue). The radius of the circle and flight path is shown in the lower right hand corner of each time series. The circular arc and the simulated UAS flight are nearly on top of each other.

simulated UAS flight paths, with radii fixed between 2 km and 15 km, attempting to follow the 850 mb isosurface, shown in blue. Finally, using the 850 mb isosurface velocity field the true attraction rate at the center point of the circle/flight radius was calculated, shown in red. Pearson correlation coefficients for these measurements can be found in Table 3.2.

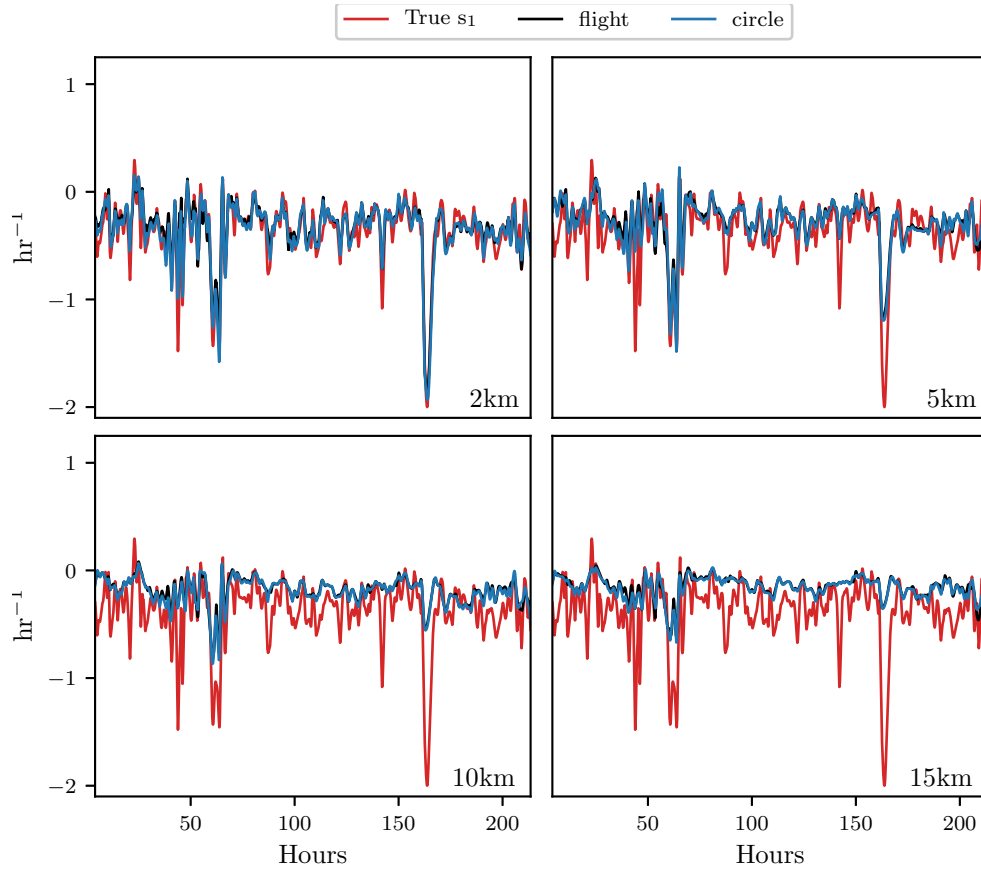


Figure 3.7: Comparison of measurements of the attraction rate  $s_1$  at the center point of the circular sampling orbit (red), along the path of a simulated UAS flight (black), and along a circular arc (blue). The radius of the circle and flight path is shown in the lower right hand corner of each time series. The circular arc and the simulated UAS flight are nearly on top of each other.

### 3.2 Using Eulerian Metrics to infer Lagrangian Dynamics

In this section, results which indicate how well the attraction rate,  $s_1$ , and the trajectory divergence rate,  $\dot{\rho}$ , predicts Lagrangian dynamics, such as the passage of LCSs are presented. Figure 3.8 shows the time series for the trajectory divergence rate and backward-time FTLE for integration times of 0.5, 1, and 2 hrs. Figure 3.9 shows the time series for the attraction rate and backward-time FTLE for integration times of 0.5, 1, and 2 hrs. The FTLE values have been multiplied by -1 for improved visualization. These values were calculated using

	2 km circle	5 km circle	10 km circle	15 km circle	2 km flight	5 km flight	10 km flight	15 km flight
center point	0.939	0.838	0.677	0.590	0.910	0.821	0.675	0.577
2 km circle	--	0.932	0.742	0.644	0.980	0.917	0.739	0.627
5 km circle		--	0.898	0.789	0.916	0.980	0.887	0.760
10 km circle			--	0.908	0.729	0.881	0.978	0.864
15 km circle				--	0.637	0.788	0.907	0.965
2 km flight					--	0.936	0.746	0.644
5 km flight						--	0.900	0.791
10 km flight							--	0.909

Table 3.2: Pearson correlation coefficients for attraction rate,  $s_1$ , measurements. Coefficients range from 0.577 to 0.939.

velocity data from the the 850 mb isosurface over the Kentland Farm portion of the NAM model.

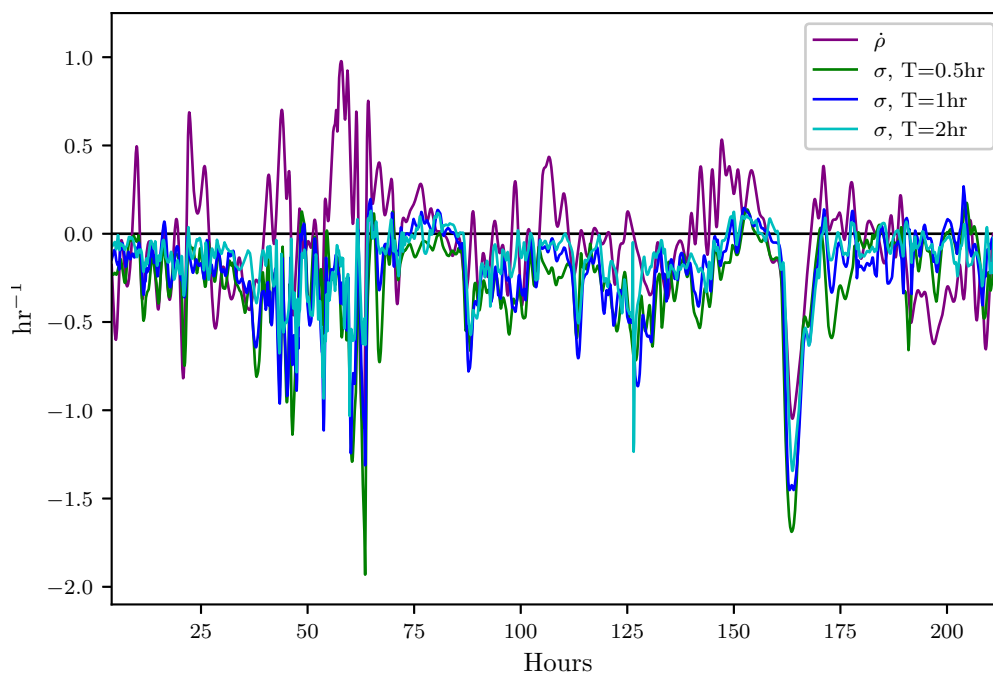


Figure 3.8: Comparison of the trajectory divergence rate with the 0.5, 1, and 2 hr backward-time FTLE from  $t=4$  to  $t=215$ hrs. FTLE fields have been multiplied by  $-1$  to offer better comparison of attraction.

The effectiveness of the attraction rate and the trajectory divergence rate for detecting LCSs was further explored using receiver operating characteristic (ROC) curves. ROC curves plots the true positive rate against the false positive rate for different threshold levels. Figure 3.11 shows an example of a true positive and a false positive from this study. To define these

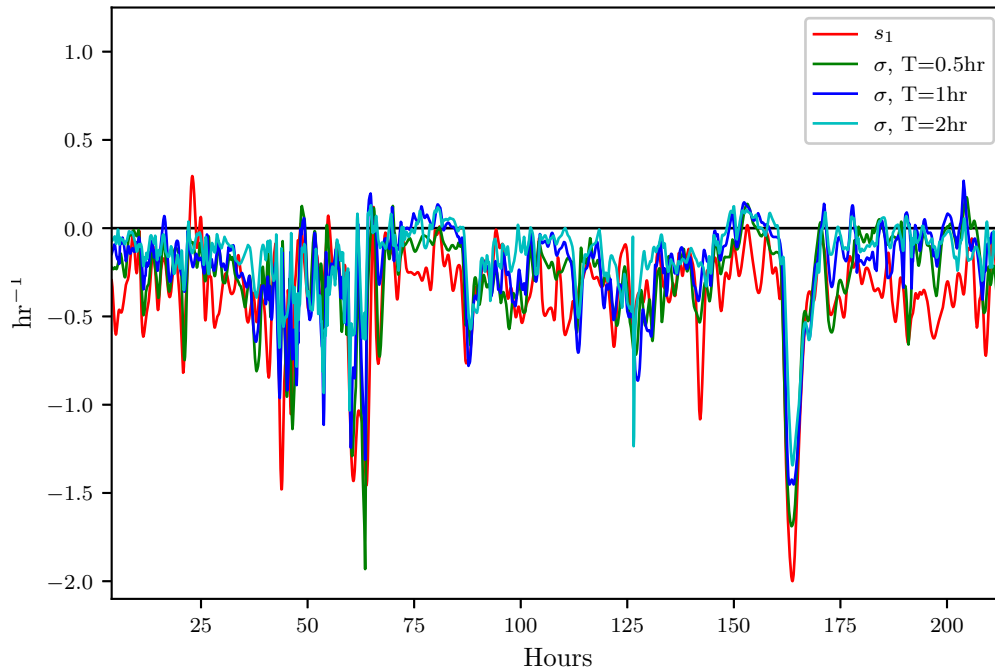


Figure 3.9: Comparison of the attraction rate with the 0.5, 1, and 2 hr backward-time FTLE from  $t=4$  to  $t=215$ hrs. FTLE fields have been multiplied by  $-1$  to offer better comparison of attraction.

curves, we determined when LCSs passed within a threshold radius which ranged from 400 m to 10 km of the center point, figure 3.10. We further applied a threshold of 90% for the LCSs, so only LCSs whose FTLE value was above the 90<sup>th</sup> percentile were considered. The attraction rate's and the trajectory divergence rate's ability to detect LCSs for integration times of 0.5, 1, and 2 hrs in backward-time was explored. Figure 3.12 shows an idealized ROC curve with different threshold values, the farther the ROC curve is from the dotted line the better the sensor is. This can be quantified using the area under the curve (AUC). The larger the AUC is above 0.5, the better the sensor is; a perfect sensor would have an AUC of 1.

Figure 3.13 shows ROC curves for the the trajectory divergence rate as measured from the center point of the sampling area (figure 3.10). The threshold ranges from 0% at the upper right hand corner to 100% at the lower left hand corner. Every 20<sup>th</sup> percentile is marked

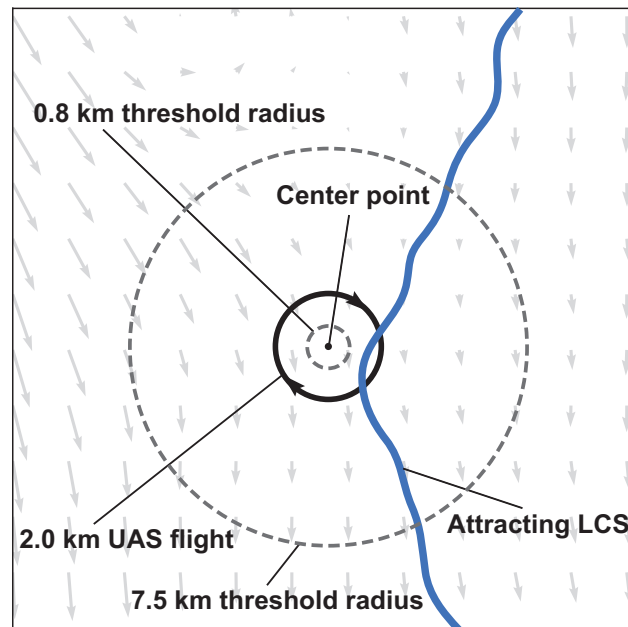


Figure 3.10: Schematic of LCS detection showing two examples of threshold radii as dashed lines. An attracting LCS falls within the larger threshold radius but does not fall within the smaller radius. The instantaneous wind field is depicted as the background vector field.

with a dot. Each subplot represents a different threshold radius, with radii ranging from 400 m to 10 km. Each color represents a different integration time for the LCSs, 0.5 hr green, 1 hr red, 2 hr blue. The AUC ranges from 0.477 to 0.756.

Figure 3.14 shows ROC curves for the attraction rate as measured from the center point of the sampling area (figure 3.10). As before, the threshold is applied to the attraction rate ranging from 0%, upper right hand corner, to 100%, lower left hand corner. Every 20<sup>th</sup> percentile is marked with a dot. Each subplot represents a different threshold radius, with radii ranging from 400 m to 10 km. Each color represents a different integration time for the LCSs, 0.5 hr green, 1 hr red, 2 hr blue. The AUC ranges from 0.626 to 0.850.

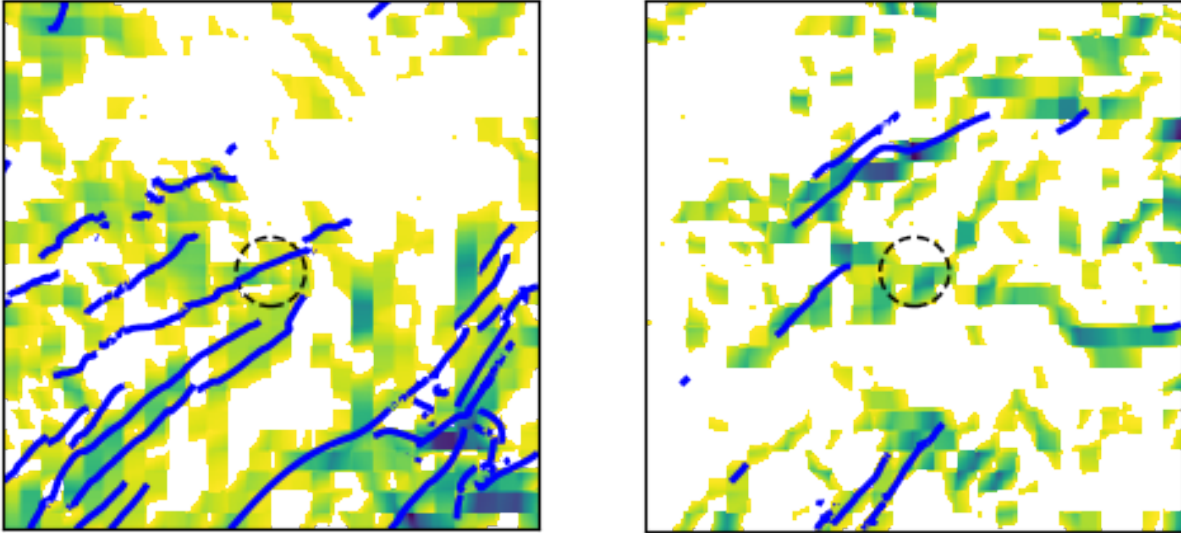


Figure 3.11: Depiction of a true positive (left) and a false positive (right), from approximately 43.5 hrs and 20.67 hrs respectively. The true attraction rate field over Kentland Farm Va. is displayed, darker greens are lower values of the attraction rate. Grid points where the value of the attraction rate is above the threshold value are masked (white). Attracting LCS with an integration time of -1 hr are shown as blue lines. The threshold radius is shown by the black dashed circle and has a radius of 5 km. In both examples the attraction rate at the center of the sampling domain is below the threshold value, thus meeting the criterion for a positive identification of an LCS passing within the threshold radius. In the true positive example there is an LCS passing within the threshold radius. Meanwhile, in the false positive there is no LCS within the threshold radius. The ROC plot point for the particular case shown in this figure (i.e. threshold value and radius) is depicted by a red “+” marker in figure 3.14.

### 3.3 Inferring Lagrangian Dynamics from UAS measurements

This section presents results which indicate how well the attraction rate,  $s_1$ , and the trajectory divergence rate,  $\dot{\rho}$ , as approximated from a UAS flight predicts Lagrangian dynamics, such as the passage of LCSs, figure 3.10. Figure 3.15 shows ROC curves for the trajectory divergence rate as calculated from a simulated 2 km radius UAS flight. The threshold ranges from 0% at the upper right hand corner to 100% at the lower left hand corner. Every 20<sup>th</sup> percentile is marked with a dot. Each subplot represents a different threshold radius,

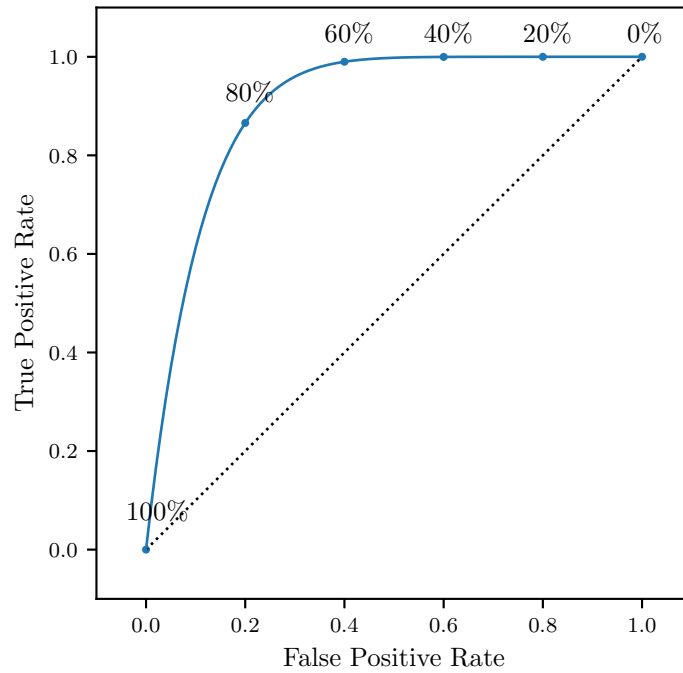


Figure 3.12: Schematic of an idealized ROC curve and with threshold percentiles.

with radii ranging from 400 m to 10 km. Each color represents a different integration time for the LCSs, 0.5 hr green, 1 hr red, 2 hr blue. The AUC ranges from 0.491 to 0.742.

Figure 3.16 shows ROC curves for the attraction rate as calculated from a simulated 2 km UAS flight. As before, the threshold is applied to the attraction rate ranging from 0%, upper right hand corner, to 100%, lower left hand corner. Every 20<sup>th</sup> percentile is marked with a dot. Each subplot represents a different threshold radius, with radii ranging from 400 m to 10 km. Each color represents a different integration time for the LCSs, 0.5 hr green, 1 hr red, 2 hr blue. The AUC ranges from 0.602 to 0.874.

## 4 Discussion

Looking at the results in figure 3.6, we can see that the simulated UAS flight in 3D space provides a very similar result to the circular path restricted to the 850 mb isosurface. For

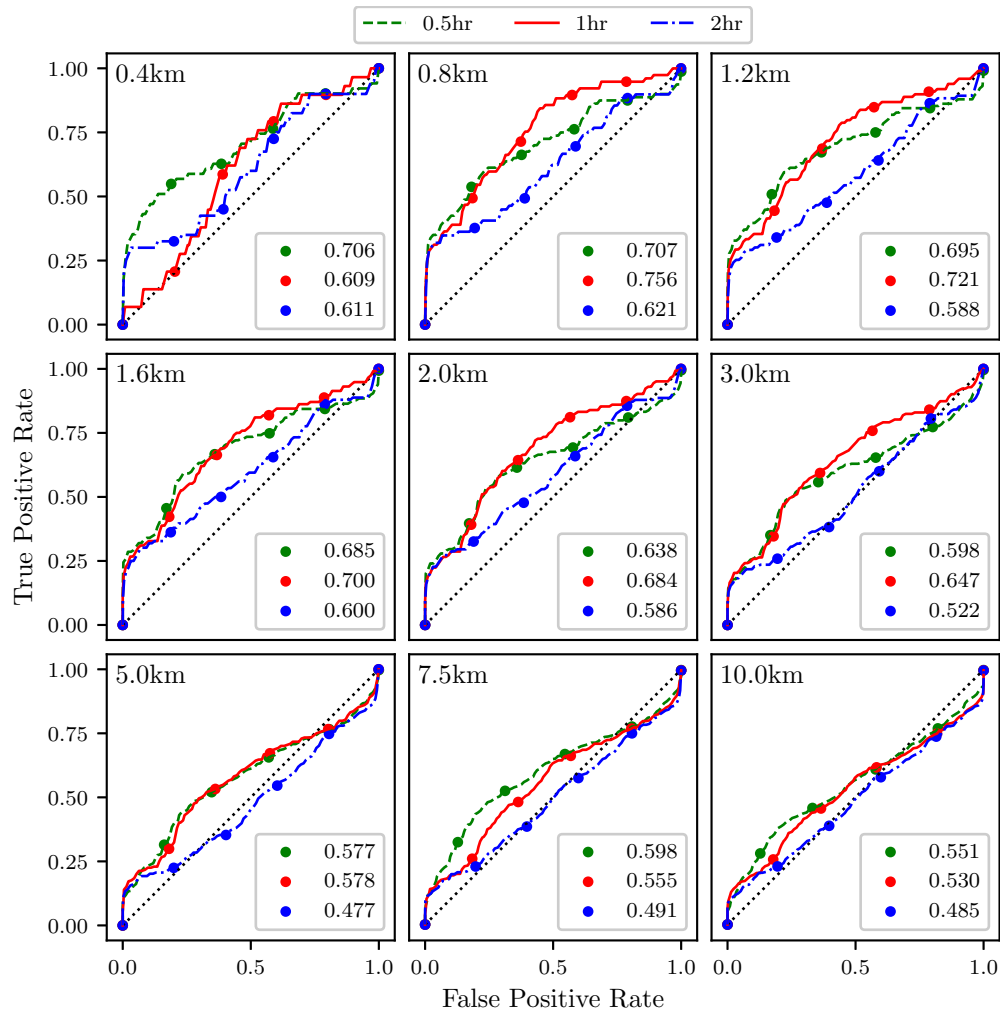


Figure 3.13: ROC curves for the trajectory divergence rate,  $\dot{\rho}$ , as measured at the center point ability to detect 90<sup>th</sup> percentile LCSs with integration times of 0.5 (green), 1 (red), and 2 (blue) hrs. Threshold radii are displayed in the upper left hand corner. The AUC for each integration time is given in the legend.

all the radii that were analyzed, the trajectory divergence rate from the flight simulation is nearly identical to that from the 2D circular path. Most of the error between the center point trajectory divergence rate and the estimate from the 3D flights appears to be due to the distance from the point of estimation, rather than inconsistencies in the flights path due to the UAS being buffeted by wind. This can also be seen in Table 3.1, where the correlation coefficients between the simulated flight and the 2D circle are all  $> 0.95$ , while there is a

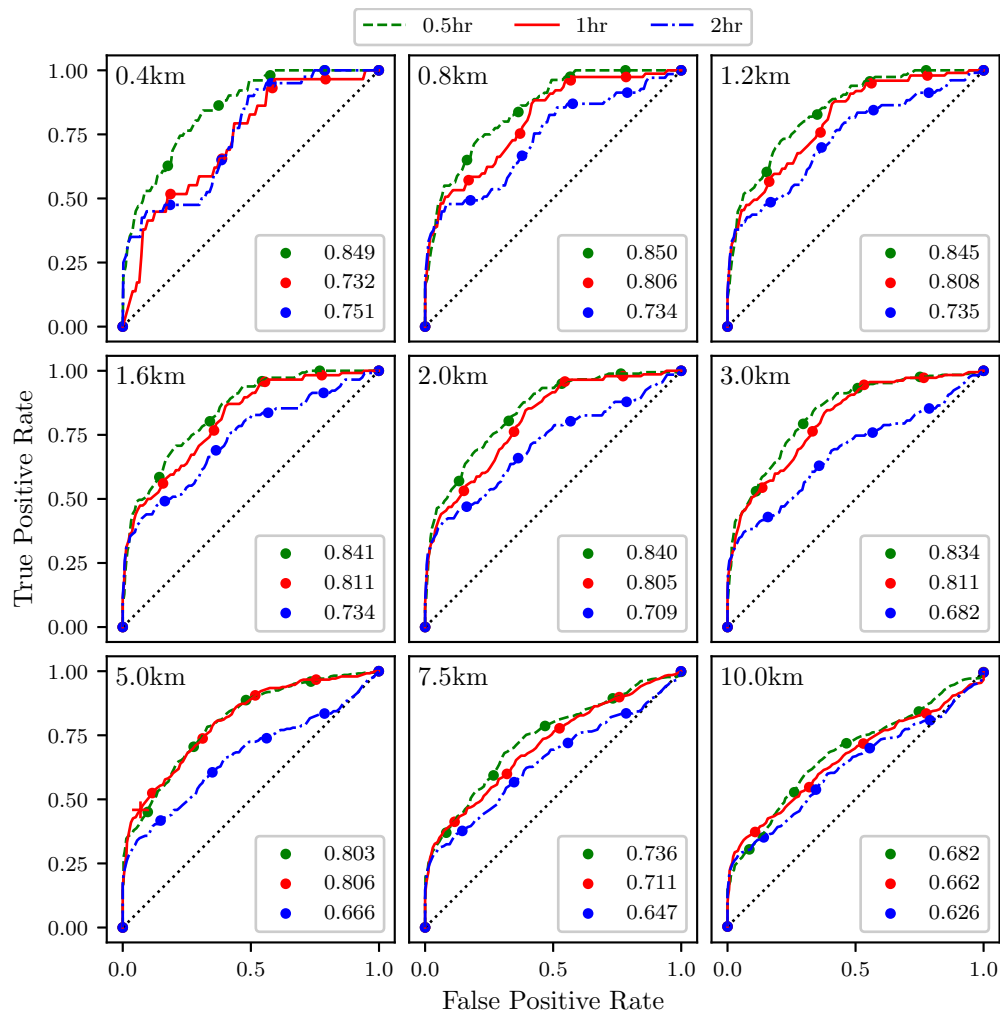


Figure 3.14: ROC curves for the attraction rate,  $s_1$ , as measured at the center point ability to detect 90<sup>th</sup> percentile LCSs with integration times of 0.5 (green), 1 (red), and 2 (blue) hrs. Threshold radii are displayed in the upper left hand corner. The AUC for each integration time is given in the legend. The red “+” marker corresponds to the plot point for the case (i.e. threshold value and radius) that was shown in figure 3.11.

steady drop in the correlation coefficients with the center point trajectory divergence rate as the radius increases.

Looking at the results in figure 3.7, we see that the simulated UAS flight in 3D space provides very similar attraction rate measurements to the circular path restricted to the 850 mb isosurface. As before, for all the radii paths that were examined, the attraction rate from

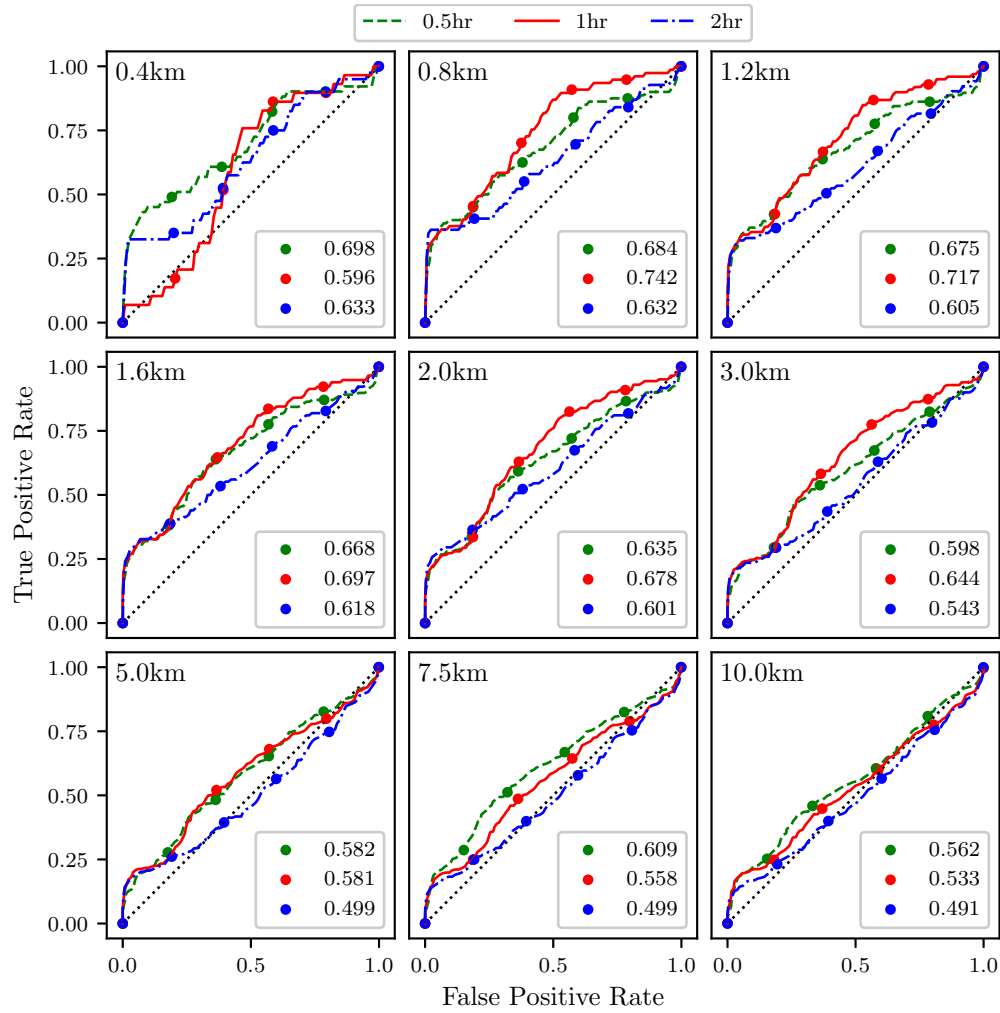


Figure 3.15: ROC curves for the trajectory divergence rate,  $\dot{\rho}$ , as measured from a 2 km radius UAS simulation ability to detect 90<sup>th</sup> percentile LCSs with integration times of 0.5 (green), 1 (red), and 2 (blue) hrs. Threshold radii are displayed in the upper left hand corner. The AUC for each integration time is given in the legend.

the flight simulation is nearly identical to that from the 2D circular path. Most of the error between the center point attraction rate and the estimate from the 3D flights appears to be due to the distance from the point of estimation, rather than inconsistencies in the flights path due to the UAS being buffeted by wind. This can also be seen in Table 3.2, where the correlation coefficients between the simulated flight and the 2D circle are all  $> 0.96$ , while there is a steep drop in the correlation coefficients with the center point attraction rate as

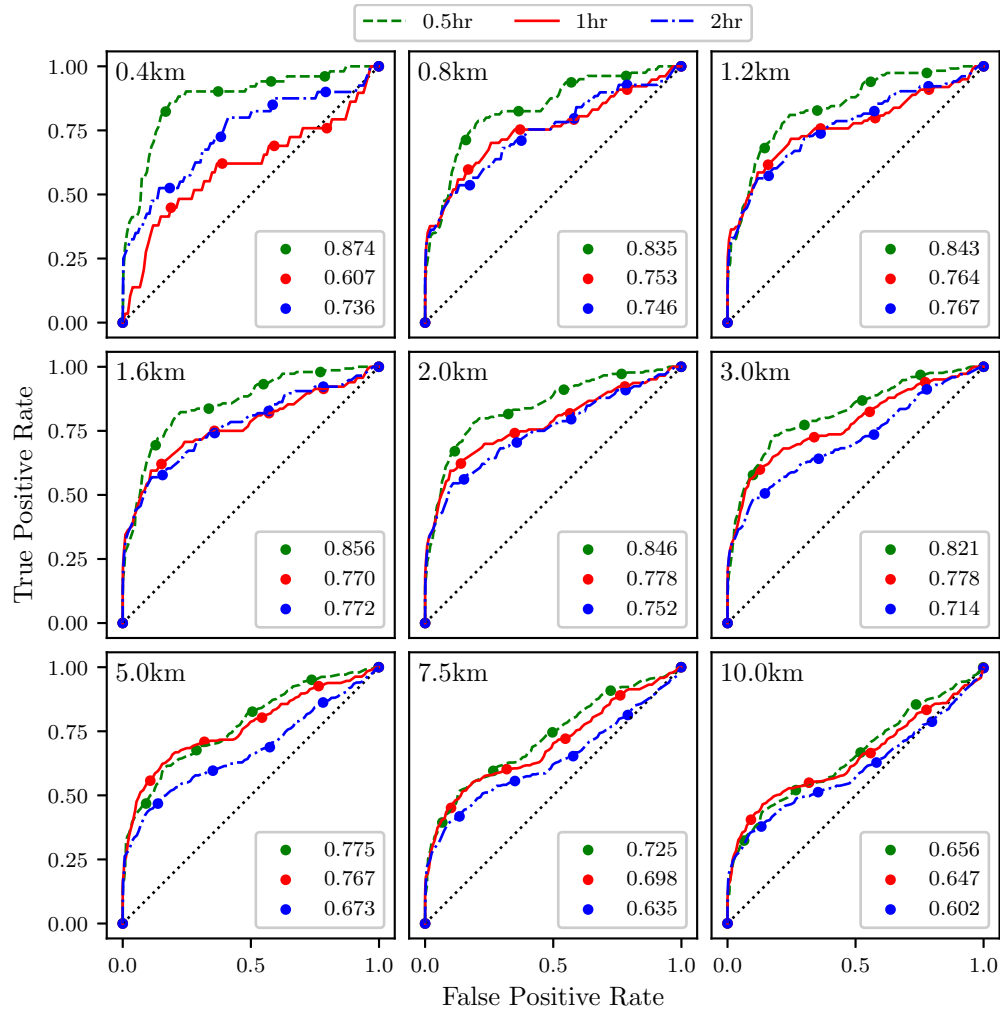


Figure 3.16: ROC curves for the attraction rate,  $s_1$ , as measured from a 2 km radius UAS simulation ability to detect 90<sup>th</sup> percentile LCSs with integration times of 0.5 (green), 1 (red), and 2 (blue) hrs. Threshold radii are displayed in the upper left hand corner. The AUC for each integration time is given in the legend.

the radius increases.

Both the attraction rate and the trajectory divergence rate at a point can be approximated to a high degree of accuracy by UAS flights. Simulated 3D UAS flights provided measurements which were nearly identical to those of perfect circular 2D paths. The main cause of error in the approximations appears to be the radius of the circular arc. Furthermore, the trajectory divergence rate appears to be a more robust metric than the attraction rate; meaning that the

trajectory divergence rate can be better approximated at larger radii than the attraction rate can. This can be seen very clearly in Tables 3.1 and 3.2, where the correlation coefficient for the attraction rate drops off more quickly with flight radius than for the trajectory divergence rate.

As mentioned previously, the smallest flight radius which was explored in this study was 2 km. This radius was chosen because under 2 km the spatial inhomogeneity of the simulated velocity field was insufficient to compute meaningful gradients. However, under current federal regulations in FAA part 107, unaided visual contact must be maintained with the UAS [32]. For smaller UASs, it is unlikely that an operator would be able to satisfy this requirement at a flight radius of 2 km. Fortunately, these results suggest that as the flight radius is decreased the UAS approximation of the Eulerian diagnostic will converge the true value at the center point. Thus, we anticipate that in real-world experiments, where the flight radius will be  $\mathcal{O}(100\text{ m})$ , a single fixed-wing UAS will provide a very accurate approximation to the Eulerian diagnostics at the center point.

Figure 3.8 shows that the trajectory divergence rate does not always follow the trend of the negative backward-time FTLE. This is to be expected, as the trajectory divergence rate gives information on both instantaneous attraction and repulsion, while the negative backward-time FTLE gives only a measure of attraction. The trajectory divergence rate does, however, agree with the negative backward-time FTLE during periods of significant (large) attraction. This behavior is of particular interest for the detection of LCSs. When calculating LCSs, there is often a multitude of weaker, less important LCSs. In order to filter out these less important structures and focus on important structures, one often needs to set a threshold value for the FTLE field. These dips in the the trajectory divergence rate, coinciding with the strongest dips in the negative backward-time FTLE, would therefore seem to be a likely indicator of the most influential LCS.

Figure 3.9 shows that the attraction rate follows the general trend of the negative backward-time FTLE. This is consistent as both the attraction rate and the negative backward-time FTLE give measures of attraction. The attraction rate appears to give a good approximation to the negative backward-time FTLE, and thus should be able to give indications of LCSs.

The ROC curves in figure 3.13 show that the trajectory divergence rate, calculated at a point, can be used to detect the passage of LCSs. For the smaller threshold radii, AUC values for the ROC curves of greater than 0.6 are consistently seen. This means that this method is outperforming random guessing, which would have an AUC of 0.5. Of course as the threshold radius increases the AUC trends to 0.5. This convergence to random chance at larger thresholds is consistent, since as the sample area increases, the likelihood of an LCS being within that domain will converge to 100%, at least for realistic atmospheric flows.

The ROC curves in figure 3.14 show that the attraction rate, calculated at a point, cannot only be used to detect the passage of LCSs, but that it performs better at LCS detection than the trajectory divergence rate does. The smaller and more moderate threshold radii consistently display AUC values for the ROC curves of greater than 0.7, and many well over 0.8. This means that this method is far outperforming random guessing. Once again, it can be seen that as the threshold radius increases the AUC trends towards 0.5, although this convergence is happening slower than it did with the trajectory divergence rate.

It should be noted that both the attraction and trajectory divergence rates seem to perform best at a threshold radius of around 800-2000 m and become noisier as the radius decreases. We suspect that this is due to the spatial and temporal scales of the input data, 3 km x 1 hr grid spacing. We speculate that with a velocity field that is either analytically defined or more highly resolved in both space and time, continued improvement in the ROC curves as the threshold radius decreases would be seen. Unfortunately, higher resolution model data was unavailable for this study and the analytical models currently used in the study of LCSs

in 2D, such as the double gyre [34] and the Bickley jet [35], do not have the requisite spatial inhomogeneity necessary to reveal meaningful Eulerian structures in the attraction rate or the trajectory divergence rate fields.

The ROC curves in figure 3.15 show that the trajectory divergence rate, as calculated from a simulated 2 km UAS flight, can be used to detect the passage of LCSs. For the smaller, and even more moderate, threshold radii, AUC values for the ROC curves of greater than 0.6 are consistently seen. This means that this method is outperforming random guessing. Of course as the threshold radius increases the AUC trends to 0.5.

The ROC curves in figure 3.16 show that the attraction rate, as calculated from a simulated 2 km UAS flight, cannot only be used to detect the passage of LCSs, but once again performs better at LCS detection than the trajectory divergence rate does. For the smaller and more moderate threshold radii consistently display AUC values for the ROC curves of greater than 0.7, and many well over 0.8. This means that this method is outperforming random guessing. Once again, as the threshold radius increases the AUC trends towards 0.5, although this convergence is happening slower than it did with the trajectory divergence rate.

## 5 Conclusions

We have put forward a novel algorithm to approximate the gradient of a scalar field using measurements from a circular arc around a point. Using realistic atmospheric velocity data from the NAM 3 km model, this algorithm was applied to circular trajectories restricted to a 2D isosurface and simulated UAS flights in 3D, with radii ranging from 2 km to 15 km. From these results the trajectory divergence rate and the attraction rate was approximated for the center point of these paths. Comparing these approximations with the true trajectory divergence rate and attraction rate at the center point, we found that both the

realistic flight simulator and the circle give nearly identical approximations. Furthermore, the approximations were very good for the smaller radii that were looked at, but even the larger radii approximations were able to pick up the trend of the trajectory divergence rate and attraction rate, though they underestimated the magnitude.

We have also examined the ability of Eulerian diagnostics, in particular the trajectory divergence and attraction rates, to infer Lagrangian dynamics. Using ROC curves, the ability of the trajectory divergence rate and attraction rate, as calculated at a point, to detect the passage of LCSs within a threshold radius was explored. We found that the attraction rate can be used as an effective tool to detect short term LCSs passing by. We also found that the trajectory divergence rate, while performing better than chance, underperformed the attraction rate. This analysis was then extended to look at the trajectory divergence rate and attraction rate as approximated by a UAS flight. Once again we found that these Eulerian diagnostics, as approximated by a UAS flight, can be an effective tool for detecting LCSs passing through a sampling area.

This manuscript serves as a first step towards in-situ detection of LCSs in the atmosphere. It demonstrates that a single fixed-wing UAS can, in principle, be used to measure Eulerian diagnostics of a local atmospheric flow. These Eulerian diagnostics can then be used to infer the Lagrangian dynamics of the local flow. Future work will apply this manuscript's techniques to experimental data to detect real-world atmospheric LCSs using a fixed-wing UAS, evaluate the effects of sensor uncertainty on the accuracy of LCS detection, and extend the analysis to the detection of pollutant specific LCSs [5, 12, 36].

**Funding:** his research was supported in part by grants from the National Science Foundation (NSF) under grant numbers AGS 1520825 (Hazards SEES: Advanced Lagrangian Methods for Prediction, Mitigation and Response to Environmental Flow Hazards) and

DMS 1821145 (Data-Driven Computation of Lagrangian Transport Structure in Realistic Flows) and the National Aeronautics and Space Administration (NASA) under grant number 80NSSC17K0375 (NASA Earth and Space Science Fellowship). Any opinions, findings, and conclusions or recommendations expressed in this material are those of the authors and do not necessarily reflect the views of the sponsors.

**Acknowledgments:** We thank Javier González-Rocha, Gary K. Nave, and David G. Schmale III for fruitful discussions during the writing of this manuscript.

**Conflicts of interest:** The authors declare no conflict of interest.

**Abbreviations:** The following abbreviations are used in this manuscript,

UAS	unmanned aircraft systems
ASL	Above sea level
AUC	area under the curve
FTLE	Finite-time Lyapunov exponent
LCS	Lagrangian coherent structure
iLCS	infinitesimal-time LCS
OECS	Objective Eulerian coherent structure
WRF	Weather research and forecasting
NAM	North American Mesoscale model
OSSE	Observing System Simulation Experiment

## Appendix B

The aircraft flight dynamic model is derived by combining standard aircraft rigid-body equations [37] with Grauer and Morelli's Generic Global Aerodynamic model [33], modified for

non-uniform wind. The important flight dynamic modeling assumptions are:

1. Earth is a flat, inertial reference.
2. The aircraft is a rigid body, symmetric about its longitudinal plane, with constant mass  $m$ .
3. For wind-aircraft interaction, the aircraft is a point “located” at it’s center-of-mass.
4. The wind is described by a  $C^1$ -smooth kinematic vector field.
5. Aircraft thrust  $f_{th}$  is an instantaneously-controllable force acting nose-forward from the center-of-mass.
6. All parameters are invariant with altitude. (e.g. no altitudinal variation of density  $\rho$ , gravity  $g$ , ground-effect, etc.)

The resulting dynamic equations of motion are

$$\mathbf{R}_{BM}(\alpha) \begin{pmatrix} C_D(\dots) \\ C_Y(\dots) \\ C_L(\dots) \end{pmatrix} \frac{1}{2} \rho \|\mathbf{V}_r\|^2 S + \begin{pmatrix} f_{th} \% \left( \frac{f_{th} \text{ max}}{100\%} \right) \\ 0 \\ 0 \end{pmatrix} + \mathbf{R}_{EB}^T(\Theta) \begin{pmatrix} 0 \\ 0 \\ mg \end{pmatrix} = m \left( \dot{\mathbf{V}} + (\boldsymbol{\omega} \times \mathbf{V}) \right), \quad (3.10)$$

$$\begin{bmatrix} b & 0 & 0 \\ 0 & \bar{c} & 0 \\ 0 & 0 & b \end{bmatrix} \begin{pmatrix} C_l(\dots) \\ C_m(\dots) \\ C_n(\dots) \end{pmatrix} \frac{1}{2} \rho \|\mathbf{V}_r\|^2 S = \begin{bmatrix} I_{xx} & 0 & -I_{xz} \\ 0 & I_{yy} & 0 \\ -I_{xz} & 0 & I_{zz} \end{bmatrix} \dot{\boldsymbol{\omega}} + \left( \boldsymbol{\omega} \times \begin{bmatrix} I_{xx} & 0 & -I_{xz} \\ 0 & I_{yy} & 0 \\ -I_{xz} & 0 & I_{zz} \end{bmatrix} \boldsymbol{\omega} \right). \quad (3.11)$$

where the ellipses on the aerodynamic coefficients remind the reader that these are functions of state variables, as given below in Equations 3.14 – 3.19. The symbol  $\mathbf{V}$  is used for

inertially-referenced velocity, and  $\mathbf{V}_r$  is used for air-relative velocity. The notation  $\mathbf{R}_{BM}(\alpha)$  represents the rotation matrix, which depends on of angle-of-attack  $\alpha$ , from the aircraft's body-frame to the modified-stability frame in which Grauer and Morelli's aerodynamic forces are defined. Similarly,  $\mathbf{R}_{EB}(\Theta)$  is the rotation matrix from the Earth frame to the aircraft's body frame. The rest of the notation is in agreement with Etkin [37]. These dynamics are combined with standard translational and rotational kinematic equations

$$\dot{\mathbf{X}} = \mathbf{R}_{EB}(\phi, \theta, \psi) \begin{pmatrix} u \\ v \\ w \end{pmatrix} = \mathbf{R}_{EB}(\Theta) \mathbf{V}, \quad (3.12)$$

$$\dot{\Theta} = \begin{pmatrix} \dot{\phi} \\ \dot{\theta} \\ \dot{\psi} \end{pmatrix} = \begin{bmatrix} 1 & \sin \phi \tan \theta & \cos \phi \tan \theta \\ 0 & \cos \phi & -\sin \phi \\ 0 & \sin \phi \sec \theta & \cos \phi \sec \theta \end{bmatrix} \begin{pmatrix} p \\ q \\ r \end{pmatrix} = \mathbf{L}^{-1}(\phi, \theta) \boldsymbol{\omega}. \quad (3.13)$$

The aerodynamic coefficient expressions are from Equation 20 of Grauer and Morelli [33]

$$C_D = \theta_1 + \theta_2 \alpha + \theta_3 \alpha \tilde{q}_r + \theta_4 \alpha \delta_e + \theta_5 \alpha^2 + \theta_6 \alpha^2 \tilde{q}_r + \theta_7 \alpha^2 \delta_e + \theta_8 \alpha^3 + \theta_9 \alpha^3 \tilde{q}_r + \theta_{10} \alpha^4, \quad (3.14)$$

$$C_Y = \theta_{11} \beta + \theta_{12} \tilde{p}_r + \theta_{13} \tilde{r}_r + \theta_{14} \delta_a + \theta_{14} \delta_r, \quad (3.15)$$

$$C_L = \theta_{16} + \theta_{17} \alpha + \theta_{18} \tilde{q}_r + \theta_{19} \delta_e + \theta_{20} \alpha \tilde{q}_r + \theta_{21} \alpha^2 + \theta_{22} \alpha^3 + \theta_{23} \alpha^4, \quad (3.16)$$

$$C_l = \theta_{24} \beta + \theta_{25} \tilde{p}_r + \theta_{26} \tilde{r}_r + \theta_{27} \delta_a + \theta_{28} \delta_r, \quad (3.17)$$

$$C_m = \theta_{29} + \theta_{30} \alpha + \theta_{31} \tilde{q}_r + \theta_{32} \delta_e + \theta_{33} \alpha \tilde{q}_r + \theta_{34} \alpha^2 \tilde{q}_r + \theta_{35} \alpha^2 \delta_e + \theta_{36} \alpha^3 \tilde{q}_r + \theta_{37} \alpha^3 \delta_e + \theta_{38} \alpha^4, \quad (3.18)$$

$$C_n = \theta_{39} \beta + \theta_{40} \tilde{p}_r + \theta_{41} \tilde{r}_r + \theta_{42} \delta_a + \theta_{43} \delta_r + \theta_{44} \beta^2 + \theta_{45} \beta^3. \quad (3.19)$$

In these equations  $(\theta_1, \theta_2, \dots, \theta_{45})$  are the aircraft parameters,  $(\alpha, \beta)$  are the standard aerodynamic angles,  $(\tilde{p}_r, \tilde{q}_r, \tilde{r}_r)$  are wind-relative non-dimensionalized angular rates, and  $(\delta_a, \delta_e, \delta_r)$

are aileron, elevator, and rudder deflections.

# Bibliography

- [1] Phanindra Tallapragada, Shane D Ross, and David G Schmale III. Lagrangian coherent structures are associated with fluctuations in airborne microbial populations. *Chaos*, 21:033122, 2011.
- [2] David G Schmale III and Shane D Ross. Highways in the sky: Scales of atmospheric transport of plant pathogens. *Annual Review of Phytopathology*, 53:591–611, 2015.
- [3] David G Schmale III and Shane D Ross. High-flying microbes: Aerial drones and chaos theory help researchers explore the many ways that microorganisms spread havoc around the world. *Scientific American*, February:32–37, 2017.
- [4] Amir E BozorgMagham, Shane D Ross, and David G Schmale III. Local finite-time Lyapunov exponent, local sampling and probabilistic source and destination regions. *Nonlinear Processes in Geophysics*, 22(6):663–677, 2015.
- [5] Jifeng Peng and Rorik Peterson. Attracting structures in volcanic ash transport. *Atmospheric environment*, 48:230–239, 2012.
- [6] Wenbo Tang, Pak Wai Chan, and George Haller. Lagrangian coherent structure analysis of terminal winds detected by LiDAR. Part I: Turbulence structures. *Journal of Applied Meteorology and Climatology*, 50(2):325–338, 2011.

- [7] Marilena Kampa and Elias Castanas. Human health effects of air pollution. *Environmental pollution*, 151(2):362–367, 2008.
- [8] C Arden Pope III, Richard T Burnett, Michael J Thun, Eugenia E Calle, Daniel Krewski, Kazuhiko Ito, and George D Thurston. Lung cancer, cardiopulmonary mortality, and long-term exposure to fine particulate air pollution. *JAMA*, 287(9):1132–1141, 2002.
- [9] Amir E BozorgMagham and Shane D Ross. Atmospheric Lagrangian coherent structures considering unresolved turbulence and forecast uncertainty. *Communications in Nonlinear Science and Numerical Simulation*, 22(1):964–979, 2015.
- [10] Carmine Senatore and Shane D Ross. Detection and characterization of transport barriers in complex flows via ridge extraction of the finite time Lyapunov exponent field. *International Journal for Numerical Methods in Engineering*, 86(9):1163–1174, 2011.
- [11] Jezabel Curbelo, Víctor José García-Garrido, Carlos Roberto Mechoso, Ana Maria Mancho, Stephen Wiggins, and Coumba Niang. Insights into the three-dimensional Lagrangian geometry of the antarctic polar vortex. *Nonlinear Processes in Geophysics*, 24(3):379, 2017.
- [12] Daniel Garaboa-Paz, Jorge Eiras-Barca, Florian Huhn, and Vicente Pérez-Muñuzuri. Lagrangian coherent structures along atmospheric rivers. *Chaos: An Interdisciplinary Journal of Nonlinear Science*, 25(6):063105, 2015.
- [13] Brent Knutson, Wenbo Tang, and Pak Wai Chan. Lagrangian coherent structure analysis of terminal winds: Three-dimensionality, intramodel variations, and flight analyses. *Advances in Meteorology*, 2015, 2015.
- [14] Javier González-Rocha, Craig A Woolsey, Cornel Sultan, and Stephan F J De Wekker.

- Sensing wind from quadrotor motion. *Journal of Guidance, Control, and Dynamics*, 2018. DOI: 10.2514/1.G003542.
- [15] Peter J Nolan, James Pinto, Javier González-Rocha, Anders Jensen, Christina Vezzi, Sean Bailey, Gijs de Boer, Constantin Diehl, Roger Laurence, Craig Powers, Hosein Foroutan, Shane D Ross, and David G Schmale III. Coordinated unmanned aircraft system (UAS) and ground-based weather measurements to predict Lagrangian coherent structures (LCSs). *Sensors*, 18(12):4448, 2018.
- [16] Mattia Serra and George Haller. Objective Eulerian coherent structures. *Chaos: An Interdisciplinary Journal of Nonlinear Science*, 26(5):053110, 2016.
- [17] Gary K Nave Jr, Peter J Nolan, and Shane D Ross. Trajectory-free approximation of phase space structures using the trajectory divergence rate. *Nonlinear Dynamics*, 2019.
- [18] D N Axford. On the accuracy of wind measurements using an inertial platform in an aircraft, and an example of a measurement of the vertical mesostructure of the atmosphere. *Journal of Applied Meteorology and Climatology*, 7:645–666, August 1968.
- [19] Donald H Lenschow and P Spyers-Duran. Measurement techniques: Air motion sensing. Technical Report 23, National Center for Atmospheric Research, Boulder, CO, USA, 1989.
- [20] NASA. Airborne science program website. <https://airbornescience.nasa.gov/>, 2017. accessed Jan 2017.
- [21] Jack Elston, Brian Argrow, Maciej Stachura, Doug Weibel, Dale Lawrence, and David Pope. Overview of small fixed-wing unmanned aircraft for meteorological sampling. *Journal of Atmospheric and Oceanic Technology*, 32(1):97–115, 2015.

- [22] Kasper T Borup, Thor I Fossen, and Tor A Johansen. A nonlinear model-based wind velocity observer for unmanned aerial vehicles. *IFAC-PapersOnLine*, 49(18):276–283, 2016. doi: 10.1016/j.ifacol.2016.10.177. 10th IFAC Symposium on Nonlinear Control Systems.
- [23] Matthew B Rhudy, Yu Gu, Jason N Gross, and Haiyang Chao. Onboard wind velocity estimation comparison for unmanned aircraft systems. *IEEE Transactions on Aerospace and Electronic Systems*, 53(1):55–66, February 2017.
- [24] F Adhika Pradipta Lie and Demoz Gebre-Egziabher. Synthetic air data system. *Journal of Aircraft*, 50(4):1234–1249, July 2013.
- [25] Jack W Langelaan, Nicholas Alley, and James Neidhoefer. Wind field estimation for small unmanned aerial vehicles. *Journal of Guidance, Control, and Dynamics*, 34(4):1016–1030, 2011. doi: 10.2514/1.52532.
- [26] Brandon M Witte, Robert F Singler, and Sean C C Bailey. Development of an unmanned aerial vehicle for the measurement of turbulence in the atmospheric boundary layer. *Atmosphere*, 8(10):195, 2017. doi: 10.3390/atmos8100195.
- [27] Andreas Wenz and Tor Arne Johansen. Estimation of wind velocities and aerodynamic coefficients for UAVs using standard autopilot sensors and a moving horizon estimator. In *International Conference on Unmanned Aircraft Systems (ICUAS)*, pages 1267–1276, Miami, FL, USA, June 2017. IEEE. doi: 10.1016/j.measurement.2018.01.027.
- [28] Ronald Peikert, Benjamin Schindler, and Robert Carnecky. Ridge surface methods for the visualization of Lagrangian coherent structures. In *Proceedings of the Ninth International Conference on Flow Dynamics, Sendai, Japan*, pages 206–207, 2012.

- [29] Peter J Nolan and Shane D Ross. Finite-time Lyapunov exponent field in the infinitesimal time limit. *viXra preprint viXra:1810.0023*, Dec 2018. URL <http://vixra.org/abs/1810.0023>.
- [30] Amir E BozorgMagham, Shane D Ross, and David G Schmale III. Real-time prediction of atmospheric Lagrangian coherent structures based on forecast data: An application and error analysis. *Physica D: Nonlinear Phenomena*, 258:47–60, 2013.
- [31] North american mesoscale model. <https://www.emc.ncep.noaa.gov/NAM/.php>. Accessed: 2019-01-18.
- [32] Fact sheet small unmanned aircraft regulations (part 107). [https://www.faa.gov/news/fact\\_sheets/news\\_story.cfm?newsId=22615](https://www.faa.gov/news/fact_sheets/news_story.cfm?newsId=22615). Accessed: 2019-03-08.
- [33] Jared A Grauer and Eugene A Morelli. Generic global aerodynamic model for aircraft. *Journal of Aircraft*, 52(1):13–21, January 2015. doi: 10.2514/1.C032888.
- [34] Shawn C Shadden, Francois Lekien, and Jerrold E Marsden. Definition and properties of Lagrangian coherent structures from finite-time Lyapunov exponents in two-dimensional aperiodic flows. *Physica D: Nonlinear Phenomena*, 212(3):271–304, 2005.
- [35] Irina I Rypina, Michael G Brown, Francisco J Beron-Vera, Huseyin Kocak, María J Olascoaga, and Ilya A Udovydchenkov. On the Lagrangian dynamics of atmospheric zonal jets and the permeability of the stratospheric polar vortex. *Journal of the Atmospheric Sciences*, 64(10):3595–3610, 2007.
- [36] Peter J Nolan, Hosein Foroutan, and Shane D Ross. The understanding of pollutant transport in the atmosphere: Lagrangian coherent structures. Poster presented at the *17th Annual CMAS Conference*, October 2018. [https://cmascenter.org/conference//2018/slides/foroutan\\_understanding\\_pollutant\\_2018.pdf](https://cmascenter.org/conference//2018/slides/foroutan_understanding_pollutant_2018.pdf).

- [37] Bernard Etkin. *Dynamics of Atmospheric Flight*. John Wiley & Sons, New York, 1972.

# Chapter 4

## Coordinated Unmanned Aircraft System and Ground-based Weather Measurements to Predict Lagrangian Coherent Structures

### Attribution

This manuscript represents a collaborative work with James Pinto, Javier González-Rocha, Anders Jensen, Christina N. Vezzi, Sean C. C. Bailey, Gijs de Boer, Constantin Diehl, Roger Laurence III, Craig W. Powers, Hosein Foroutan, Shane D. Ross and David G. Schmale III, which has been published in the journal *Sensors*.

Peter J. Nolan generated the LCS computations, analyzed data across platforms, and led the writing of the manuscript. James Pinto and Anders Jensen generated the WRF-LES model

and assisted in writing the manuscript. Javier González-Rocha operated one UAS, and assisted in analyzing the data and writing the manuscript. Christina N. Vezzi and Sean C. C. Bailey analyzed data from the 2 m flux tower and assisted in writing the manuscript. Gijs de Boer organized the ISARRA campaign and assisted in writing the manuscript. Roger Lawrence III analyzed data from the MURC, and assisted in writing the manuscript. Constantin Diehl organized airspace logistics for the campaign and assisted in writing the manuscript. Craig W. Powers designed the mount for the UAS wind sensor and assisted in writing the manuscript. Hosein Foroutan and Shane D. Ross contributed to model computations and assisted in designing the experiment and writing the manuscript. David G. Schmale III managed the project, designed experiments, operated both UASs, analyzed data, and assisted in writing the manuscript.

## **abstract**

Concentrations of airborne chemical and biological agents from a hazardous release are not spread uniformly. Instead, there are regions of higher concentration, in part due to local atmospheric flow conditions which can attract agents. We equipped a ground station and two rotary-wing unmanned aircraft systems (UASs) with ultrasonic anemometers. Flights reported here were conducted 10 to 15 meters above ground level (AGL) at the Leach Airfield in the San Luis Valley, Colorado as part of the Lower Atmospheric Process Studies at Elevation - a Remotely-Piloted Aircraft Team Experiment (LAPSE-RATE) campaign in 2018. The ultrasonic anemometers were used to collect simultaneous measurements of wind speed, wind direction, and temperature in a fixed triangle pattern; each sensor was located at one apex of a triangle with  $\sim 100$  to 200 meters on each side, depending on the experiment. A WRF-LES model was used to determine the wind field across the sampling domain. Data

from the ground-based sensors and the two UASs were used to detect attracting regions (also known as Lagrangian Coherent Structures, or LCSs), which have the potential to transport high concentrations of agents. This unique framework for detection of high concentration regions is based on estimates of the horizontal wind gradient tensor. To our knowledge, our work represents the first direct measurement of an LCS indicator in the atmosphere using a team of sensors. Our ultimate goal is to use environmental data from swarms of sensors to drive transport models of hazardous agents that can lead to real-time proper decisions regarding rapid emergency responses. The integration of real-time data from unmanned assets, advanced mathematical techniques for transport analysis, and predictive models can help assist in emergency response decisions in the future.

## 1 Introduction

Atmospheric wind velocity measurements are critical to air quality [1], weather forecasting [2], and climate studies [3]. Unmanned aircraft systems (UASs) are an emerging technology for atmospheric wind velocity measurements near the surface of Earth [4] where it is difficult and expensive to operate conventional atmospheric sensors reliably. Small UASs, both fixed- and rotary-wing, are low-cost, mobile, and portable with some trade-offs involving flight characteristics. Fixed-wing UASs can fly for periods of around 45 minutes continuously, but are limited by their flight envelope to open-space operations for launch, maneuvering, and recovery. Rotary-wing UASs can hover, allowing for operations in complex environments, but have limited battery power and generally have shorter flight periods.

Efforts to measure atmospheric properties with UASs began as early as 1971 with [5] using a small fixed-wing platform to carry sensors for direct measurements of atmospheric properties [6]. Similar studies have since followed suit using different mission-specific aircraft designs as

detailed in [6]. More recently, indirect approaches have been developed to infer wind velocity using model-based state estimation algorithms. These methods have implemented, among others, the Extended Kalman Filter [7], Unscented Kalman Filter [8], or Finite Horizon Filter [9] to reconstruct wind velocity estimates from inertial and airspeed aircraft sensor measurements. In general, both direct and indirect approaches have yielded promising results as sensor technology continues to advance.

Direct methods of wind estimation encompass the integration of atmospheric flow sensors directly onto the rotary-wing platform [10, 11]. This method has been tested using vane [12], solid-state [13, 14], hot-wire [10], and sonic anemometers [10, 12] as part of sensor placement studies. Results from experiments have demonstrated sensor location to be critical as the propeller downwash can corrupt measurements of ambient wind velocity. Indirect methods, on the other hand, measure wind velocity employing model-free and model-based algorithms. Model-free algorithms render wind velocity measurements from a static relationship between tilt and air-relative velocity [15, 16] or the angular kinematics accessed from on-board inertial measurement unit (IMU) sensors [16, 17]. Model-based algorithms, in contrast, use a physics-based model along with aircraft state measurements to reconstruct wind velocity using a state observer [18, 19, 20].

Analyzing atmospheric flows can be challenging due to their chaotic nature. Lagrangian coherent structures (LCSs) have become an increasingly popular tool for the analysis of atmospheric systems. LCSs provide a way to visualize how particles in a flow will evolve; they constitute the skeleton of the flow pattern, particularly regions which are attracting or repelling of nearby fluid, as in figure 4.1. For instance, attracting LCSs can correspond to regions of enhanced concentrations of some atmospheric borne chemical species, such as water vapor, pollutants, or hazardous material. Previous work [21, 22, 23, 24, 25, 26, 27, 28] has shown that LCSs tend to coincide with ridges of the finite-time Lyapunov exponent

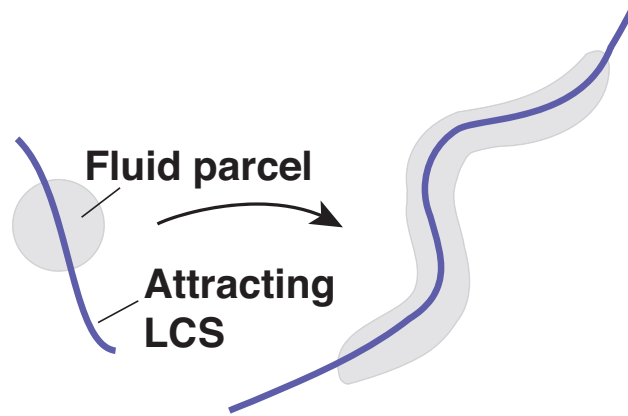


Figure 4.1: Schematic illustration of an attracting LCS, and its effect on a fluid parcel over a short advection time.

(FTLE) field, which measures the stretching of an air parcel as it advects under the wind. Recently, new Eulerian methods have been developed to detect regions of high attraction and repulsion in fluid flows without the need for simulating air particle paths. These methods are based on the horizontal wind velocity gradient and can be used to calculate an instantaneous approximation to Lagrangian quantities such as LCSs or the FTLE field [29, 30, 31]. We will take advantage of these Eulerian methods to look for potential LCSs in the experimental results presented here.

Measurements used in this campaign were obtained between 14-19 July, 2018 as part of a community-centric field experiment. This experiment was organized in association with the with the International Society for Atmospheric Research using Remotely-Piloted Aircraft (ISARRA) conference held the week before at the University of Colorado Boulder. This “flight week”, titled Lower Atmospheric Process Studies at Elevation - a Remotely-piloted Aircraft Team Experiment (LAPSE-RATE) took place in the San Luis Valley, Colorado. This activity included participation by a variety of university, government, and industry teams. Over the course of six days, over 100 participants supported the coordinated deployment of 50 different unmanned aircraft to complete 1287 total flights, accumulating 262.4

flight hours. These flights were conducted under both Federal Aviation Administration (FAA) Certificates of Authorization (COAs) and FAA Part 107, with the COAs generally supporting flights up to altitudes of 3000 feet above ground level. In addition to the aerial assets, a variety of ground-based observational assets were deployed. These included the Collaborative Lower Atmospheric Mobile Profiling System (CLAMPS), two Doppler Lidar systems, numerous radiosondes, and mobile surface instrumentation associated with vehicles and small towers. Over the course of the week, flight operations spanned a large ( 3500 km<sup>2</sup>) area over the northern San Luis Valley. The open space around Leach Airfield supported the simultaneous deployment of several aircraft at a time, with these platforms operating alongside several ground-based measurement systems as well as regular radiosonde launches to provide comparison datasets using well-characterized methods and sensors.

In this manuscript, we describe the use of multiple UASs equipped with ultrasonic anemometers to measure wind and temperature and forecast LCSs. The specific objectives of this work were to: develop and deploy multiple UASs equipped with ultrasonic anemometers to measure wind speed, wind direction, and temperature; compare data from the sonic anemometers onboard the UAS against two different ground-based weather stations and a weather research and forecasting large eddy simulation (WRF-LES) model; and conduct a series of coordinated UAS flights to detect LCSs based on estimates of the horizontal wind gradient tensor. Our ultimate goal is to use environmental data from UASs to drive atmospheric transport models of hazardous agents that can lead to appropriate decisions regarding rapid emergency responses.

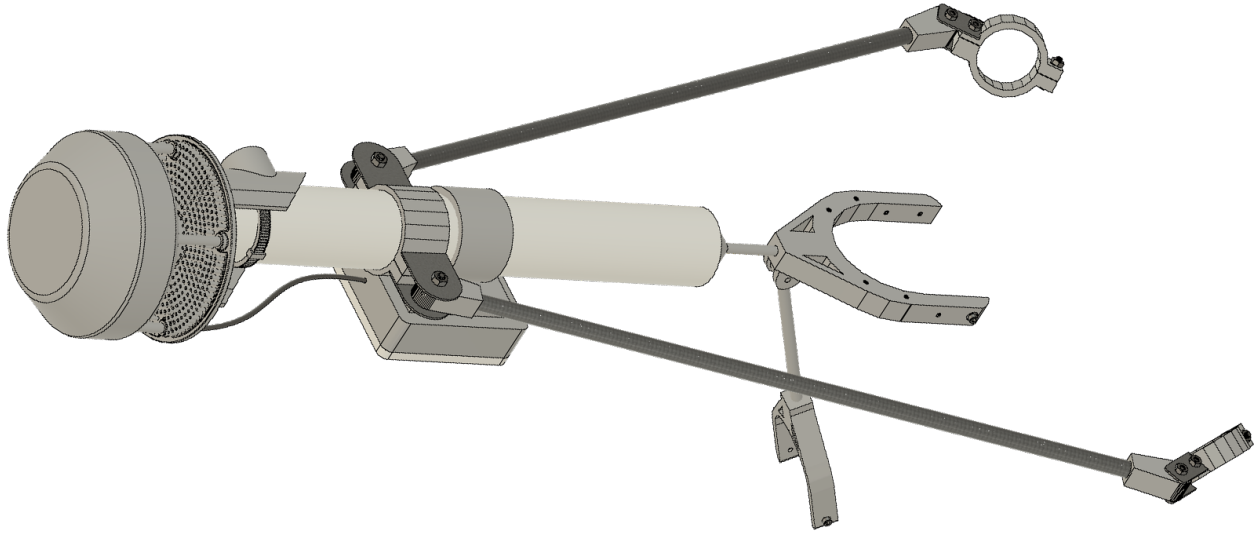


Figure 4.2: Schematic of Inspire 2 sampler assembly. An interactive 3D version can be found at <https://a360.co/2OnKT14>

## 2 Materials and Methods

### 2.1 Sensor Package onboard UAS

Two Inspire 2 quadcopters (DJI, Shenzhen, China) were each equipped with an Atmos 22 ultrasonic anemometer (Meter Environment, Pullman, WA) and a Microlog SDI MP/E datalogger (Environmental Measuring Systems, Czech Republic). The Inspire 2 quadcopters were registered with the FAA; registration numbers FA37XL79KC and FA3KHWTTTCY. The sensor package was mounted to the airframe of the UAS using carbon fiber rods and custom 3d-printed pieces (found at <https://github.com/SchmaleLab/Schmale-Lab-3D-Printing-Files-Nolan-et-al-Sensors-2018>). The Atmos 22 weighed 424 grams and was 10 cm in diameter by 16 cm in height. The anemometer measured horizontal wind speed from 0 to  $30\text{m s}^{-1}$  with a resolution of  $0.01\text{m s}^{-1} \pm 0.3\text{m s}^{-1}$  or 3% and wind direction from 0 to  $359^\circ$  with a resolution of  $1^\circ \pm 5^\circ$ . The datalogger recorded measurements every 15 seconds. A structure was developed to mount the anemometer to the DJI Inspire 2 using a 30 cm long by 3.8 cm

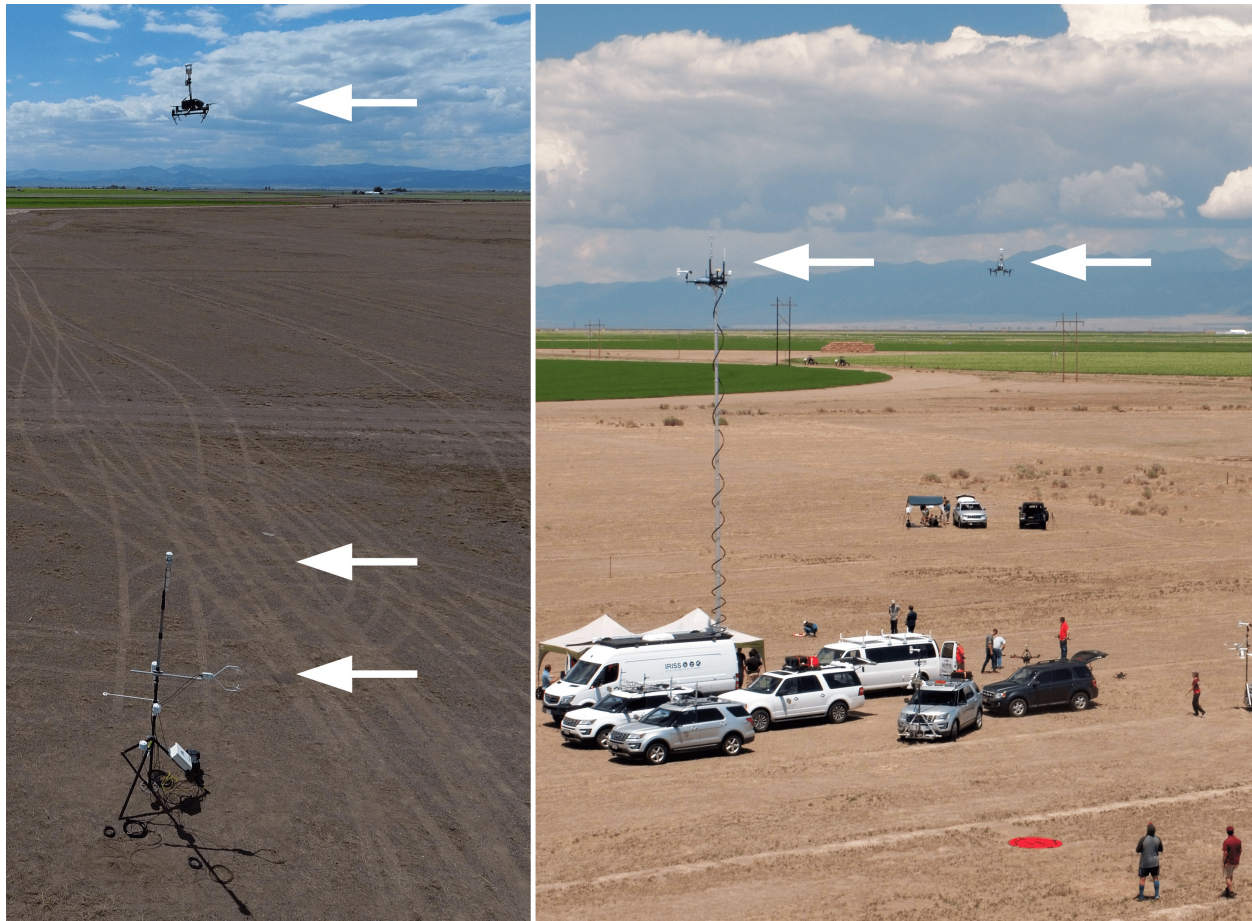


Figure 4.3: Calibration flight with vertical array of sensors at 10 m (UAS with Atmos 22 sonic anemometer), 4 m (Atmos22 sonic anemometer), and 2 m (CSAT3 sonic anemometer) (left). White arrows indicate the sensors at each of the respective heights. Calibration flight (B2) with one ground-based sensor on the MURC tower and one UAS, both at 15 m (right). White arrows indicate the sensors for each of the platforms.

wide polypropylene tube, 3D printed components and carbon fiber tubes. The anemometer was mounted to the top of the polypropylene tube and the data logger was mounted to the tube below the anemometer. Four carbon fiber mounting arms attached the pole vertically to the Inspire 2 using stainless steel bolts: one directly below the vertical tube, one to each left and right arm, and one to the rear of the Inspire 2 main body. The data logger was set to record continuously before each flight.



Figure 4.4: Simultaneous flights with sensors in a triangle formation (white arrows). Both UASs were operating off of marks on the taxiway, and the MURC tower was stationed north of the UAS operations.

## 2.2 Permissions for Flight Operations

The six counties of the San Luis Valley (SLV), through the support of UAS Colorado and CU Boulder, established a UAS program in 2014 including extensive FAA Permits to operate UASs under public entity Certificates of Authorization (COAs) in a 5,100,000 square mile area of the valley up to 15,000 ft MSL, which equates to about 7,500 ft AGL in the central valley. All flights were deconflicted with Local Crop-Dusting Operations, military low altitude training operations along VR routes, routine daily airline operations in and out

of KALS, and Local Flight For Life as well as private aircraft operations in the area. UAS pilots for the missions reported in this manuscript were certified Remote Pilots under Part 107; (Schmale, Certificate Number 4038906; González-Rocha, Certificate Number 4010055).

### 2.3 Coordinated aerial and ground-based measurements

#### Calibration flight with vertical array of sensors at 10 m (UAS), 4 m (Ground), and 2 m (Ground)

One UAS flight (UAS\_B1, Table 4.1) was conducted over a 4 m flux tower with sensors at fixed heights of 4 m (Atmos 22 sonic anemometer package) and 2 m (CSAT-3 sonic anemometer from Campbell Scientific) (figure 4.3). The accuracy of the CSAT-3 was between  $\pm 2$  and  $\pm 6\%$  with  $\pm 0.08 \text{ m s}^{-1}$  bias precision. Output from the CSAT-3 was logged at 20 Hz via RS232 using a Kangaroo PC portable computer mounted in a weatherproof enclosure. Additional measurements of temperature and humidity were provided at 2 m via a Campbell Scientific E+E Elektronik EE181 digital probe ( $\pm 0.2^\circ\text{C}$ ,  $\pm 2.3\% \text{RH}$ ). This sensor was supplemented by two Campbell Scientific CS215 digital sensors ( $\pm 0.4^\circ\text{C}$ ,  $\pm 4\% \text{RH}$ ) located 1.5 m and 0.75 m above ground level. All temperature and humidity sensors were housed in a solar radiation shield and logged every 3 seconds via a Campbell Scientific CR1000X measurement and control data logger. Additional sensors on the flux tower logged every 3 s, but not used in the present study, included a Setra 278 digital barometer, Kipp and Zonen NR-LITE2 Net Radiometer, two Hukseflux HFP01 Soil Heat Flux Plates, a Campbell Scientific CS655 water content reflectometer, and Campbell Scientific TCAV averaging soil thermocouple probe. All sensors were factory calibrated within one year of use, although intercomparison measurements in a laboratory environment revealed that the EE181 sensor had a consistent  $0.5^\circ\text{C}$  bias which was removed from the measurements reported here.

### **Calibration flights with one ground-based sensor at 15 m (MURC) and one UAS at 15 m**

Two UASs flights (UAS\_A2 and UAS\_B2, Table 4.1) of about 10 min at 15 m AGL were conducted adjacent to the Mobile UAS Research Collaboratory (MURC) tower (figure 4.3). The MURC is equipped with a 15 m extendable mast containing several meteorological sensors including a Gill MetPak Pro Base Station that provided barometric pressure, temperature, and humidity; a Gill 3D sonic anemometer for 3D wind measurements; and an R.M. Young Wind Monitor anemometer which provided a redundant horizontal wind measurement.

### **Simultaneous flights with sensors at 15 m in a triangle formation (two UASs, and two ground sensors)**

Eight coordinated flights (Table 4.1) were conducted at 15 m AGL in a fixed triangle pattern (each sensor was located at one apex of a triangle with about 100 to 200 meters on each side, depending on the experiment) (figure 4.4).

## **2.4 WRF-LES model**

Version 3.9.1.1 of the Weather Research and Forecasting (WRF) model [32, 33] was used to downscale mesoscale flows to predict the evolution of winds and turbulence in the boundary layer during ISARRA flight week. The model set up was similar to that described by [34]. We used the nesting configuration to downscale operational forecast from 3 km resolution NOAA/NCEP High Resolution Rapid Refresh (HRRR) to a resolution of 111 m using 45 vertical levels. The vertical levels were spaced to maximize resolution in the lowest 2 km of the atmosphere. The nests were configured using one-way feedback (coarse mesh to fine mesh only). Following [34], a refinement ratio of 10 was used between the WRF-LES grid

and its parent domain in order to minimize the impact of the terra incognita range of grid resolutions for which boundary layer parameterizations were not designed [35]. Boundary layer turbulence in D01 was parameterized using the MYNN2 boundary layer while unresolved turbulence in D02 was computed using a sub-grid scale (SGS) closure that includes a prognostic equation for turbulent kinetic energy following [36]. The land surface type was specified using the 20-category MODIS land use dataset. Model forecast data was output at each grid point every 10 min. A higher output rate (0.66 sec) was enabled at select grid points that were coincident with ISARRA profiling sites including Leach Airfield. Data used in this study were obtained from WRF-LES runs initialized at 11:00 UTC using HRRR data to initialize and drive the lateral boundaries of the downscaling system. The HRRR is a rapidly-updating forecast system that uses 3DVAR data assimilation to incorporate a wide range of observations to produce a new 18 hour forecast every hour [37]. The outer grid of the downscaling system, with 1 km grid spacing, was run for 6 hours to spin up dynamically-balanced forcing which was then used to initialize and force the inner-most WRF-LES grid. Data from the forecasts were interpolated to a set of heights above the ground (including 30, 80 and 150 m AGL) and were also interpolated from the Lambert Conformal computational grid onto a regularly spaced grid using bilinear interpolation.

## 2.5 Lagrangian-Eulerian analysis

Due to their chaotic nature, time-dependent unsteady fluid flows such as atmospheric flows can be challenging to analyze. As mentioned in the introduction, Lagrangian methods such as LCS and the FTLE field have become popular tools to analyze the transport of particles in such flows. Calculating the FTLE field requires Lagrangian data, i.e., numerically simulating the advected paths of fluid particles. The integration of particle trajectories tends to be computationally expensive and necessitates a greater degree of spatial and temporal

information than can reasonably be gathered by operators in the field.

New Eulerian tools have recently been developed which use velocity gradients, instead of integrating particle trajectories. This allows for flows to be analyzed by pointwise measurements at as few as three points. These velocity gradients are assembled into the Eulerian rate-of-strain tensor,  $\mathbf{S}$  in eq. (4.3) discussed below. In [30] it is shown that  $\mathbf{S}$  can provide an instantaneous approximation of the Lagrangian dynamics of a fluid flow. Ref [30] further states that we should seek objective Eulerian coherent structures (OECSs) based on the invariants of  $\mathbf{S}$ , as short-term limits of LCSs. Further work on this topic [31] has also shown that in two-dimensional flows, the eigenvalues of  $\mathbf{S}$ ,  $s_1 < s_2$ , are the limits of the backward-time and forward-time FTLE fields as integration (advection) time goes to zero. Ref [31] further posits that troughs of the  $s_1$  field can be identified as instantaneous attracting LCSs and ridges of the  $s_2$  field can be identified as instantaneous repelling LCSs. For the remainder of this manuscript we shall refer to  $s_1$  as the attraction rate and  $s_2$  as the repulsion rate.

For our analysis we be considering the fluid particle advection dynamical system,

$$\frac{d}{dt}\mathbf{x} = \mathbf{v}(\mathbf{x}, t), \quad (4.1)$$

$$\mathbf{x}_0 = \mathbf{x}(t_0). \quad (4.2)$$

In this system  $\mathbf{x}(t)$  is the position vector of a fluid parcel at time  $t$  and  $\mathbf{v}(\mathbf{x}, t)$  is the horizontal wind velocity vector at position  $\mathbf{x}(t)$ , time  $t$ . We define the components of the horizontal position vector,  $\mathbf{x} = (x, y)$ , where  $x$  is the eastward position and  $y$  is the northward position, measured either in meters with respect to some convenient reference point or in longitude and latitude, respectively. We will analyze this system by looking at the attraction rate, which is the minimum eigenvalue,  $s_1$ , of the Eulerian rate-of-strain tensor,  $\mathbf{S}(\mathbf{x}, t)$ . The Eulerian

rate-of-strain tensor is defined based on the horizontal wind gradient,

$$\nabla \mathbf{v}(\mathbf{x}, t),$$

as

$$\mathbf{S}(\mathbf{x}, t) = \frac{1}{2} (\nabla \mathbf{v}(\mathbf{x}, t) + \nabla \mathbf{v}(\mathbf{x}, t)^T). \quad (4.3)$$

As stated before, the attraction rate provides a means of identifying the attracting OECSs, which are the instantaneous LCSs. The attraction rate provides information on where material particles will converge (figure 4.1). The lower the value of the (negative) attraction rate, the more particles will be attracted to that point. We focus on the attraction rate given its importance for predicting enhanced concentrations of atmospherically advected tracers, as nearby particles will converge onto those features and flow with them as opposed to repelling features which particles will diverge from before flowing independent of those features.

## 2.6 Computation of Wind Gradient and Attraction Rate

In order to calculate the attraction rate we first needed to calculate the gradient of the wind velocity field,  $\nabla \mathbf{v}(\mathbf{x}, t)$ , for the spatiotemporally varying wind velocity vector  $\mathbf{v}(\mathbf{x}, t) = (u, v)$ , where  $u$  is the eastward wind component and  $v$  is the northward wind component. For an estimate of the gradient, three measurements of the wind velocity were simultaneously recorded by two UASs and one ground station. The wind velocity data taken from these measurements was then interpolated to a fourth point between the three sensors, figure 4.5. This point is chosen to be along a north-south line with one of the sensors and an east-west line with another. A depiction of the true situation based on a satellite photo can be seen in figure 4.6.

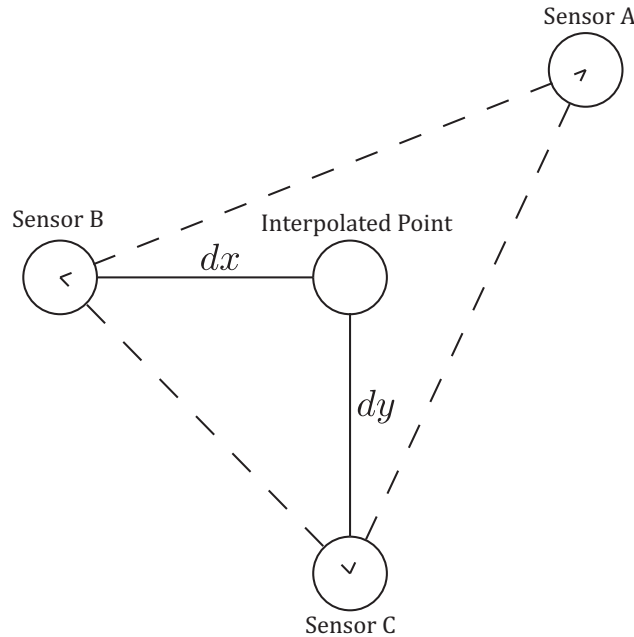


Figure 4.5: Schematic of how the velocity gradient,  $\nabla\mathbf{v}(\mathbf{x}, t)$ , was computed from sensor measurements. Using wind measurements from three independent sensors, a linear function was generated for a triangular element. This function was then used to interpolate the wind to an interpolated point. A finite-difference scheme, eq. 4.4, was then used to calculate the gradient of the two components,  $u$  and  $v$ , of the horizontal wind.

The velocity was interpolated to the fourth point using linear interpolation provided by the `griddata` routine from Python’s `SciPy` module. Once the velocity was interpolated, the gradient of the velocity field was calculated using a finite-difference scheme between the velocity at the interpolated point and the velocity from the sensors directly north/south and east/west. For example, with the setup shown in figure 4.5, the gradient of  $u$  is calculated as

$$\frac{\partial u}{\partial x} \approx \frac{u_{interp} - u_B}{dx}, \quad \frac{\partial u}{\partial y} \approx \frac{u_{interp} - u_C}{dy}, \quad (4.4)$$

where  $u_{interp}$  is  $u$  at the interpolated point,  $u_B$  is  $u$  at sensor B, and  $u_C$  is  $u$  at sensor C. This method could then be applied to  $v$  as well to get the full horizontal gradient of the

wind vector,

$$\nabla \mathbf{v} = \begin{bmatrix} \frac{\partial u}{\partial x} & \frac{\partial u}{\partial y} \\ \frac{\partial v}{\partial x} & \frac{\partial v}{\partial y} \end{bmatrix}, \quad (4.5)$$

and the Eulerian rate-of-strain tensor,

$$\mathbf{S} = \begin{bmatrix} \frac{\partial u}{\partial x} & \frac{1}{2} \left( \frac{\partial u}{\partial y} + \frac{\partial v}{\partial x} \right) \\ \frac{1}{2} \left( \frac{\partial u}{\partial y} + \frac{\partial v}{\partial x} \right) & \frac{\partial v}{\partial y} \end{bmatrix}. \quad (4.6)$$

The attraction rate,  $s_1$  is then given analytically by

$$s_1 = \frac{1}{2} \left( \frac{\partial u}{\partial x} + \frac{\partial v}{\partial y} \right) - \frac{1}{2} \sqrt{\left( \frac{\partial u}{\partial x} - \frac{\partial v}{\partial y} \right)^2 + \left( \frac{\partial u}{\partial y} + \frac{\partial v}{\partial x} \right)^2}. \quad (4.7)$$

## 2.7 Uncertainty Analysis

We can quantify the uncertainty in our gradient approximation as follows. For example, for the gradient component,  $\frac{\partial u}{\partial x}$ , we can estimate the uncertainty  $\delta \left( \frac{\partial u}{\partial x} \right)$  using (4.4) as,

$$\begin{aligned} \delta \left( \frac{\partial u}{\partial x} \right) &= \left| \frac{\partial \left( \frac{\partial u}{\partial x} \right)}{\partial u_{interp}} \right| \delta(u_{interp}) + \left| \frac{\partial \left( \frac{\partial u}{\partial x} \right)}{\partial u_B} \right| \delta(u_B) + \left| \frac{\partial \left( \frac{\partial u}{\partial x} \right)}{\partial (dx)} \right| \delta(dx) \\ &= \frac{1}{dx} \delta(u_{interp}) + \frac{1}{dx} \delta(u_B) + \frac{1}{dx^2} |u_{interp} - u_B| \delta(dx) \\ &= \frac{1}{dx} \left( \delta(u_{interp}) + \delta(u_B) + \left| \frac{\partial u}{\partial x} \right| \delta(dx) \right). \end{aligned} \quad (4.8)$$

where  $\delta(\cdot)$  denotes the uncertainty in the measured quantity. SciPy's griddata routine uses a barycentric interpolation scheme for linear interpolation, thus we can rewrite  $u_{interp}$  as,

$$u_{interp} = c_1 u_A + c_2 u_B + c_3 u_C, \quad (4.9)$$

subject to the constraint that  $c_1 + c_2 + c_3 = 1$ . So, since the anemometers all have the same error,  $\delta(u_A) = \delta(u_B) = \delta(u_C)$ , we have

$$\delta(u_{interp}) = \delta(u_A) \quad (4.10)$$

and

$$\begin{aligned} \delta\left(\frac{\partial u}{\partial x}\right) &= \frac{1}{dx} (c_1 \delta(u_A) + (1 + c_2) \delta(u_B) + c_3 \delta(u_C) + \left|\frac{\partial u}{\partial x}\right| \delta(dx)) \\ &= \frac{1}{dx} (2\delta(u_A) + \left|\frac{\partial u}{\partial x}\right| \delta(dx)) \end{aligned} \quad (4.11)$$

Similar results hold for the other components of the velocity gradient (4.5).

We can also determine the uncertainty in the attraction rate  $s_1$ , based on (4.7), as

$$\delta(s_1) = \left| \frac{\partial s_1}{\partial\left(\frac{\partial u}{\partial x}\right)} \right| \delta\left(\frac{\partial u}{\partial x}\right) + \left| \frac{\partial s_1}{\partial\left(\frac{\partial u}{\partial y}\right)} \right| \delta\left(\frac{\partial u}{\partial y}\right) + \left| \frac{\partial s_1}{\partial\left(\frac{\partial v}{\partial x}\right)} \right| \delta\left(\frac{\partial v}{\partial x}\right) + \left| \frac{\partial s_1}{\partial\left(\frac{\partial v}{\partial y}\right)} \right| \delta\left(\frac{\partial v}{\partial y}\right) \quad (4.12)$$

where

$$\begin{aligned} \frac{\partial s_1}{\partial\left(\frac{\partial u}{\partial x}\right)} &= \frac{1}{2} - \frac{1}{2c} \left( \frac{\partial u}{\partial x} - \frac{\partial v}{\partial y} \right), \\ \frac{\partial s_1}{\partial\left(\frac{\partial v}{\partial y}\right)} &= \frac{1}{2} + \frac{1}{2c} \left( \frac{\partial u}{\partial x} - \frac{\partial v}{\partial y} \right), \\ \frac{\partial s_1}{\partial\left(\frac{\partial u}{\partial y}\right)} &= \frac{\partial s_1}{\partial\left(\frac{\partial v}{\partial x}\right)} = -\frac{1}{2c} \left( \frac{\partial u}{\partial y} + \frac{\partial v}{\partial x} \right), \end{aligned} \quad (4.13)$$

and

$$c = \sqrt{\left(\frac{\partial u}{\partial x} - \frac{\partial v}{\partial y}\right)^2 + \left(\frac{\partial u}{\partial y} + \frac{\partial v}{\partial x}\right)^2}. \quad (4.14)$$

### 3 Results

UAS flights were conducted between 10 and 15 m AGL at the Leach Airfield in the San Luis Valley, Colorado as part of the ISARRA 2018 flight campaign (Table 4.1). The UASs were used to collect simultaneous measurements of wind speed, wind direction, and temperature in a fixed triangle pattern (each sensor was located at one apex of a triangle with 100 to 200 meters on each side, depending on the experiment, figures 4.5 and 4.6). In addition, a high resolution atmospheric simulations using WRF-LES model was used to determine the 4D (space and time) wind field across the sampling domain. Data from the ground-based sensors and the two UASs were used to detect LCSs.

Sensor Package	Description of operation	Date	Time Start	Time End	Height	Location	Lat	Long
UAS_A2	Calibration flight w/MURC.	14-Jul-2018	13:30:21	13:41:05	15	MURC Tower	37.781914	-106.041412
UAS_A4	Coordinated flight w/ B4	14-Jul-2018	16:43:07	16:54:55	10	East Runway	37.780315	-106.040772
UAS_A5	Coordinated flight w/ B5	14-Jul-2018	17:15:58	17:27:19	10	East Runway	37.780312	-106.040763
UAS_A16	Coordinated flight w/ B7	16-Jul-2018	14:42:07	14:53:04	15	East Runway	37.780308	-106.040753
UAS_A17	Coordinated flight w/ B8	16-Jul-2018	15:18:01	15:28:17	15	East Runway	37.780336	-106.040746
UAS_A22	Coordinated flight w/ B9	17-Jul-2018	12:36:00	12:47:24	15	East Runway	37.780287	-106.04076
UAS_A23	Coordinated flight w/ B10	17-Jul-2018	13:59:29	14:10:59	15	East Runway	37.780307	-106.040763
UAS_A25	Coordinated flight w/ B11	17-Jul-2018	15:07:39	15:19:02	15	East Runway	37.780398	-106.040762
UAS_A26	Coordinated flight w/ B12	17-Jul-2018	15:41:53	15:53:11	15	East Runway	37.780338	-106.040762
UAS_B1	Calibration flight w/ Flux Tower.	13-Jul-2018	15:15:07	15:25:27	10	Above UK WS	-25.95749269	28.05921094
UAS_B2	Calibration flight w/ MURC.	14-Jul-2018	14:15:23	14:26:07	15	MURC Tower	37.78188077	-106.0414296
UAS_B4	Coordinated flight w/ A4	14-Jul-2018	16:42:10	16:52:40	10	West Runway	37.78155488	-106.0422978
UAS_B5	Coordinated flight w/ A5	14-Jul-2018	17:15:27	17:26:28	10	West Runway	37.7815583	-106.0422984
UAS_B7	Coordinated flight w/ A16	16-Jul-2018	14:43:05	14:52:42	18	West Runway	37.78156695	-106.0422614
UAS_B8	Coordinated flight w/ A17	16-Jul-2018	15:16:17	15:27:48	9	West Runway	37.78158549	-106.0422597
UAS_B9	Coordinated flight w/ A22	17-Jul-2018	12:35:22	12:46:56	15	West Runway	37.78153018	-106.0422848
UAS_B10	Coordinated flight w/ A23	17-Jul-2018	13:58:58	14:10:31	15	West Runway	37.78155617	-106.0422905
UAS_B11	Coordinated flight w/ A25	17-Jul-2018	15:07:12	15:18:49	15	West Runway	37.78156052	-106.0422956
UAS_B12	Coordinated flight w/ A26	17-Jul-2018	15:41:12	15:52:55	15	West Runway	37.78156436	-106.0422941
Ground1		13-Jul-2018	11:45:00	15:55:00	4	On Flux Tower	37.781644	-106.03917
Ground2		14-Jul-2018	8:00:00	18:30:00	4	On Flux Tower	37.781644	-106.03917
Ground3		15-Jul-2018	11:00:00	14:45:00	4	On Flux Tower	37.781644	-106.03917
Ground4		16-Jul-2018	8:40:00	15:35:00	15	On MURC Tower	37.782097	-106.041412
Ground5		17-Jul-2018	8:15:00	16:00:00	15	On MURC Tower	37.782005	-106.041504

Table 4.1: UAS mission and ground station details. UAS sensor packages were functionally identical. Time start and time end are in local time, Mountain Daylight Time. Height is in meters above ground level.



Figure 4.6: Satellite image of the sampling region with sensor locations marked with blue pins. A potential interpolated point is marked in yellow.

### 3.1 Comparison of Measurements

#### Calibration flights

Calibration flights were conducted to compare wind velocity and temperature measurements from UAS A and B to measurements from independent sensors installed at 2, 4 and 10

m AGL as shown in figure 4.3. The wind velocity and temperature independent sensors consisted of a CSAT3 sonic anemometer installed at 2 m, an Atmos22 sonic anemometer placed at 4 m or 15 m (on the MURC's tower), and the Gill 3D sonic anemometer mounted atop of the MURC's tower at 15 m. For comparison, measurements of temperature and wind velocity recorded at 15 m AGL were considered. Results from this analysis were used as a confidence benchmark for UAS-based measurements of wind velocity and temperature sensors.

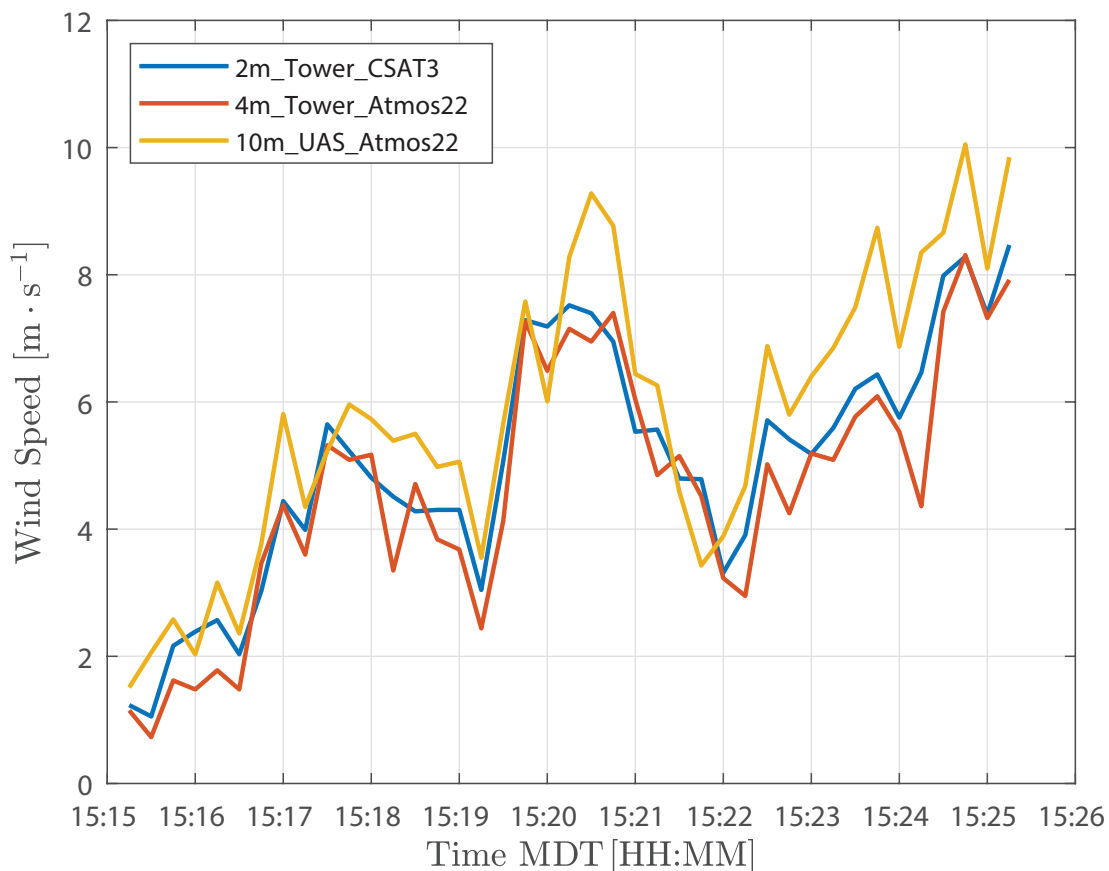


Figure 4.7: Comparison of wind speed measurements on the flux tower for a height of 2 m (CSAT3 sonic anemometer, yellow), 4 m (Atmos22 sonic anemometer), and 10 m (UAS with Atmos 22 sonic anemometer).

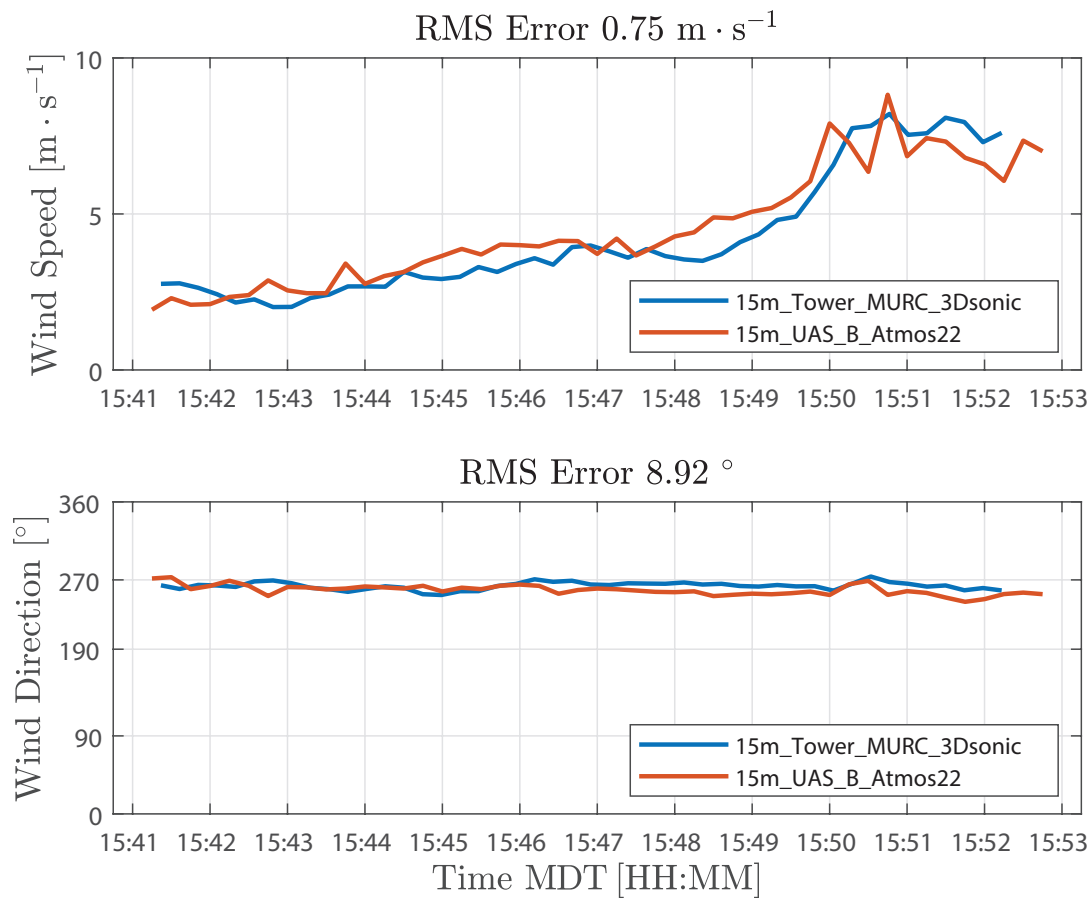


Figure 4.8: RMSE comparison for wind speed and direction measurements collected from UAS B and MURC Tower at 15 meters above ground level.

### Wind speed

In this section, we present results from measurements of wind speed and direction collected on July 13<sup>th</sup>, 2018. The wind conditions on this day were variable ranging between 2 and 10 m s<sup>-1</sup> as shown in figure 4.7. Atmospheric sampling involved four coordinated UAS missions, comprising eight distinct flights, along with measurements from the 15m\_tower\_Atmos22, 15m\_tower\_MURC\_3Dsonic, and the 2m\_tower\_CSAT3. Figure 4.7 shows the general trend in wind velocity as recorded by independent sensors at 2, 4 and 10 meters above ground level during a 10-minute interval. The wind speed trend with height is consistent with a power

law with coefficient  $\alpha \approx 0.2$ . In figure 4.8, measurements of wind speed and direction from UAS B and MURC were compared at 15 m AGL. Agreement for wind speed and direction were determined using a RMSE metric. Results show an RMS error of  $0.75 \text{ ms}^{-1}$  and  $8.9^\circ$  for wind speed and direction, respectively.

In figures 4.9 and 4.10 wind speed measurements from multiple sensors are displayed. Figure 4.9 shows the measurements from the ground based 15m\_tower\_MURC\_3Dsonic (blue) and 15m\_tower\_Atmos22 (orange), overlaid with measurements from the 15m\_UAS\_A\_Atmos22 (black). Figure 4.10 also shows the measurements from the ground based 15m\_tower\_MURC\_3Dsonic (blue) and 15m\_tower\_Atmos22 (orange), but overlaid with the 15m\_UAS\_B\_Atmos22 measurements (black). The UAS A flights shown are 22, 23, 25, 26. The UAS B flights shown are 9, 10, 11, 12. Details regarding the flights can be found in Table 4.1. Pearson correlation coefficients for these wind speed measurements range from 0.868 to 0.970 and can be found in Table 4.2.

In figure 4.11, we show the wind speed measurements associated with our attraction rate calculations (orange) along with wind speed predictions from WRF-LES model (blue), overlaid with mission averages for the sensor measurements (black). Mission averages are included for the period over which all three sensors were operating. For this comparison, a temporal resolution of 0.66 s was used for the WRF-LES model output. To calculate the wind speed, measurements were taken from two concurrent UAS flights as well as the 15m\_tower\_MURC\_3Dsonic and interpolated to the point where the attraction rate was computed, figures 4.5 and 4.6. The wind speed from the WRF-LES model came from the grid point nearest to where the attraction rate was calculated.

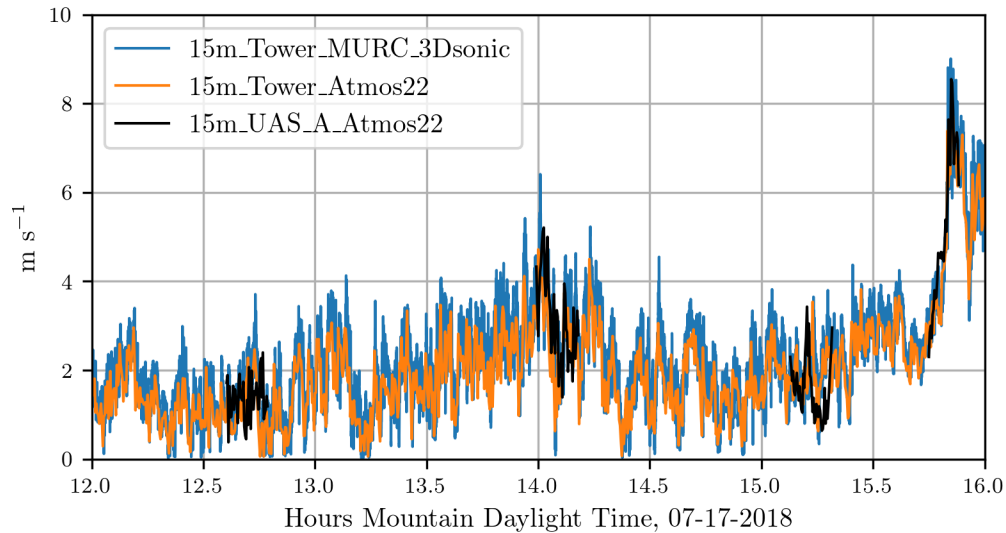


Figure 4.9: Comparison of wind speed measurements from UAS A and ground based sensors.

	15m_Tower_MURC_3Dsonic	15m_Tower_Atmos22	15m_UAS_A_Atmos22	15m_UAS_B_Atmos22
15m_Tower_MURC_3Dsonic	–	0.970	0.876	0.914
15m_Tower_Atmos22		–	0.868	0.895
15m_UAS_A_Atmos22			–	0.868
15m_UAS_B_Atmos22				–

Table 4.2: Pearson correlation coefficients for wind speed measurements between different UAS packages and ground based sensors.

### 3.2 Attraction rate measurements

In this section we present our results for attraction rate as calculated from our wind velocity measurements using the UAS and ground station method described in section 2.6. As a comparison we show the attraction rate as calculated from the WRF-LES model predictions. In order to get a picture of what was happening on a larger scale, we also calculated the attraction rate over the San Luis Valley using the 10 m velocity field from the WRF-LES model.

In figure 4.13, we show the attraction rate as calculated from the measurements provided by the two UASs and the 15m.tower\_MURC\_3Dsonic (orange) along with the attraction rate calculated from WRF-LES model predictions (blue), overlaid with mission averages for the sensor measurements (black). The uncertainty ranges for the attraction rate measurements

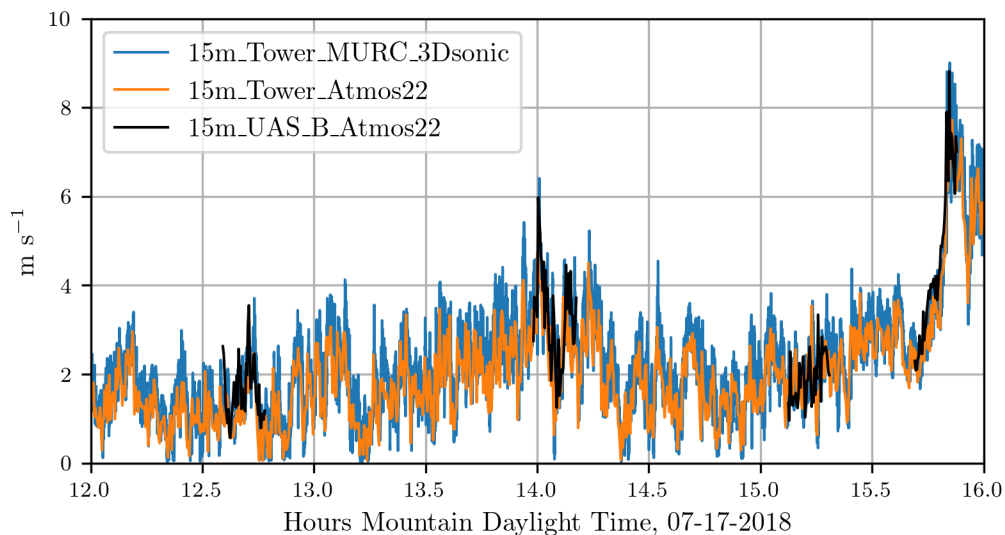


Figure 4.10: Comparison of wind speed measurements from UAS B and ground based sensors.

are shown in gray. Mission averages are averages for the period over which all 3 sensors were operating. For this comparison the WRF-LES model data was at a temporal resolution of 0.66s. The attraction rate from the WRF-LES model’s wind predictions was calculated using a central finite-difference scheme from a five point stencil centered on the grid point nearest to where the attraction rate was calculated from the UASs and the 15m\_tower\_MURC\_3Dsonic measurements. In yellow we highlight the time periods around the predicted attraction rate fields shown in figures 4.14 and 4.15. We display the gradients that were used to calculate attraction rate in figure 4.12. The gradients from the WRF-LES model (blue) are overlaid with those from our sensors (orange). We also show the range of uncertainty for our sensor gradient calculations in gray.

In figures 4.14 and 4.15, we show the attraction rate field over the San Luis valley on July 17<sup>th</sup> 2018 as calculated from the WRF-LES model’s 10 m velocity field prediction. In figure 4.14, we show the attraction rate field at 1400 MDT. This time was chosen to display due to a large discrepancy between the WRF-LES model’s attraction rate prediction and the attraction rate as calculated from real-world data. In figure 4.15, we show the attraction

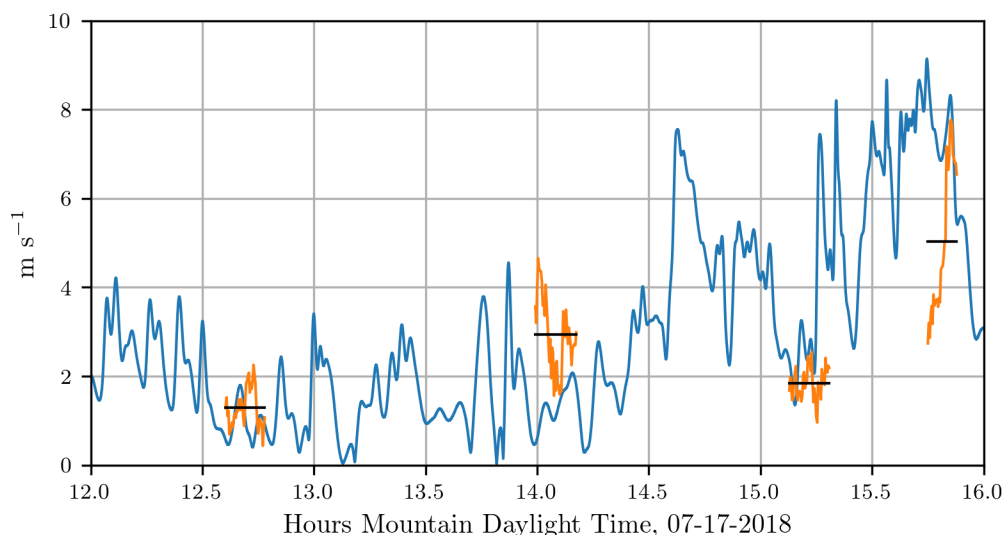


Figure 4.11: Wind speed from WRF-LES grid point nearest to where the attraction rate was calculated (blue) and wind speed as measured by sensors, interpolated to the attraction rate position (orange) overlaid with flight average of the wind speed (black). Wind speed from the WRF-LES comes from the 10m height level, while wind speed measurements were performed by sensors at 15m.

rate field at 1550 MDT. This time was chosen because an attracting front was passing through our sampling region out of the east. After the front passes the field is noticeable smoother. In both figures, the point where the attraction rate was calculated for the time series in figure 4.13 is shown as a red dot. An animation of the attracting rate field over the San Luis valley can be found at [attraction rate link](#).

## 4 Discussion

Concentrations of airborne chemical and biological agents from a hazardous release are not spread uniformly. Instead, there are regions of higher concentration, in part due to local atmospheric flow conditions which can attract agents [24, 27, 38, 39, 40]. New tools and technology are needed to monitor and forecast atmospheric transport phenomena [20]. Here, we have described a series of unique field experiments to collect simultaneous measurements

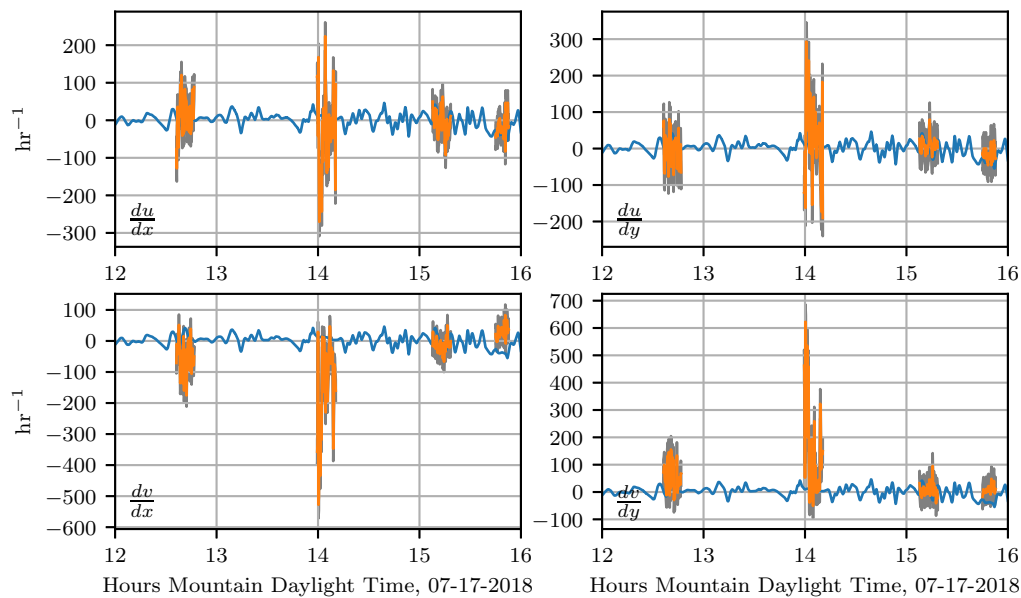


Figure 4.12: The velocity gradient from WRF-LES predictions (blue) and the velocity gradient as calculated from sensor measurements (orange). The velocity gradient from the WRF-LES comes from the 10 m height level wind speed, while wind speed measurements used to calculate the velocity gradient were performed by sensors at 15 m. The uncertainty ranges for the velocity gradient as calculated from sensor measurements are shown in gray.

of wind speed, wind direction, and temperature using multiple UASs and ground stations. Data from these sensors were compared to a WRF-LES model, and were used to forecast LCS.

Overall, the WRF-LES model provided fairly accurate predictions of both the winds and the attraction rate with some caveats. The wind speed predictions from the WRF-LES model followed the general trend measured by the sensors with both modeled and observed winds ranging between 0 and 4 m s<sup>-1</sup> during the early afternoon increasing late in the day in response to the development of moist convection and gusty outflows. Modeling the exact timing of deep moist convection and associate gusty winds at a single grid point is not possible, but rather, can be determined in a statistical sense by compositing forecast information across a much larger area of similar surface type. As seen in the attraction rate field (Figures 4.14 and 4.15), visual inspection of the modeled 10 m winds reveals very

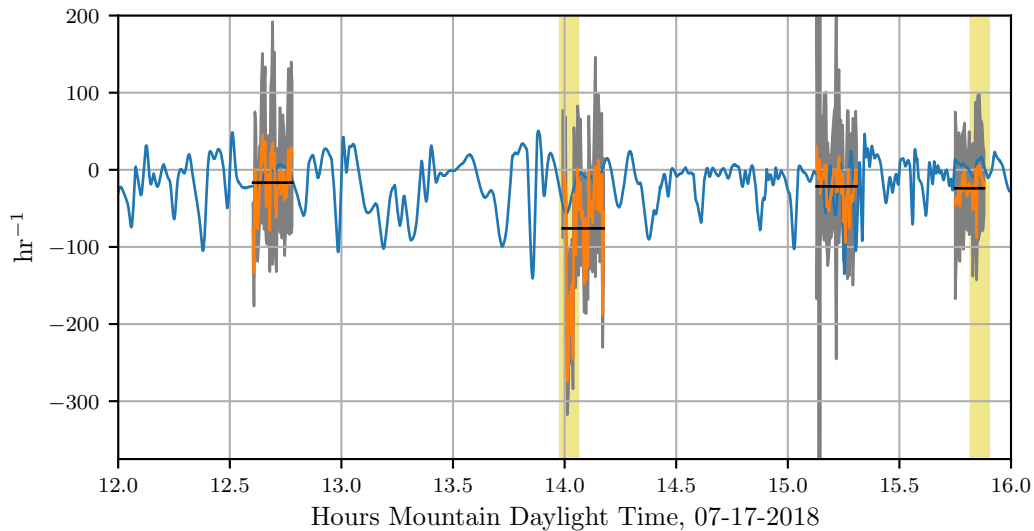


Figure 4.13: The attraction rate from WRF-LES predictions (blue) and the attraction rate as calculated from sensor measurements (orange) overlaid with flight average of the attraction rate (black). The uncertainty ranges for the attraction rate measurements are shown in gray. The attraction rate from the WRF-LES comes from the 10 m height level wind speed, while wind speed measurements used to calculate the attraction rate were performed by sensors at 15 m. Times of interest are highlighted with a yellow vertical line, corresponding to the predicted attraction rate fields shown in figures 4.14 and 4.15, respectively.

localized convective circulations that resulted in gusty higher winds at the grid point closest to the measurement site. However, within 5 km the 10 m winds were still below 4 m s<sup>-1</sup> as observed through 1545 MDT (Figures 4.9 and 4.10). Quantifying this spatial and temporal variability can be captured through ensemble approaches which can be derived using spatial statistics and/or by running a multi-member ensemble; however, such analyses are beyond the scope of this manuscript.

Analyzing the time series data, we see that the attraction rate has quick repeated dips in it, indicating short bursts of attracting activity. Comparing this to the the attraction rate fields shown in figure 4.14, we can see that the convective cells are bordered by narrow troughs of the attraction rate field. These dips appear to be an indicator of the movement of convective cells across a location, and thus a transition of the observer from one convective

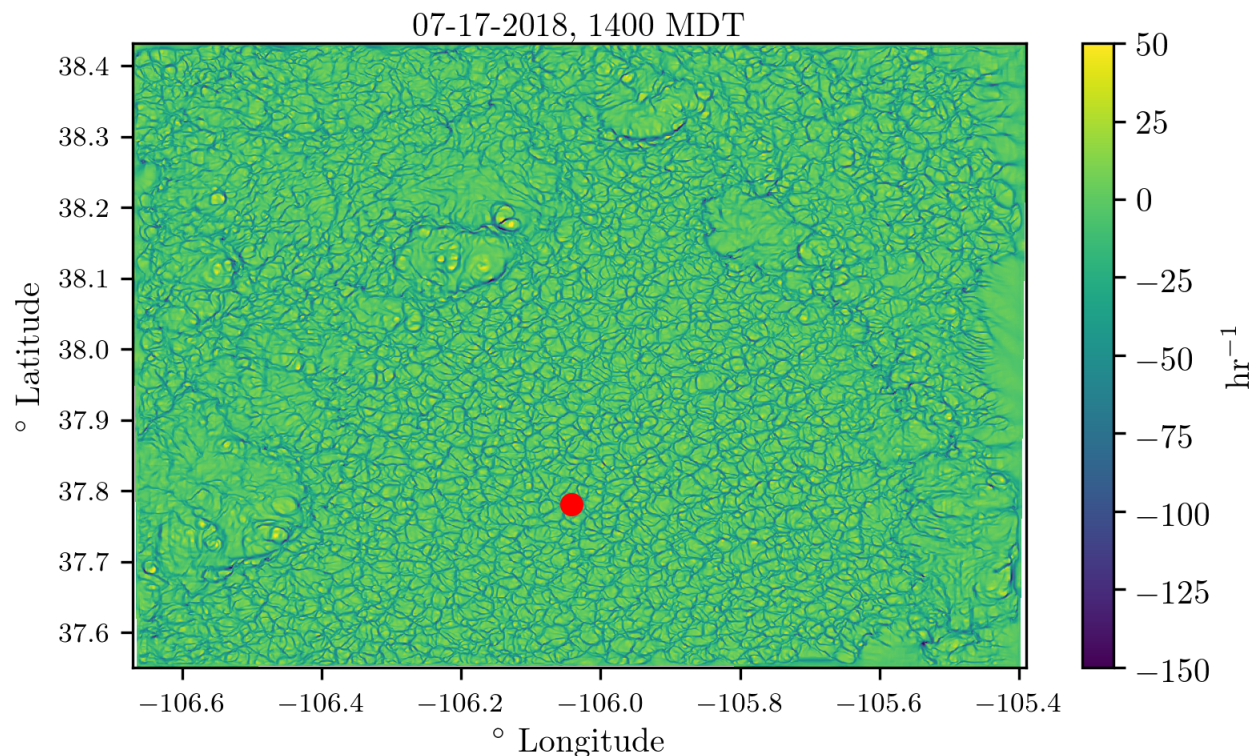


Figure 4.14: The attraction rate field at 1400 MDT, convective cells can be seen, bordered by troughs of the attracting field, throughout the domain. A front appears to be blowing an attracting feature out of the east of the domain. Sampling region is marked with a red dot.

cell to another.

As mentioned before, there was good agreement between the attraction rate as calculated from the WRF-LES model's predictions and the attraction rate as calculated from sensor measurements. There is an exception to this agreement during the second UAS mission on July 17, 2018 around 1400 MDT. During this mission, the sensors measured the attraction rate drop below  $-200\text{hr}^{-1}$ , yet the model prediction for this time was closer to  $-50\text{hr}^{-1}$ . Looking at the attraction rate field for this time period, figure 4.14, we can see there was a lot of convective activity going on in this region of the domain. Furthermore, looking at the time series data, figure 4.13, we can see that the WRF-LES model does predict a dip in the attraction rate around that time. These dips appear to be an indication of transition

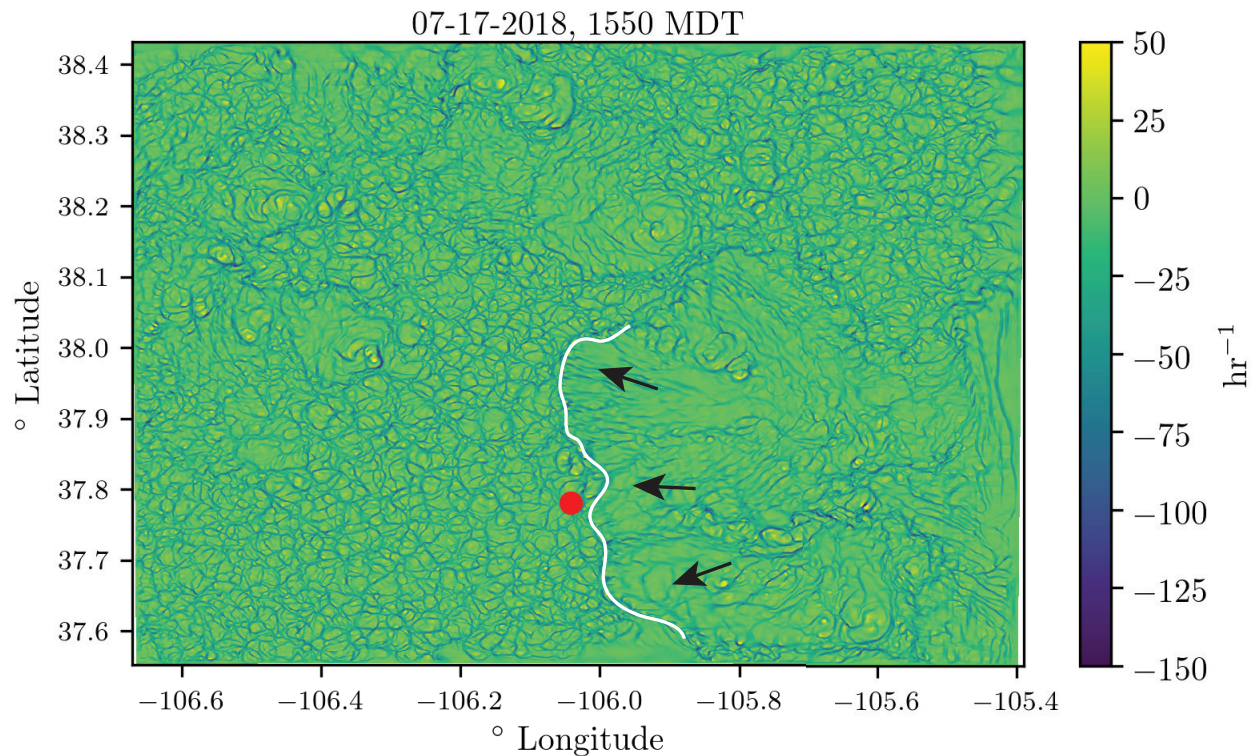


Figure 4.15: The attraction rate field at 1550 MDT, an attracting LCS can be seen along the center of the domain having ridden the front out of the east. The sampling region is marked with a red dot. Part of the attracting feature is shown as a white line. The direction the feature is moving is shown by black arrows.

between convective cells. Thus, the UAS and ground station measurements are likely picking up highly localized attraction at that time as a convective cell passes by, attraction which is falling below the scale of the model.

Another noteworthy event happened during the fourth UAS flight on 2018 July 17. During this flight, a front passes through the sampling area, coming out of the east. In figure 4.15, we show the predicted front (white curve) just before passing by our sampling area, marked as a red dot. In the time series data, figure 4.13, we can see two small dips right before 1600 in the attraction rate as predicted by the WRF-LES model. During this same period, we have a sharp drop in the attraction rate as calculated by our UAS measurements, followed by a quick uptick and then another drop as the flight data ends. These dips happen at

approximately the same time the front was predicted to pass through the sampling area. It is thus very likely that the drops calculated correspond to the predicted front passing through our measurement sampling area.

The troughs of the attraction rate field that we are detecting are very likely to be important indicators of LCSs. The attraction rate field is the limit of the backward-time FTLE field as integration time goes to zero [31]. As mentioned in the introduction, ridges of the FTLE field tend to coincide with LCSs [21, 22, 23, 24, 25, 26, 27, 28]. Whereas the FTLE is defined as a positively valued scalar field, indicating stretching, the attracting rate field is largely negative, indicating shrinking. Troughs of the attraction rate field are the analogues to ridges of the backward-time FTLE field. These troughs can be thought of as attracting LCSs. Therefore strong dips in the attraction rate time series should correspond to the passage of attracting LCSs.

## 5 Conclusions

We equipped a ground station and two UASs with identical ultrasonic anemometers. Flights reported here were conducted 10 to 15 meters AGL at the Leach Airfield in the San Luis Valley, Colorado as part of the ISARRA 2018 flight campaign. The ultrasonic anemometers were used to collect simultaneous measurements of wind speed and wind direction in a fixed triangle pattern. Results showed excellent agreement among sensors across different platforms, particularly for wind speed. Over the same time period as the sampling campaign, a WRF-LES model was used to determine the wind field across the sampling domain.

Data from the ground-based sensors and the two UASs were used to detect attracting regions (also known as Lagrangian coherent structures or LCSs), which have the potential to attract and transport high concentrations of chemical and biological agents. This is the first time

that direct measurement of an LCS indicator was made in the atmosphere using a team of sensors.

Coordinated teams of aerial and ground-based sensors provide unique environmental data that have the potential to inform real-time decisions regarding rapid emergency responses, such as following the transport of hazardous agents after a hurricane. The integration of real-time data from unmanned assets, advanced mathematical techniques for transport analysis, and predictive models can help assist in emergency response decisions in the future.

**Funding:** This research was supported in part by grants from the Institute for Critical Technology and Applied Science (ICTAS) at Virginia Tech, the National Science Foundation (NSF) under grant number AGS 1520825 (Hazards SEES: Advanced Lagrangian Methods for Prediction, Mitigation and Response to Environmental Flow Hazards) and DMS 1821145 (Data-Driven Computation of Lagrangian Transport Structure in Realistic Flows). Limited travel support for LAPSE-RATE participants was provided by the National Science Foundation (AGS 1807199) and the US Department of Energy (DE-SC0018985). Any opinions, findings, and conclusions or recommendations expressed in this material are those of the authors and do not necessarily reflect the views of the sponsors.

**Acknowledgments:** We thank J. Estridge, University of Kentucky, for serving as a pilot for some for some of the coordinated UAS missions. We also thank S. Borenstein and C. Dixon for their help with MURC operations.

**Conflicts of interest:** The authors declare no conflict of interest.

**Abbreviations:** The following abbreviations are used in this manuscript,

UAS	unmanned aircraft systems
AGL	Above ground level
FTLE	Finite-time Lyapunov exponent
LCS	Lagrangian coherent structure
OECS	Objective Eulerian coherent structure
WRF	Weather research and forecasting
LES	Large eddy simulation
MDT	Mountain daylight time
RMSE	Root-mean-square error

# Bibliography

- [1] Villa. An overview of small unmanned aerial vehicles for air quality measurements: Present applications and future prospectives. *Sensors*, 16(7):1 – 29, 2016. ISSN 14248220. doi: 10.3390/s16071072.
- [2] Benjamin L. Hemingway, Amy E. Frazier, Brian R. Elbing, and Jamey D. Jacob. Vertical sampling scales for atmospheric boundary layer measurements from small unmanned aircraft systems (suas). *Atmosphere*, 8(9):176, 2017. doi: 10.3390/atmos8090176. Copyright - Copyright MDPI AG 2017; Last updated - 2018-08-08.
- [3] Michał T. Chiliński, Krzysztof M. Markowicz, and Marek Kubicki. Uas as a support for atmospheric aerosols research: Case study. *Pure and Applied Geophysics*, 175(9): 3325–3342, 2018. ISSN 1420-9136. doi: 10.1007/s00024-018-1767-3.
- [4] Karen Anderson and Kevin J Gaston. Lightweight unmanned aerial vehicles will revolutionize spatial ecology. *Frontiers in Ecology and the Environment*, 11(3):138–146, 2013. doi: 10.1890/120150.
- [5] ML Hill, TG Konrad, JH Meyer, and JR Rowland. Small, radio-controlled aircraft as a platform for meteorological sensors. *Atmospheric Technology*, 6:114–122, 1974.
- [6] Jack Elston, Brian Argrow, Maciej Stachura, Doug Weibel, Dale Lawrence, and David Pope. Overview of small fixed-wing unmanned aircraft for meteorological sampling.

- Journal of Atmospheric and Oceanic Technology*, 32(1):97–115, 2015. doi: 10.1175/jtech-d-13-00236.1.
- [7] Pengzhi Tian and Haiyang Chao. Model aided estimation of angle of attack, sideslip angle, and 3d wind without flow angle measurements. In *2018 AIAA Guidance, Navigation, and Control Conference*, page 1844, 2018. doi: 10.2514/6.2018-1844.
- [8] Matthew B Rhudy, Trenton Larrabee, Haiyang Chao, Yu Gu, and Marcello Napolitano. Uav attitude, heading, and wind estimation using gps/ins and an air data system. In *AIAA Guidance, Navigation, and Control Conference*, page 5201, 2013. doi: 10.2514/6.2013-5201.
- [9] Andreas Wenz and Tor Arne Johansen. Estimation of wind velocities and aerodynamic coefficients for uavs using standard autopilot sensors and a moving horizon estimator. In *icuas*, pages 1267–1276, Miami, FL, USA, jun 2017. ieee. doi: 10.1016/j.measurement.2018.01.027.
- [10] Carl A Wolf, Richard P Hardis, Steven D Woodrum, Richard S Galan, Hunter S Wichelt, Michael C Metzger, Nicola Bezzo, Gregory C Lewin, and Stephan F J de Wekker. Wind data collection techniques on a multi-rotor platform. In *Systems and Information Engineering Design Symposium (SIEDS), 2017*, pages 32–37. IEEE, 2017. doi: 10.1109/sieds.2017.7937739.
- [11] Shimura Tomoya, Inoue Minoru, Tsujimoto Hirofumi, Sasaki Kansuke, and Iguchi Masato. Estimation of wind vector profile using a hexarotor unmanned aerial vehicle and its application to meteorological observation up to 1000m above surface. *Journal of Atmospheric and Oceanic Technology*, 35(8):1621 – 1631, 2018. ISSN 07390572. doi: 10.1175/jtech-d-17-0186.1.

- [12] Ian de Boisblanc, Nikita Dodbele, Lee Kussmann, Rahul Mukherji, Doug Chestnut, Stephanie Phelps, Gregory C Lewin, and Stephan F J de Wekker. Designing a hexacopter for the collection of atmospheric flow data. In *Systems and Information Engineering Design Symposium (SIEDS), 2014*, pages 147–152. IEEE, 2014. doi: 10.1109/sieds.2014.6829915.
- [13] Paolo Bruschi, Michele Dei, and Massimo Piotto. A low-power 2-d wind sensor based on integrated flow meters. *IEEE Sensors Journal*, 9(12):1688–1696, 2009. doi: 10.1109/jсен.2009.2030652.
- [14] P Bruschi, M Piotto, F DellAgnello, J Ware, and N Roy. Wind speed and direction detection by means of solid-state anemometers embedded on small quadcopters. *Procedia Engineering*, 168:802–805, 2016. doi: 10.1016/j.proeng.2016.11.274.
- [15] Patrick P Neumann and Bartholmai Matthias. Real-time wind estimation on a micro unmanned aerial vehicle using its inertial measurement unit. *Sensors and Actuators A: Physical*, 235:300–310, 2015. doi: 10.1016/j.sna.2015.09.036.
- [16] Ross T Palomaki, Nathan T Rose, Michael van den Bossche, Thomas J Sherman, and Stephan F J De Wekker. Wind estimation in the lower atmosphere using multirotor aircraft. *Journal of Atmospheric and Oceanic Technology*, 34(5):1183–1191, 2017. doi: 10.1175/jtech-d-16-0177.1.
- [17] Geoffrey W Donnell, Jordan A Feight, Nate Lannan, and Jamey D Jacob. Wind characterization using onboard imu of suas. In *2018 Atmospheric Flight Mechanics Conference*, page 2986, 2018.
- [18] Javier Moyano Cano. Quadrotor uav for wind profile characterization. Master’s thesis, Universidad Carlos III de Madrid, 2013.

- [19] Brandon M Witte, Robert F Singler, and Sean CC Bailey. Development of an unmanned aerial vehicle for the measurement of turbulence in the atmospheric boundary layer. *Atmosphere*, 8(10):195, 2017. doi: 10.3390/atmos8100195.
- [20] Javier González-Rocha, Craig Author Woolsey, Sultan Cornel, and Stephan F Joseph De Wekker. Sensing wind from quadrotor motion. *Journal of Guidance, Control, and Dynamics*, 2018. Preprint.
- [21] Shawn C Shadden, Francois Lekien, and Jerrold E Marsden. Definition and properties of lagrangian coherent structures from finite-time lyapunov exponents in two-dimensional aperiodic flows. *Physica D: Nonlinear Phenomena*, 212(3):271–304, 2005.
- [22] Benjamin Schindler, Ronald Peikert, Raphael Fuchs, and Holger Theisel. Ridge concepts for the visualization of lagrangian coherent structures. *Topological Methods in Data Analysis and Visualization II*, pages 221–235, 2012.
- [23] Carmine Senatore and Shane D Ross. Detection and characterization of transport barriers in complex flows via ridge extraction of the finite time lyapunov exponent field. *International Journal for Numerical Methods in Engineering*, 86(9):1163–1174, 2011.
- [24] P. Tallapragada, S. D. Ross, and D. G. Schmale. Lagrangian coherent structures are associated with fluctuations in airborne microbial populations. *Chaos*, 21:033122, 2011.
- [25] Phanindra Tallapragada and Shane D Ross. A set oriented definition of finite-time lyapunov exponents and coherent sets. *Communications in Nonlinear Science and Numerical Simulation*, 18(5):1106–1126, 2013.
- [26] Amir E BozorgMagham, Shane D Ross, and David G Schmale III. Real-time prediction of atmospheric lagrangian coherent structures based on forecast data: An application and error analysis. *Physica D: Nonlinear Phenomena*, 258:47–60, 2013.

- [27] A. E. BozorgMagham, S. D. Ross, and D. G. Schmale III. Local finite-time lyapunov exponent, local sampling and probabilistic source and destination regions. *Nonlinear Processes in Geophysics*, 22(6):663–677, 2015.
- [28] Amir E BozorgMagham and Shane D Ross. Atmospheric lagrangian coherent structures considering unresolved turbulence and forecast uncertainty. *Communications in Nonlinear Science and Numerical Simulation*, 22(1):964–979, 2015.
- [29] Gary K Nave Jr, Peter J Nolan, and Shane D Ross. Trajectory-free approximation of phase space structures using the trajectory divergence rate. *Nonlinear Dynamics*, 2019.
- [30] Mattia Serra and George Haller. Objective eulerian coherent structures. *Chaos: An Interdisciplinary Journal of Nonlinear Science*, 26(5):053110, 2016.
- [31] Peter J Nolan and Shane D Ross. Finite-time Lyapunov exponent field in the infinitesimal time limit. *viXra preprint viXra:1810.0023*, Dec 2018. URL <http://vixra.org/abs/1810.0023>.
- [32] W.C. Skamarock, J Klemp, Jimy Dudhia, D.O. Gill, Dale Barker, W Wang, and J.G. Powers. A description of the advanced research wrf version 3, near technical note tn-475+str. 27:3–27, 01 2008.
- [33] William C Skamarock and Joseph B Klemp. A time-split nonhydrostatic atmospheric model for weather research and forecasting applications. *Journal of Computational Physics*, 227(7):3465–3485, 2008.
- [34] Domingo Muñoz-Esparza, Robert Sharman, Jeremy Sauer, and Branko Kosović. Toward low-level turbulence forecasting at eddy-resolving scales. *Geophysical Research Letters*, 2018.

- [35] Bowen Zhou, Jason S Simon, and Fotini K Chow. The convective boundary layer in the terra incognita. *Journal of the Atmospheric Sciences*, 71(7):2545–2563, 2014.
- [36] K Lilly. On the application of the eddy viscosity concept in the inertial sub-range of turbulence. 1966.
- [37] Stanley G Benjamin, Stephen S Weygandt, John M Brown, Ming Hu, Curtis R Alexander, Tatiana G Smirnova, Joseph B Olson, Eric P James, David C Dowell, Georg A Grell, et al. A north american hourly assimilation and model forecast cycle: The rapid refresh. *Monthly Weather Review*, 144(4):1669–1694, 2016.
- [38] Thomas Peacock and George Haller. Lagrangian coherent structures: The hidden skeleton of fluid flows. *Physics today*, 66(2):41, 2013.
- [39] DG Schmale and SD Ross. Highways in the sky: Scales of atmospheric transport of plant pathogens. *Annual Review of Phytopathology*, 53:591–611, 2015.
- [40] David G. Schmale and Shane D. Ross. High-flying microbes: Aerial drones and chaos theory help researchers explore the many ways that microorganisms spread havoc around the world. *Scientific American*, February:32–37, 2017.

# Chapter 5

## Conclusion

### 1 Summary

The purpose of this dissertation is fill in some of the gaps in the theoretical, numerical, and experimental understanding of Eulerian diagnostics and their relationship to Lagrangian diagnostics, particularly with respect to the transport of material in geophysical flows. This is done by:

- proving rigorous mathematical connections between Lagrangian and Eulerian diagnostics for  $n$ -dimensional systems,
- formulating a new Eulerian diagnostic, the infinitesimal-time LCS (iLCS),
- exploring the ability of Eulerian diagnostics to detect Lagrangian dynamics,
- developing a new method to measure local Eulerian diagnostics using a single fixed-wing unmanned aircraft system (UAS),

- and applying Eulerian diagnostics to combined UAS and ground-based measurements to look for indications of LCSs.

In chapter 2 the deep mathematical relationships between Lagrangian and Eulerian diagnostics is rigorously proven. Higher order Eulerian approximations to the FTLE are derived using Taylor series expansions and Rivlin-Ericksen tensors. A new Eulerian diagnostic, iLCS, is derived by examining at the limit of LCS and the invariants Cauchy-Green tensor as integration time goes to zero. These methods are then tested on a number of example flows, including the double gyre, a realistic geophysical flow, and 3D analytic flows. These test cases demonstrated the mathematical relationship between between Eulerian and Lagrangian diagnostics by showing that the difference between the FTLE and Eulerian approximations goes to zero as integration time is decreased. These examples also illustrate the effectiveness of iLCS for predicting fluid parcel trajectories, in both analytic models and realistic flows. Notably, for the realistic flow iLCS were predictive for up to several hours.

In Chapter 3 the groundwork for being able to detect LCSs from a single fixed wing UAS is laid. A new algorithm is developed which approximates the gradient of a scalar field from measurements taken along a circular arc. After this, an OSSE was conducted which determined that it is, in principle, possible to use velocity measurements from a circling UAS to approximate the local Eulerian diagnostics at the center-point of the UAS orbit. A parametric study was then performed which determined that it is in fact possible to utilize Eulerian diagnostics infer Lagrangian dynamics. However, care needs to be taken with one's choice of Eulerian diagnostic, as well as with the choice of parameters values. Finally, these two concepts were combined into a single numerical experiment which found that it is possible to infer local Lagrangian dynamics from atmospheric velocity measurements gathered by a fixed-wing UAS.

In Chapter 4 the attraction rate is used to analyze wind velocity measurements. These mea-

measurements were taken by UASs and ground-based sensors during an atmospheric sampling campaign in the San Luis Valley, Co. over the summer of 2018. The attraction rate as calculated from these measurements is then compared to the attraction rate as computed from an WRF-LES model of the San Luis Valley. This comparison revealed that the sensors appeared to be picking up signals associated with atmospheric convective cells and an atmospheric front which passed out of the mountains. Convective cells have been found to be associated with LCS [1]; likewise as a flow separatrix, LCSs are likely to coincide with atmospheric fronts. Thus these attraction rate signals likely correspond to LCSs.

The work presented in this dissertation has a wide range of real world applications to fields as diverse as: tracking the spread of atmospheric contaminants, search and rescue operations, and optimizing the response to hazard releases. For example, one application could be to fly fixed wing UASs around hazardous areas, such as forest fires, and used the local attraction rate to determine where particulates, such as smoke, are more likely to converge. Likewise, networks of inexpensive UASs could be set up around urban areas and used to measure the local velocity gradients. From these gradients, iLCSs could then be computed. These iLCSs could then be used to track where air contaminants are likely to move in order to provide better quality warnings.

## 2 Future research direction

As is often the case in science, this dissertation has raised more questions than it has answered. The following are potential research directions that could stem from this dissertation.

From the work on Eulerian diagnostics in chapter 2, several research direction are possible. With a better understanding of how Eulerian diagnostics relate to Lagrangian diagnostics, a next step should be to apply Eulerian diagnostics to reduced order modeling in place

of Lagrangian diagnostics, as was done in [2]. This would likely speed up the generation of the new ROM, while still improving the accuracy of the ROM's subsequent Lagrangian characteristics. Another potential direction is to look for iLCS embedded within higher dimensional iLCS (e.g. a 1D iLCS embedded within a 2D iLCS). This would help to further the understanding of how fluid parcels evolve in the neighborhood of the LCS and could uncover new slow-fast systems. Additionally, the use of higher order FTLE approximations to detect Lagrangian transport structures in geophysical fluid flows would be a worthwhile direction. The geophysical flow example in chapter 2 demonstrated that iLCS can show how fluid parcels will evolve over several hours, higher order approximations may be valid for even long periods of time. This would be very useful in a hazardous release situation, where the accurate prediction of contaminant transport over longer periods of time would help to optimize the respond. Finally, finding a way to determine the interval over which Eulerian diagnostics are effective is a critical direction for this research. Users applying these methods in the field need to have a sense of the period of time for which these diagnostics are useful, in order to exploit them to their full extent.

The methodology laid out in chapter 3 has opened up several potential venues of exploration. First and foremost, the role of sensor uncertainty in the detection of LCS needs to be explored. As of now, this methodology has been tested using a "perfect" anemometer, however, in reality no instrument is perfect. Researchers looking for indications of LCS in the field need to know whether or not their instruments are sufficiently precise for the reliable detection of LCS. Second, this methodology should be applied to experimental data sets. As it stands this methodology has only been tested on numerical simulations, using this method to experimentally detect LCSs will give users added confidence in its strength. Another potential direction is to look for indications of iLCSs using UAS measurements. This should be fairly straight forward as UASs measure Eulerian data. Finally, this methodology

should be applied to search for LCSs associated with specific atmospheric species, such as those associated with water vapor [3]. While traditionally LCSs give an indication of how particles in a fluid flow will be transported, species specific LCSs will likely be more useful for situations such as hazardous response and air quality monitoring.

The Eulerian analysis of experimental data in chapter 4 opens the door more forms of dynamical systems analysis. In this chapter the attraction rate was used to analyze velocity field measurements. However, this dissertation has developed new higher order methods to analyze fluid flows. Thus, a next step should be to analyze experimental UAS and ground sensor data with higher order terms. Likewise, other tools, such as the trajectory divergence rate [4], could be applied to analyze these types of measurements. Future work could also seek to find indications of iLCS. This study already found likely indications of LCS. Since iLCS are the limit of LCS as integration time goes to zero, their indications were likely picked up as well. Additionally, with a few additional sensors the equations for iLCS could be directly evaluated. This would allow the direct experimental detection of iLCS, rather than just an inferred passing. Due to time constraints only a single run LES was used for the comparison with experimental measurements. While a single run LES simulation is sufficient, an ensemble simulation would better account the uncertainties associated with initial conditions and model parameterizations. Thus, future work should try to use ensemble forecasts to ensure more statistically robust comparisons. Finally, the experimental results should be compared to results from larger scale models such as NAM. This would filter out the noisy turbulence of the CBL and allow for the comparison of larger scale features passing through the area.

# Bibliography

- [1] Francois Lekien, Shawn C Shadden, and Jerrold E Marsden. Lagrangian coherent structures in n-dimensional systems. *Journal of Mathematical Physics*, 48(6):065404, 2007.
- [2] Xuping Xie, Peter J Nolan, Shane D Ross, and Traian Iliescu. Lagrangian data-driven reduced order modeling of finite time Lyapunov exponents, 2019. <https://arxiv.org/abs/1808.05635>.
- [3] Daniel Garaboa-Paz, Jorge Eiras-Barca, Florian Huhn, and Vicente Pérez-Muñuzuri. Lagrangian coherent structures along atmospheric rivers. *Chaos: An Interdisciplinary Journal of Nonlinear Science*, 25(6):063105, 2015.
- [4] Gary K Nave Jr, Peter J Nolan, and Shane D Ross. Trajectory-free approximation of phase space structures using the trajectory divergence rate. *Nonlinear Dynamics*, 2019.

